POLITECNICO
MILANO 1863

SCUOLA DI INGEGNERIA INDUSTRIALE
E DELL'INFORMAZIONE

Extension of Terminator Orbits for Solar Sail Applications around Small Bodies

Tesi di Laurea Magistrale in
Space Engineering - Ingegneria Spaziale

Author: **Maurizio Ondeggia**

Student ID: 243113
Advisor: Carmine Giordano
Co-advisors: Prof. Francesco Topputo, Alban Beshaj
Academic Year: 2024-2025

Abstract

This thesis presents an investigation into the design and control of novel orbits around asteroids employing solar sails. Based on previous studies, it is well known and well established that Sun Terminator Orbits (STOs) offer simple solutions and trajectories for solar sails; however, their flexibility in terms of observation and mission design is very limited. Resonant Terminator Orbits (RTOs) and Quasi Terminator Orbits (QTOs), previously studied for more conventional spacecrafts, exhibit enhanced surface coverage capabilities and offer a more versatile approach for orbit design, yet remain completely unexplored for solar sail propulsion.

The objective of this work is to adapt RTOs and QTOs for solar sail operations near minor bodies. The work will start with the development of methods to find RTOs and QTOs by using solar sails with two different type of controls, one with fixed-orientation and one with variable-orientation. Then, the effects of a non-ideal solar sail will be studied. Finally, there will be a brief discussion on how to design and evaluate the mission benefits and limitations offered by these orbit families.

The research presented in this thesis seeks to provide new orbital options for science-driven and fuel-free asteroid missions. The results obtained are valuable for applications in planetary defense, in-situ resource utilization and scientific exploration, particularly for small-body missions where propulsion mass is a strict constraint.

Keywords: Solar Sails, Asteroid Missions, Orbital Mechanics, Resonant Terminator Orbits, Quasi Termiantor Orbits, Orbit Design

Abstract in lingua italiana

Questa tesi presenta uno studio sulla progettazione e sul controllo di nuove orbite attorno agli asteroidi mediante vele solari. Sulla base di studi precedenti, è ben noto e consolidato che le Sun Terminator Orbits (STO) offrono soluzioni e traiettorie semplici per le vele solari; tuttavia, la loro flessibilità in termini di osservazione e progettazione della missione è molto limitata. Le Resonant Terminator Orbits (RTO) e le Quasi Terminator Orbits (QTO), già analizzate per veicoli spaziali più convenzionali, garantiscono una maggiore copertura della superficie e offrono un approccio più versatile alla progettazione orbitale, ma restano del tutto inesplorate per la propulsione a vela solare.

L'obiettivo di questo lavoro è adattare le QTO e le RTO alle operazioni con vele solari in prossimità di corpi minori. Il lavoro inizia con lo sviluppo di metodi per individuare RTO e QTO utilizzando vele solari con due diversi tipi di controllo: uno a orientamento fisso e uno a orientamento variabile. Successivamente saranno studiati gli effetti di una vela solare non ideale. Infine, si discuterà brevemente come progettare e valutare i vantaggi e le limitazioni di missione offerti da queste famiglie orbitali.

La ricerca presentata in questa tesi mira a fornire nuove opzioni orbitali per missioni scientifiche verso asteroidi senza l'uso di propellente. I risultati ottenuti sono di particolare interesse nel campo della difesa planetaria, dell'utilizzo in-situ delle risorse e dell'esplorazione scientifica, in particolare per missioni verso corpi minori in cui la massa destinata alla propulsione costituisce un vincolo critico.

Parole chiave: Vele Solari, Missioni verso Asteroidi, Meccanica Orbitale, Resonant Terminator Orbits, Quasi Terminator Orbits, Design Orbitale

Contents

1 | Introduction

This chapter introduces the research topic by first explaining the motivation for the study, it then reviews the current state of the art, defines the research question and objectives, and concludes with an outline of the thesis structure.

1.1. Motivation

In recent years, the number of known asteroids has grown dramatically, with more and more objects now cataloged, located not only in the main asteroid belt, but also in near-Earth space [1]. These small bodies, primordial remnants of the formation of the solar system, hold valuable clues about planetary origins and the distribution of volatiles and organic compounds, while also offering strategic potential for resource extraction. Apart from possible scientific and economic return, these objects can also represent a threat to our Earth and species, so awareness of the impact hazard has heightened scientific and technological interest. Missions dedicated to asteroid exploration and characterization, especially those aiming to visit multiple targets, require innovative propulsion solutions to understand the composition, dynamics, and possible deflection methods.

In this context, solar sails represents an innovative opportunity: by exploiting solar radiation pressure they can provide continuous thrust without propellant, enabling flexible trajectories and extended mission lifetimes to increase the scientific return [2]. In the last decades, numerous missions demonstrated the capabilities of these novel designs, such as JAXA's IKAROS [3], which was one of the first successful attempts, confirming via flight testing in deep space that large solar sail technology is a viable solution for space flight operations, and NanoSail-D, which performed a similar function for smaller spacecrafts. Despite these advancements, the first mission that should have exploited solar sails to visit one or several asteroids, that being NEA Scout, failed after contact was never established after launch [4] and after that no other mission has been attempted.

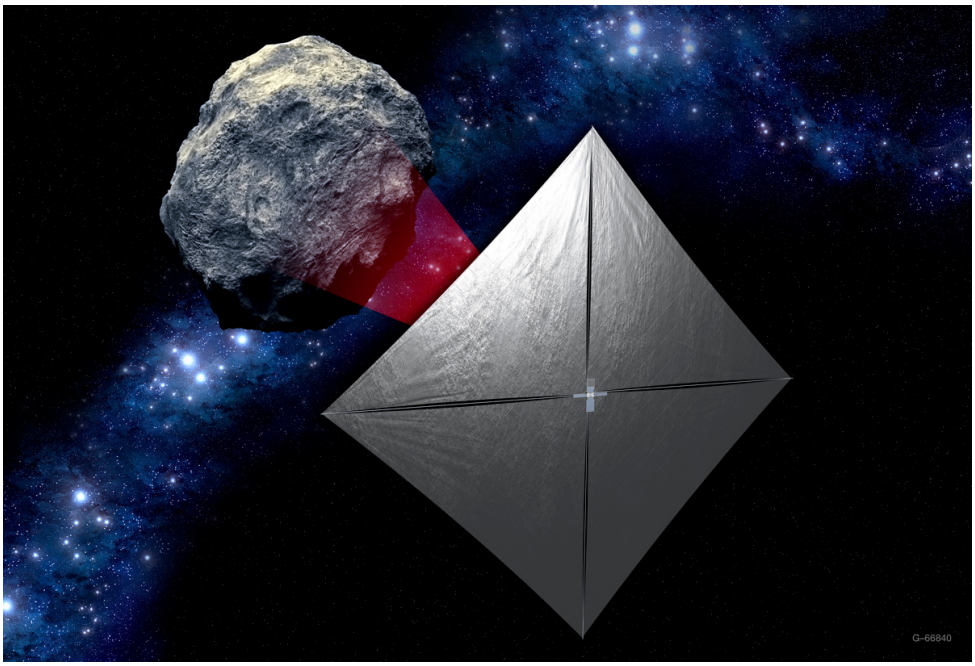

Figure 1.1: Artist's illustration of NASA's NEA Scout cubesat [5].

Different applications have been proposed over the years regarding different aspects of solar sails: attitude determination and control [6], design of interplanetary heliocentric trajectories [7, 8], with also multiple rendezvous [9], and asteroid insertion [8, 10]. However, this work will focus primarily on close-proximity operations and orbit options around asteroids assuming ideal attitude controls and with the sail already injected in the gravity field.

1.2. State of the art

The field of astrodynamics around small bodies experienced a considerable evolution over the past two decades. Scheeres [11, 12] provided one of the seminal overviews of orbital dynamics in the challenging gravitational environments near small bodies. The work focuses primarily on two aspects of the dynamic environment: the irregular shape and weak gravitational field of the asteroid, and the Solar Radiation Pressure (SRP) generated by the Sun. The most appropriate modeling approach depends on the area-to-mass ratio of the spacecraft. When this ratio is high—as in the case of solar sails—SRP dominates over the irregular gravitational effects, which can then be approximated using a simpler spherical model. In contrast, for satellites with a low area-to-mass ratio, the irregular gravity of the asteroid becomes the dominant effect and must be modeled with higher fidelity.

Morrow et al. [13] initiated the study of solar sail operations near asteroids, by modeling the dynamics of the problem with the Hill Three-Body Problem in a rotating frame. They defined the control and constraints of the solar sail with the sail pitch angle and the clock angle. With these foundations it was possible to identify Artificial Equilibrium Points (AEPs), where solar sail can hover above an asteroid in equilibrium, balancing the asteroid gravitational field and the SRP. While this work briefly touched on orbits located in the terminator plane (plane perpendicular to the Sun direction), it focused on larger asteroids like Vesta, Eros, and Ida, where gravity is order of magnitudes stronger than on smaller near-Earth objects (NEOs) such as Apophis or Bennu.

Heiligers and Scheeres [14] expanded the concepts of AEPs by studying families of solar-sail periodic orbits around these equilibrium points, while also presenting the option of pole-sitter-like orbits in binary asteroids systems. Farrés et al. [15–17] expanded the family of periodic orbits by also introducing Horizontal and Vertical Lyapunov orbits, as well as Halo orbits (or terminator orbits) located near the L2 point of the Augmented Hill 3-Body problem. Moreover, this study introduced a non-perfect model for the solar sail which takes into consideration both reflectivity and absorption. However, all these studies focus on asteroids of the size of Vesta and periodic orbits where both the sail pitch and clock angle are fixed, neglecting the possibility of using control to extend these orbits to smaller asteroids. In addition, these orbits present additional limitations related to the high range from the body and the high Sun-body-spacecraft (SBS) angles, which impact observation capabilities.

Williams and Abate [18] explored the concept of furlable solar sails, where the sail area becomes the main control variable for the spacecraft, focusing on hovering dynamics above asteroids both in the rotating sun–asteroid frame and in the fixed body frame. Moore [10] incorporated active control for the sail orientation, with the use of genetic algorithm and Linear Quadratic Regulator (LQR) methods when flying in the proximity of the asteroids, where the dynamics is modeled with a high-fidelity gravity field. This approach opened the door to new orbit types aligned with the ecliptic plane, which had not been demonstrated previously. Urrios [8] expanded the use of terminator orbits for solar sails to very small asteroids such as Apophis, where the SRP perturbation is far more relevant with respect to the dynamical environment of Vesta. This was done by actively employing the sail pitch and clock angles into the dynamic.

Several other studies focused on solar sails orbits in the three body problem involving the Sun–Earth or Moon–Earth systems, such as: Lyapunov and Halo orbits [19, 20], trajectories with applications to the lunar south pole [21], and periodic orbits above the ecliptic [22].

As of now, there have been no studies on the use of RTOs and QTOs for solar sails, despite their strict connection to STOs, so here is a brief introduction. Broschart et al. [23, 24] introduced, studied and classified RTOs and QTOs starting from the already assessed STOs. The authors presented new families of multi-revolution resonant orbits that originate from periodic bifurcation of STOs. These were shown to provide valuable observation geometries, as they remain on the Sun-facing side of the plane, enabling observations at low SBS angles — which yield a higher scientific return — while also not requiring frequent station-keeping thanks to their stability. Oki et al. [25] and Damme and Oberst [26] conducted numerical and analytical studies on the more general case of QTOs, showing a trade-off between their orbital elements, stability and geometric properties. Since then, the options for these orbits have been studied for possible mission scenarios to small bodies such as OSIRIS-APEX [27] or Hayabusa 2 [28].

1.3. Research question and objectives

The design of solar sails faces an inherent challenge: while high thrust is desirable for rapid heliocentric transfers, once near the asteroids the SRP must be kept low to avoid escaping their weak gravitational field. As previously noted, extensive research has explored various strategies for orbit design around small bodies. However, most approaches either rely on simple STOs with limited flexibility, place spacecraft in distant orbits near AEPs or Lagrangian points where long periods in shadow cause visibility challenges, or focus on massive asteroids, thereby overlooking the challenges posed by high SRP.

Therefore, the main research question addressed in this work is:

Is it possible to extend the concept of RTOs and QTOs to solar sails operating near small bodies, even under SRP dominated dynamical environments?

To comprehensively address this question, this research will pursue the following objectives: investigating different control strategies to mitigate the effects of SRP and provide multiple options, analyzing various levels of asteroid gravitational field strength to better categorize these orbits under different SRP conditions and developing methods to simplify the mission design process.

1.4. Thesis structure

The thesis is structured as follows:

- **Chapter 2** develops the physics and mathematical modeling background used for the thesis. First, the orbital mechanics model used, the Augmented Normalized Hill 3-Body problem (ANH3BP) and the static perturbed 2-Body problem in cylindrical coordinates, are presented. Then, the solar sail models are introduced, along with the two main control schemes considered: one with fixed-orientation and one with variable-orientation. Next, the main mathematical tools are introduced, including: the State Transition Matrix (STM), simple shooting method, differential correction schemes, numerical continuation, the monodromy matrix, and stability indices. Lastly, the main references for the asteroids and solar sail used in the simulations are presented.
- **Chapter 3** provides two different methods to find RTOs for solar sails. First, it introduces the keplerian averaging method to find keplerian orbits for a fixed-orientation solar sail. From there, artificial families of orbits similar to STOs are found and then RTOs can be derived with a combined use of simple shooting, differential correction, and numerical continuation. Then, it provides a similar method to find RTOs for a variable-orientation solar sail and finally, a comparison between stability indices of different families of orbits is reported.
- **Chapter 4** introduces parabolic coordinates and the Hamilton–Jacobi method to find closed form solutions for QTOs for a fixed-orientation sail. Then, a method for the variable-orientation control exploiting the equilibrium energy is derived and presented.
- **Chapter 5** provides a discussion on the effects that a non-ideal sail model might have on the previous results. In addition, provides some brief examples on how to design orbits for mapping applications.
- **Chapter 6** presents a summary of the work and the conclusions. It is followed by a brief discussion on the potential future studies that could enhance the work done in this Master's Thesis.

2 | Background

2.1. Orbital mechanics models

The primary orbital mechanics models adopted in this thesis are the ANH3BP and the perturbed two-body problem in cylindrical coordinates. Introducing a more elaborate framework such as the Circular Restricted 3-Body problem (CR3BP) with SRP as a perturbation would increase complexity without offering greater accuracy than the ANH3BP. The same reasoning applies to the asteroid gravity: when using solar sails, the SRP dominates the asteroid's gravity by several orders of magnitude, so detailed models such as the Spherical Harmonics Expansion (SHE) or the polyhedron model are neglected in this preliminary study.

2.1.1. Augmented Normalized Hill 3-Body problem

The ANH3BP models the motion of an infinitesimal particle (spacecraft) that interacts with a small mass (asteroid) and is perturbed by a distant massive body (Sun), and also takes into account the effect of SRP. This model assumes:

- the mass of the particle is much smaller than the rest;
- the mass of the main body (Sun) is much bigger than the asteroid;
- the second body orbits in a circular and planar motion around the first body;
- the third body is in the vicinity of the second body.

This model is formulated in the asteroid's Local-Vertical Local-Horizontal (LVLH) frame, centered on the asteroid itself, where the $\hat{x}$ axis represents the anti-Sun direction, the $\hat{z}$ axis is aligned with the angular momentum vector of the primaries, and the $\hat{y}$ axis completes the right-handed triad.

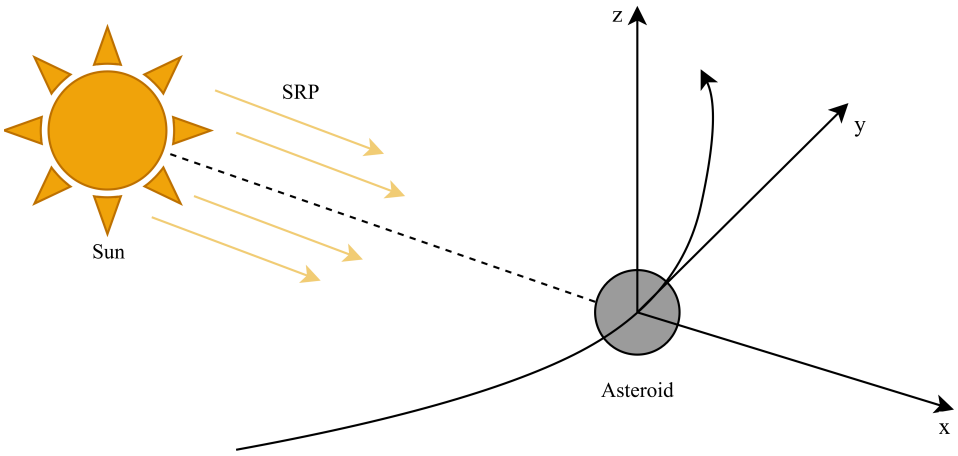

Figure 2.1: ANH3BP reference frame.

By defining $\mathbf{r} = [x, y, z]$ and $\mathbf{v} = [\dot{x}, \dot{y}, \dot{z}]$ as the position and velocity vectors of the spacecraft, respectively, and their coordinates with respect to the rotating frame centered on the primitive body, $r = \sqrt{x^2 + y^2 + z^2}$ and $v = \sqrt{\dot{x}^2 + \dot{y}^2 + \dot{z}^2}$ as their magnitudes, $\mathbf{a}_{srp} = [a_x, a_y, a_z]$ as the SRP acceleration in the same frame with $a_{srp} = \sqrt{a_x^2 + a_y^2 + a_z^2}$ being its magnitude, the Equations of Motion (EoM) can be written as [13]:

$$\begin{aligned} \ddot{x} &= -\frac{\mu_a}{r^3}x + 2N\dot{y} + 3N^2x + a_x \\ \ddot{y} &= -\frac{\mu_a}{r^3}y - 2N\dot{x} + a_y \\ \ddot{z} &= -\frac{\mu_a}{r^3}z - N^2z + a_z \end{aligned} \tag{2.1}$$

where μ_a is the gravitational constant of the asteroid and N is the orbital angular velocity of the asteroid. To further simplify the system, a Distance Unit (DU) and a Time Unit (TU) are defined as:

$$\begin{aligned} \text{DU} &= \left(\frac{\mu_a}{\mu_{sun}}\right)^{1/3} R \\ \text{TU} &= \frac{1}{N} \end{aligned} \tag{2.2}$$

where μ_{sun} is the gravitational constant of the Sun and R is the Sun-asteroid mean distance or semi-major axis. With this normalization $N = 1$ TU^{-1} and $\mu_a = 1$ DU^3 TU^{-2} and the EoM are simplified to:

$$\begin{aligned}\ddot{x} &= -\frac{x}{r^3} + 2\dot{y} + 3x + a_x \\ \ddot{y} &= -\frac{y}{r^3} - 2\dot{x} + a_y \\ \ddot{z} &= -\frac{z}{r^3} - z + a_z\end{aligned} \tag{2.3}$$

From these equations, an integral of motion, also known as the Jacobi constant, can be derived if the components of $\mathbf{a}_{srp}$ are constants [17]:

$$C = \frac{1}{2}v^2 - \frac{1}{r} - \frac{3}{2}x^2 + \frac{1}{2}z^2 - a_x x - a_y y - a_z z \tag{2.4}$$

2.1.2. Static perturbed 2-Body problem

Although less accurate than the ANH3BP, this kind of formulation for the 2-body problem will be especially useful in Chapter 4 when dealing with QTOs. The LVLH frame of the asteroid is still the reference frame for this dynamic.

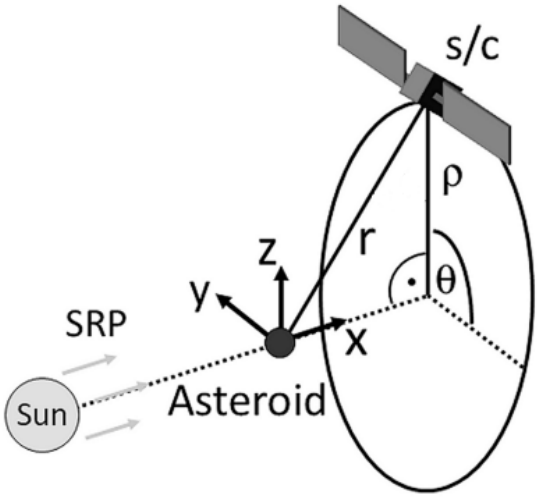

Figure 2.2: Static perturbed 2-Body problem reference frame [26].

Taking into account only SRP in the $\hat{x}$-axis, the gravity of the asteroid and neglecting the heliocentric motion, the Hamiltonian in cylindrical coordinates (x, ρ, θ) can be written as the sum of the kinetic energy K and the potential energy U [29]:

$$H = \underbrace{\frac{1}{2}\left(P_x^2 + P_\rho^2 + \frac{h_x^2}{\rho^2}\right)}_{K} \quad \underbrace{-\frac{\mu_a}{r} - a_{srp}x}_{U} \tag{2.5}$$

where $r = \sqrt{x^2 + \rho^2}$, momenta are defined as $P_x = \dot{x}$, $P_\rho = \dot{\rho}$, the angular momentum along the $\hat{x}$-axis is $h_x = \rho^2\dot{\theta}$, and the SRP acceleration a_{srp} is directed only along the $\hat{x}$-axis for now. The derivatives of the Hamiltonian $\partial H/\partial x = -\dot{P}_x$, $\partial H/\partial \rho = -\dot{P}_\rho$ give the EoMs:

$$\begin{aligned} \ddot{x} &= -\frac{\mu_a}{r^3}x + a_{srp} \\ \ddot{\rho} &= -\frac{\mu_a}{r^3}\rho + \frac{h_x^2}{\rho^3} \\ \ddot{\theta} &= -2\frac{\dot{\rho}}{\rho}\dot{\theta} \end{aligned} \tag{2.6}$$

It is technically possible to simplify these equations by introducing a set of normalized units.

2.2. Solar sail models and controls

2.2.1. Ideal solar sail model

Solar sail propulsion uses SRP to propel vehicles through space by reflecting solar photons from a large, mirror-like sail made of a lightweight, highly reflective material. An ideal solar sail is perfectly reflective, so no other optical characteristic will be considered, such as absorption or transmission. An important consequence of the ideal sail is that the SRP acceleration vector aligns with the normal vector to the solar sail. The first parameter to consider is the non-dimensional sail loading parameter, also called the sail lightness number, which is defined to be the ratio of the SRP acceleration at Earth to the solar gravitational acceleration:

$$\beta = \frac{2I}{m}\frac{R_0^2 S}{c}\frac{1}{\mu_{sun}} \tag{2.7}$$

where $I = 1368$ W/m^2 is the solar irradiance at 1 astronomical unit (AU), R_0 is the distance from the Sun to Earth, c is the speed of light, S is the surface area of the spacecraft in m^2, and m is the mass in kg. The only parameters that are not constants in this equation are the area and mass of the spacecraft. Typically, for solar sails, the area-to-mass ratio is very high, which is convenient for heliocentric trajectories, but can become a problem when dealing with strong SRP perturbations near small asteroids; in fact, a high sail lightness number results in strong SRP force. In order to obtain the SRP acceleration near the asteroid, the following formula is used:

$$a_{srp} = \frac{\mu_{sun}\beta}{R^2} \tag{2.8}$$

where R is the mean distance from the Sun to the sail in km. It is possible to normalize the sail acceleration to make it consistent with the ANH3BP formulation [16]:

$$k = K_1(S/m)\mu_a^{-1/3} \tag{2.9}$$

where $K_1 \approx 7.8502$ if S is given in m^2 and m in kg. From this equation, it can be seen that the value of the normalized sail acceleration depends only on the area-to-mass ratio of the solar sail and the gravitational parameter of the small body. Finally, the acceleration vector can be defined as:

$$\mathbf{a}_{srp} = k(\hat{\mathbf{r}}_s \cdot \hat{\mathbf{n}})^2\hat{\mathbf{n}} \tag{2.10a}$$

$$\mathbf{a}_{srp} = a_{srp}(\hat{\mathbf{r}}_s \cdot \hat{\mathbf{n}})^2\hat{\mathbf{n}} \tag{2.10b}$$

depending on whether the vector and its components are required in dimensional or nondimensional form, where $\hat{\mathbf{r}}_s = [1, 0, 0]$ is the direction of the incident light and will be always constant in this reference frame, while $\hat{\mathbf{n}}$ is the vector normal to the solar sail and its definition changes depending on the type of control. The direction of the SRP acceleration can never be pointed toward the Sun, constraining the attitude with $\hat{\mathbf{r}}_s \cdot \hat{\mathbf{n}} \geq 0$. Moreover, the versor of the SRP acceleration $\hat{\mathbf{a}}_{srp}$ for the ideal sail model is the same as the normal of the sail $\hat{\mathbf{n}} = \hat{\mathbf{a}}_{srp}$.

2.2.2. Fixed-orientation control

Most orbits presented in Section 1.2 rely on a fixed orientation to control the sailcraft, that means that the two control angles do not change over time. In this case, the normal vector to the solar sail will be defined as:

$$\hat{\mathbf{n}} = (\cos\alpha\cos\delta, \cos\alpha\sin\delta, \sin\alpha) \tag{2.11}$$

where α is the sail pitch angle with respect to the sun line and δ is the orientation angle about the $\hat{z}$-axis, also known as the clock angle. Because the sail normal is required to point in the anti-solar direction, the pitch angle is limited to be $-\pi/2 \leq \alpha \leq \pi/2$. Moreover, to satisfy the attitude constraint $\hat{\mathbf{r}}_\mathbf{s} \cdot \hat{\mathbf{n}} \geq 0$, the clock angle will be limited as well to be $-\pi/2 \leq \delta \leq \pi/2$. The orientation scheme can be seen in Figure 2.3.

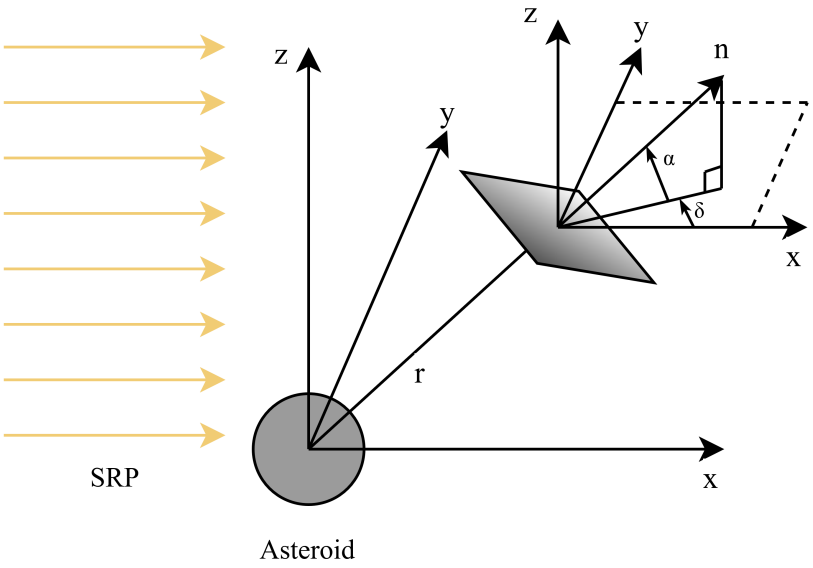

Figure 2.3: Fixed-orientation control angles.

Applying this normal vector to Equation 2.10a, the following terms are obtained:

$$\begin{aligned} a_x &= k\cos^3\alpha\cos^3\delta \\ a_y &= k\cos^3\alpha\cos^2\delta\sin\delta \\ a_z &= k\cos^2\alpha\cos^2\delta\sin\alpha \end{aligned} \tag{2.12}$$

The EoM for the ANH3BP then assume the following form:

$$\begin{aligned} \ddot{x} &= -\frac{x}{r^3} + 2\dot{y} + 3x + k\cos^3\alpha\cos^3\delta \\ \ddot{y} &= -\frac{y}{r^3} - 2\dot{x} + k\cos^3\alpha\cos^2\delta\sin\delta \\ \ddot{z} &= -\frac{z}{r^3} - z + k\cos^2\alpha\cos^2\delta\sin\alpha \end{aligned} \tag{2.13}$$

From Equation 2.13 it can be noted that the sail redirects the SRP acceleration, which in its absence would always point in the $\hat{x}$-axis, but the overall effect is reduced, since the norm of the acceleration would be $a_{srp} = k\cos^2\alpha\cos^2\delta$. This reduction becomes critical when operating near small asteroids, where the SRP can be strong enough to cause a sailcraft to escape if it has an extremely high sail lightness number.

2.2.3. Variable-orientation control

With a fixed-orientation control, it is possible to reduce the effects of the SRP; however, it becomes impossible to find orbits where the accelerations are directed towards the $\hat{x}$-axis, since the pitch and clock angle cannot be zero if a reduction on the accelerations is needed. To cover this case, a variable orientation control is implemented. Firstly, the normal vector to the sail is redefined as:

$$\hat{\mathbf{n}} = (\cos\alpha_v, \sin\alpha_v \sin\delta_v, \sin\alpha_v \cos\delta_v) \tag{2.14}$$

where the subscript $(\cdot)_v$ is there to differentiate these angles from the fixed-orientation ones, the sail pitch angle α_v is the angle that the normal vector forms with the $\hat{x}$-axis, while the clock angle δ_v is the angle between the projection of the normal vector in the y-z plane and the $\hat{z}$-axis, in the clockwise direction, as can be seen in Figure 2.4:

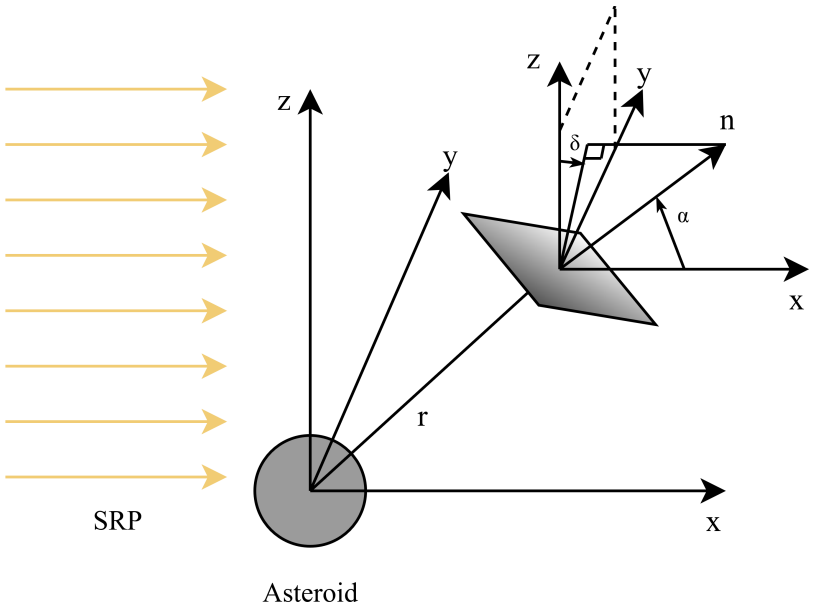

Figure 2.4: Variable-orientation control angles.

With this scheme, the norm of the acceleration is reduced by $\cos^2\alpha_v$, making the pitch angle the main control variable to reduce the SRP effect. Following the work done by Urrios [8], by defining the clock angle to have the same definition, but applied to the asteroid-spacecraft position vector instead of the normal vector of the sail, yields:

$$\sin\delta_v = \frac{y}{r_{yz}}, \quad \cos\delta_v = \frac{z}{r_{yz}} \tag{2.15}$$

where $r_{yz} = \sqrt{y^2 + z^2}$. By applying all these new definitions to Equation 2.10a, the components of the acceleration become:

$$\begin{aligned} a_x &= k\cos^3\alpha_v \\ a_y &= k\cos^2\alpha_v \sin\alpha_v \frac{y}{r_{yz}} \\ a_z &= k\cos^2\alpha_v \sin\alpha_v \frac{z}{r_{yz}} \end{aligned} \tag{2.16}$$

In this case, there is no constraint on the clock angle, but the pitch angle remains subject to the same limitation as in the fixed-orientation control. Moreover, when $0 \leq \alpha_v \leq \pi/2$ the resulting acceleration points away from the $\hat{x}$-axis, whereas for $-\pi/2 \leq \alpha_v \leq 0$ it points toward it. For the purposes of this study, α is restricted to the range $0 \leq \alpha_v \leq \pi/2$, as this choice provided the best results. The final EoM for the ANH3BP are:

$$\begin{aligned} \ddot{x} &= -\frac{x}{r^3} + 2\dot{y} + 3x + k\cos^3\alpha_v \\ \ddot{y} &= -\frac{y}{r^3} - 2\dot{x} + k\cos^2\alpha_v \sin\alpha_v \frac{y}{r_{yz}} \\ \ddot{z} &= -\frac{z}{r^3} - z + k\cos^2\alpha_v \sin\alpha_v \frac{z}{r_{yz}} \end{aligned} \tag{2.17}$$

Since the components of the acceleration are not constants anymore, these EoM do not have the same Jacobi constant as Equation 2.4, however, another integral of motion is still possible in the form of [8]:

$$C = \frac{1}{2}v^2 - \frac{1}{r} - \frac{3}{2}x^2 + \frac{1}{2}z^2 - k\cos^2\alpha_v(x\cos\alpha_v + r_{yz}\sin\alpha_v) \tag{2.18}$$

This kind of control is actually the same as that employed by McInnes [29], although the formulation was in cylindrical coordinates. In fact, the definition of δ_v given in Equations 2.15 is the same as the coordinate θ for the static perturbed 2-Body problem in cylindrical coordinates. This leads to an interesting formulation which will be particularly useful in Chapter 4, where the Hamiltonian becomes:

$$H = \frac{1}{2}\left(P_x^2 + P_\rho^2 + h_x^2/\rho^2\right) - \frac{\mu_a}{r} - x\ a_{srp}\cos^3\alpha_v - \rho\ a_{srp}\cos^2\alpha_v \sin\alpha_v \tag{2.19}$$

and the new EoM are:

$$\begin{aligned}
\ddot{x} &= -\frac{\mu_a}{r^3}x + a_{srp}\cos^3\alpha_v \\
\ddot{\rho} &= -\frac{\mu_a}{r^3}\rho + \frac{h_x^2}{\rho^3} + a_{srp}\cos^2\alpha_v \sin\alpha_v \\
\ddot{\theta} &= -2\frac{\dot{\rho}}{\rho}\dot{\theta}
\end{aligned} \tag{2.20}$$

2.2.4. Non-ideal solar sail model

Here, a more general model for the solar sail is presented, mainly to study the effects on the orbits which will be found throughout this study, which will be presented in Chapter 5. A simplified non-perfectly reflecting solar sail model from Dachwald et al. [30] will be used, where absorption is taken into account, but all photons are assumed to be reflected specularly, neglecting diffuse and back reflection. By defining the reflection coefficient as ξ_r, the absorbed part will be $(1-\xi_r)$, since no transmission is considered. Therefore, the new expression for the acceleration is:

$$\mathbf{a}_{srp} = k(\hat{\mathbf{r}}_s \cdot \hat{\mathbf{n}})[\xi_r(\hat{\mathbf{r}}_s \cdot \hat{\mathbf{n}})\hat{\mathbf{n}} + \frac{1}{2}(1-\xi_r)\hat{\mathbf{r}}_s] \tag{2.21}$$

It is important to note that if $\xi_r = 1$, Equation 2.10a is obtained again. The new acceleration components for the fixed-orientation and variable-orientation control are, respectively:

$$\begin{aligned}
a_x &= k(\xi_r \cos^3\alpha\cos^3\delta + \frac{1}{2}(1-\xi_r)\cos\alpha\cos\delta) \\
a_y &= k\ \xi_r \cos^3\alpha\cos^2\delta\sin\delta \\
a_z &= k\ \xi_r \cos^2\alpha\cos^2\delta\sin\alpha
\end{aligned} \tag{2.22}$$

$$\begin{aligned}
a_x &= k(\xi_r \cos^3\alpha_v + \frac{1}{2}(1-\xi_r)\cos\alpha_v) \\
a_y &= k\ \xi_r \cos^2\alpha_v \sin\alpha_v \frac{y}{r_{yz}} \\
a_z &= k\ \xi_r \cos^2\alpha_v \sin\alpha_v \frac{z}{r_{yz}}
\end{aligned} \tag{2.23}$$

Despite not being the most accurate model for solar sail dynamics, this yields the important change that the normal vector of the sail and the vector of the acceleration are no longer aligned.

2.3. Numerical tools

This section will focus on presenting the main numerical tools used in the thesis.

2.3.1. State Transition Matrix

The State Transition Matrix STM describes how small perturbations to the initial state evolve over time along a nominal trajectory. To derive it, the flow of a system must be first defined as the solution $\mathbf{x}$ of the system at a generic time instant t known its initial state $\mathbf{x}_0$ at the initial time t_0:

$$\mathbf{x}(t) = \varphi(\mathbf{x}_0, t_0; t) \tag{2.24}$$

If the system is affected by an initial small perturbation $\delta\mathbf{x}_0$, the flow becomes $\mathbf{x} + \delta\mathbf{x} = \varphi(\mathbf{x}_0 + \delta\mathbf{x}_0, t_0; t)$. If the initial perturbation is small enough, the propagation time is not too high and the dynamic is not highly nonlinear, a first order Taylor expansion of φ around $\delta\mathbf{x}_0$ can be performed while still maintaining a good precision:

$$\varphi(\mathbf{x}_0 + \delta\mathbf{x}_0, t_0; t) \approx \varphi(\mathbf{x}_0, t_0; t) + \frac{\partial\varphi}{\partial\mathbf{x}_0}(\mathbf{x}_0, t_0; t)\delta\mathbf{x}_0 \tag{2.25}$$

The STM is defined as:

$$\mathbf{\Phi}(\mathbf{x}_0, t_0; t) = \frac{\partial\varphi(\mathbf{x_0}, t_0; t)}{\partial\mathbf{x}_0} \tag{2.26}$$

and the perturbation at time instant t can be approximated as:

$$\delta\mathbf{x}(t) \approx \mathbf{\Phi}(\mathbf{x}_0, t_0; t)\delta\mathbf{x}_0 \tag{2.27}$$

This means that the STM represents the derivative of the final state with respect to its initial state after propagation, since:

$$\mathbf{\Phi}(\mathbf{x}_0, t_0; t_f) = \frac{\partial\varphi(\mathbf{x}_0, t_0; t_f)}{\partial\mathbf{x}_0} = \frac{\partial\mathbf{x}_f}{\partial\mathbf{x}_0} \tag{2.28}$$

One method to compute the STM is with a variational approach. Given a generic dynamical system $\dot{\mathbf{x}} = \mathbf{f}(t, \mathbf{x})$, a small perturbation in the state translates into a perturbation in the state derivative:

$$\delta\dot{\mathbf{x}}(t) = J(\mathbf{x})\delta\mathbf{x}(t) \tag{2.29}$$

where $J = \partial\mathbf{f}/\partial\mathbf{x}$ is the Jacobian matrix of the dynamics, evaluated at the nominal state, and for the ANH3BP has the following form:

$$J(\mathbf{x}) = \begin{bmatrix} 0 & 0 & 0 & 1 & 0 & 0 \\ 0 & 0 & 0 & 0 & 1 & 0 \\ 0 & 0 & 0 & 0 & 0 & 1 \\ U_{xx} & U_{xy} & U_{xz} & 0 & 2 & 0 \\ U_{yx} & U_{yy} & U_{yz} & -2 & 0 & 0 \\ U_{zx} & U_{zy} & U_{zz} & 0 & 0 & 0 \end{bmatrix} \tag{2.30}$$

where each subscripts represent a derivative with respect to the reported coordinate of the potential of the ANH3BP. These expressions are reported in Appendix A. By deriving Equation 2.27 with respect to time:

$$\delta\dot{\mathbf{x}}(t) = \dot{\mathbf{\Phi}}(t_0, t)\delta\mathbf{x}_0 \tag{2.31}$$

where, for simplicity of notation, the $\mathbf{x}_0$ dependence is omitted. Substituting this expression for $\delta\dot{\mathbf{x}}(t)$ and the expression for $\delta\mathbf{x}(t)$ in Equation 2.27 onto Equation 2.29, the following expression is obtained:

$$\dot{\mathbf{\Phi}} = J(\mathbf{x})\mathbf{\Phi} \tag{2.32}$$

where the initial condition is $\mathbf{\Phi}(t_0, t_0) = \mathbf{I}_6$ with $\mathbf{I}_6$ being the 6×6 identity matrix. The STM at a generic time instant t is then obtained by integrating this system of Ordinary Differential Equations (ODEs). Since the variational equations depend on the state of the system, Equation 2.32 must be integrated along with the system dynamics. For the ANH3BP this means that a total of $n + n^2 = 42$ ODEs must be integrated, where n is the number of states of the system, which in this case is 6.

2.3.2. Monodromy matrix and stability indices

In the case of periodic orbits of period T the value of the STM at time $t = T$ is called the Monodromy matrix and it is of particular importance, since it contains important information about the orbit linear stability. It is defined as:

$$\mathbf{M} = \mathbf{\Phi}(t_0, T) \tag{2.33}$$

In particular, the eigenvalues of the monodromy matrix can be divided as three pairs of reciprocal eigenvalues, with a pair always being equat to 1, which represents the orbit periodicity:

$$\left[\lambda_1, \frac{1}{\lambda_1}, \lambda_2, \frac{1}{\lambda_2}, 1, 1\right] \tag{2.34}$$

while λ_i may be complex. A periodic orbit is stable only if the magnitude of each eigenvalue of $\mathbf{M}$ is equal to one, or more generally, all eigenvalues must lie on the unit circle in the complex plane [23]. To evaluate this condition, a pair of indices is introduced as follows:

$$\begin{aligned} k_1 &= \lambda_1 + \frac{1}{\lambda_1} \\ k_2 &= \lambda_2 + \frac{1}{\lambda_2} \end{aligned} \tag{2.35}$$

where the stability condition is $|k_1| < 2$ and $|k_2| < 2$ except for degenerate situations where $\lambda_1 = \lambda_2$. The above formulas can be simplified with the following relations that do not require the computation of eigenvalues [28]:

$$\begin{aligned} a_1 &= 2 - \mathrm{tr}(\mathbf{M}) \\ a_2 &= \frac{1}{2}(a_1^2 + 2 - \mathrm{tr}(\mathbf{M}^2)) \\ k_{1,2} &= \frac{1}{2}\left(-a_1 \pm \sqrt{a_1^2 - 4a_2 + 8}\right) \end{aligned} \tag{2.36}$$

where $\mathrm{tr}(\cdot)$ is the trace operator on a matrix.

2.3.3. Simple shooting and differential correction scheme

To compute the periodic orbits considered in this study, a simple shooting predictor–corrector algorithm is used [23]. In this approach, the state vector is composed of all the state variables $\mathbf{x} = [x_0, 0, z_0, \dot{x}_0, \dot{y}_0, \dot{z}_0]$, except for y, which is set to 0:

$$\mathbf{Z} = [x_0, z_0, \dot{x}_0, \dot{y}_0, \dot{z}_0] \tag{2.37}$$

A vector of constraints describes the conditions for a periodic solution:

$$\mathbf{G}(\mathbf{Z}) = \left[(\mathbf{x}_0 - \mathbf{x}_f)_{2:6}\,,\ y_0,\ \dot{x}_0,\ \dot{z}_0,\ C(\mathbf{x}_f) - C_{\text{targ}}\right] \tag{2.38}$$

which requires the final propagated state to be the same as the initial one, except for the x component which caused convergence issues. The initial state satisfies $y_0 = \dot{x}_0 = \dot{z}_0 = 0$, and the final Jacobi constant to be equal to a prescribed one C_{targ}. The coordinate constraints imposed on the initial state force the solutions of the algorithm to be symmetric about the x–z plane. Although not strictly required, these constraints simplify the continuation process for the RTOs and help regularize the resulting solutions. The simple shooting was performed by using MATLAB's `fmincon` with the *interior-point* algorithm, while the objective function was set as:

$$F = \frac{1}{2}\|\mathbf{G}(\mathbf{Z})\|^2 \tag{2.39}$$

In addition to the simple shooting, a differential correction scheme is implemented, not only to numerically continue and regularize the solutions, but also to find STOs which will be used as a starting point for the search. The method presented here follows a similar workflow to that implemented by Koppel [31] for Halo orbits in the CR3BP. Equation 2.27 implies that by slightly altering the initial state of a trajectory, it can be corrected. In general:

$$\varphi(\mathbf{x}_0 + \delta\mathbf{x}_0, t_0; t_f) = \varphi(\mathbf{x}_0, t_0; t_f) + \mathbf{\Phi}(t_0, t_f)\delta\mathbf{x}_0 = \mathbf{x}_{targ} \tag{2.40}$$

where $\mathbf{x}_{targ}$ is the target final state, $\varphi(\mathbf{x}_0, t_f) = \mathbf{x}_f$ is the final state obtained with the propagation and $\delta\mathbf{x}_0$ is the correction that must be applied to the initial state to reach the target final state. A linear system to be solved for $\delta\mathbf{x}_0$ is then obtained:

$$\mathbf{\Phi}(t_0, t_f)\delta\mathbf{x}_0 = \mathbf{x}_{targ} - \mathbf{x}_f \tag{2.41}$$

This method can be further improved by expanding the flow in time $\varphi(\mathbf{x}_0 + \delta\mathbf{x}_0, t + \delta t)$ and also adding an expansion of the Jacobi constant $C(\mathbf{x} + \delta\mathbf{x})$. This yields:

$$\begin{bmatrix} \mathbf{\Phi} & \frac{d\varphi}{dt} \\ \frac{\partial C}{\partial \mathbf{x}_0} & 0 \end{bmatrix} \begin{pmatrix} \Delta\mathbf{x} \\ \Delta t_f \end{pmatrix} = \begin{pmatrix} \mathbf{x}_{targ} \\ C_{targ} \end{pmatrix} - \begin{pmatrix} \mathbf{x}_f \\ C \end{pmatrix} \tag{2.42}$$

where $d\varphi/dt$ is the right-hand side of the ANH3BP dynamics at the final time and the last component of the matrix is 0 since the Jacobi constant does not depend on time. With this method the correction is applied not only to the state, but also to the propagation time, increasing accuracy. Moreover, this scheme permits the selection of the Jacobi energy of an orbit. To further simplify the system, the same reasoning applied for the simple shooting can be made here and impose $y_0 = \dot{x}_0 = \dot{z}_0 = 0$. The final linear system is the following:

$$\begin{bmatrix} \Phi_{2,1} & \Phi_{2,3} & \Phi_{2,5} & \dot{y}_f \\ \Phi_{4,1} & \Phi_{4,3} & \Phi_{4,5} & \ddot{x}_f \\ \Phi_{6,1} & \Phi_{6,3} & \Phi_{6,5} & \ddot{z}_f \\ \frac{\partial C}{\partial x_0} & \frac{\partial C}{\partial z_0} & \frac{\partial C}{\partial \dot{y}_0} & 0 \end{bmatrix} \begin{pmatrix} \Delta x_0 \\ \Delta z_0 \\ \Delta \dot{y}_0 \\ \Delta t_f \end{pmatrix} = \begin{pmatrix} 0 - y_f \\ 0 - \dot{x}_f \\ 0 - \dot{z}_f \\ C_{targ} - C \end{pmatrix} \tag{2.43}$$

where the expressions for the derivatives of C are listed in the Appendix A. The process is repeated until a certain tolerance on the final state is met. By slightly varying the wanted Jacobi constant each time, it is possible to numerically continue this process by using the previous solution found as initial guess for the new problem with the new Jacobi constant, as long as C is increased or decreased at a small rate.

The correction scheme from Equation 2.43 works whenever there's a symmetry in the orbit about the x-z plane, however it can be slightly changed to work for symmetries in the x-y plane too. In this case, the initial conditions to be adjusted are x_0, y_0 and $\dot{z}_0$, while imposing $z_0 = \dot{x}_0 = \dot{y}_0 = 0$. A more general correction scheme, where the only constraint is that the coordinate y is fixed, will also be used when there are no symmetries to be exploited:

$$\mathbf{b}(\mathbf{y}) = [\mathbf{x}_0 - \mathbf{x}_f, C_0 - C_f] \tag{2.44}$$

$$\Delta\mathbf{y} = -J(\mathbf{y})/\mathbf{b}(\mathbf{y}) \tag{2.45}$$

$$\mathbf{y}_{new} = \mathbf{y} + \Delta\mathbf{y} \tag{2.46}$$

where $\mathbf{y} = [x, z, \dot{x}, \dot{y}, \dot{z}, t_f]$, $J(\mathbf{y})$ is the Jacobian of $\mathbf{b}(\mathbf{y})$ obtained with a finite differences method and in the vector $\mathbf{x}_0$ the variable y is fixed.

2.4. Asteroids and solar sail references

This work focuses on solar sails mounted on CubeSats such as LightSail-1, LightSail-2 and NEA Scout, which serves as the primary reference for the sail parameters listed in

the following table:

Parameter	Value	Unit
Area	86	m^2
Mass	14	kg
Area-to-mass ratio	6.143	m^2/kg
Sail lightness number	0.009447	-
Acceleration at 1 AU	0.0560	mm/s^2

Table 2.1: NEA Scout parameters [32].

For the asteroid selection, three small bodies with markedly different masses—Eros, Apollo, and Apophis—were chosen to evaluate how each gravitational field affects solar sail dynamics. The key parameters required from each asteroid are the gravitational parameter (since the normalized sail acceleration in Equation 2.9 depends on it), the radius (important to evaluate the quality of the mapping), and the heliocentric distance (which sets the time unit). In principle, the eccentricity of their heliocentric orbits should also be considered to minimize variations in solar distance, but this factor is neglected here for simplicity.

Asteroid	μ_a [km^3/s^2]	r_a [km]	R [AU]	DU [km]	TU [days]	a_{srp} [mm/s^2]	k [-]
Eros	4.463×10^{-4}	8.42	1.45	3249.91	102	0.0267	631
Apollo	3.404×10^{-7}	0.75	1.47	301.07	104	0.0259	6907
Apophis	1.8×10^{-9}	0.163	0.92	32.82	51	0.0662	39642

Table 2.2: Selected asteroid parameters [33], the sail accelerations refer to NEA Scout.

As shown in Table 2.2, the normalized sail acceleration k is particularly high, especially for Apophis and Apollo. In comparison, typical mapping applications that employ RTOs and QTOs usually operate with k values in the range of 10 to 200 [34].

3 | Resonant Terminator Orbits

3.1. Keplerian averaging

RTOs are special orbits that arise from the periodic bifurcation of STOs. Before addressing RTOs in the context of solar sails, it is therefore useful to examine Keplerian orbits analogous to STOs. This analysis treats the sail's SRP acceleration as a perturbation and averages it over the Keplerian elements using the Lagrange Planetary Equations (LPEs) [35, 36]. The reference frame is the same as the one used for the ANH3BP, with the position of the spacecraft described by the keplerian elements as:

$$\mathbf{r} = \frac{a(1-e^2)}{1+e\cos\nu} \begin{bmatrix} \cos\Omega\cos(\omega+\nu) - \sin(\omega+\nu)\sin\Omega\cos i \\ \sin\Omega\cos(\omega+\nu) + \sin(\omega+\nu)\cos\Omega\cos i \\ \sin(\omega+\nu)\sin i \end{bmatrix} \tag{3.1}$$

where a is the semi-major axis, e the eccentricity, i the inclination, Ω the right ascension of the ascending node, ω the argument of periapsis, and ν the true anomaly of the spacecraft. The SRP produces an acceleration component along all axes:

$$\mathbf{a}_{srp} = a_{srp} \begin{bmatrix} \cos^3\alpha\cos^3\delta \\ \cos^3\alpha\cos^2\delta\sin\delta \\ \cos^2\alpha\cos^2\delta\sin\alpha \end{bmatrix} = \begin{bmatrix} a_x \\ a_y \\ a_z \end{bmatrix} \tag{3.2}$$

Finally, this acceleration can be expressed in terms of a potential force acting on the spacecraft as:

$$U_{SRP} = \mathbf{a}_{srp} \cdot \mathbf{r} \tag{3.3}$$

It is important to note that the shadowing effects during eclipses are not taken into account. The expanded expression for the potential is:

$$U_{SRP} = \frac{a(1-e^2)}{1+e\cos\nu}\big[a_x(\cos\Omega\cos\omega\cos\nu - \cos\Omega\sin\omega\sin\nu - \cos i\sin\Omega\sin\omega\cos\nu - \cos i\sin\Omega\cos\omega\sin\nu) + a_y(\sin\Omega\cos\omega\cos\nu - \sin\Omega\sin\omega\sin\nu + \cos i\cos\Omega\sin\omega\cos\nu + \cos i\cos\Omega\cos\omega\sin\nu) + a_z(\sin i\sin\omega\cos\nu + \sin i\cos\omega\sin\nu)\big] \tag{3.4}$$

The perturbation potential is then averaged over one orbital period by integrating with respect to the true anomaly as follows:

$$\bar{U}_{SRP} = \frac{(1-e^2)^{\frac{3}{2}}}{2\pi}\int_0^{2\pi}\frac{U_{SRP}(\nu)}{(1+e\cos\nu)^2}\,\mathrm{d}\nu \tag{3.5}$$

Every term in Equation 3.4 is either multiplied by $\sin\nu$ or $\cos\nu$, so this integral can be divided into two parts, where the main integrals to compute are:

$$\int_0^{2\pi}\frac{\sin\nu}{(1+e\cos\nu)^3}\,\mathrm{d}\nu = 0 \qquad \int_0^{2\pi}\frac{\cos\nu}{(1+e\cos\nu)^3}\,\mathrm{d}\nu = \frac{-3e\pi}{(1-e^2)^{\frac{5}{2}}} \tag{3.6}$$

The final expression for the averaged SRP potential is:

$$\bar{U}_{\mathrm{SRP}} = -\frac{3}{2}ae\big[\,a_x\left(\cos\Omega\cos\omega - \cos i\sin\Omega\sin\omega\right) + a_y\left(\sin\Omega\cos\omega + \cos i\cos\Omega\sin\omega\right) + a_z\sin i\sin\omega\big] \tag{3.7}$$

The Keplerian orbital motion of a spacecraft subject to perturbations is described by the following averaged LPEs:

$$\frac{da}{dt} = \frac{2}{na}\frac{\partial\bar{U}_{\mathrm{SRP}}}{\partial\sigma} \tag{3.8}$$

$$\frac{de}{dt} = \frac{1-e^2}{na^2e}\frac{\partial\bar{U}_{\mathrm{SRP}}}{\partial\sigma} - \frac{\sqrt{1-e^2}}{na^2e}\frac{\partial\bar{U}_{\mathrm{SRP}}}{\partial\omega} \tag{3.9}$$

$$\frac{di}{dt} = \frac{\cot i}{na^2\sqrt{1-e^2}}\frac{\partial\bar{U}_{\mathrm{SRP}}}{\partial\omega} - \frac{\csc i}{na^2\sqrt{1-e^2}}\frac{\partial\bar{U}_{\mathrm{SRP}}}{\partial\Omega} \tag{3.10}$$

$$\frac{d\Omega}{dt} = \frac{\csc i}{na^2\sqrt{1-e^2}}\frac{\partial\bar{U}_{\mathrm{SRP}}}{\partial i} - N \tag{3.11}$$

$$\frac{d\omega}{dt} = \frac{\sqrt{1-e^2}}{na^2e}\frac{\partial \bar{U}_{\text{SRP}}}{\partial e} - \frac{\cot i}{na^2\sqrt{1-e^2}}\frac{\partial \bar{U}_{\text{SRP}}}{\partial i} \tag{3.12}$$

where $n = \sqrt{\mu_a/a^3}$ is the mean motion of the spacecraft, $\sigma = -Nt_0$ is the mean anomaly, with t_0 being the time of periapsis passage. The longitude of the ascending node is defined with respect to the sun-asteroid line, and because of the reference frame of the work it is subject to a variation corresponding to the mean motion of the asteroid N. The final expressions for the LPEs are:

$$\frac{da}{dt} = 0 \tag{3.13}$$

$$\begin{aligned}\frac{de}{dt} = -\frac{3\sqrt{1-e^2}}{2na}\big[&a_x(\cos\Omega\sin\omega + \cos i\sin\Omega\cos\omega) + \\ &a_y(\sin\Omega\sin\omega - \cos i\cos\Omega\cos\omega) - \\ &a_z\sin i\cos\omega\big]\end{aligned} \tag{3.14}$$

$$\frac{di}{dt} = -\frac{3e}{2na\sqrt{1-e^2}}\big[a_x\sin\Omega\cos\omega\sin i - a_y\cos\Omega\cos\omega\sin i + a_z\cos i\cos\omega\big] \tag{3.15}$$

$$\frac{d\Omega}{dt} = -\frac{3e}{2na\sqrt{1-e^2}}\big[a_x\sin\Omega\sin\omega - a_y\cos\Omega\sin\omega + a_z\cot i\sin\omega\big] - N \tag{3.16}$$

$$\begin{aligned}\frac{d\omega}{dt} = -\frac{3}{2nea\sqrt{1-e^2}}\big[&a_z[(1-e^2)\cos\Omega\cos\omega - \cos i\sin\Omega\sin\omega] + \\ &a_y[(1-e^2)\sin\Omega\cos\omega + \cos i\cos\Omega\sin\omega] + \\ &a_z\big(\sin i\sin\omega - e^2\frac{\sin\omega}{\sin i}\big)\big]\end{aligned} \tag{3.17}$$

In order to obtain a frozen orbit such as STOs, the following condition must be satisfied:

$$\frac{da}{dt} = \frac{de}{dt} = \frac{di}{dt} = \frac{d\Omega}{dt} = \frac{d\omega}{dt} = 0 \tag{3.18}$$

This can be achieved with various strategies, three of them will be now presented.

3.1.1. Frozen keplerian orbits with $\delta = 0$

A simple method to satisfy Equation 3.18 is imposing:

$$\cos\Omega = 0 \wedge \cos\omega = 0 \tag{3.19}$$

which leads to:

$$\frac{de}{dt} = -\frac{3\sqrt{1-e^2}}{2na} a_y \sin\Omega \sin\omega \tag{3.20}$$

$$\frac{di}{dt} = 0 \tag{3.21}$$

$$\frac{d\Omega}{dt} = -\frac{3e}{2na\sqrt{1-e^2}} \big(a_x \sin\Omega \sin\omega + a_z \cot i \sin\omega\big) - N \tag{3.22}$$

$$\frac{d\omega}{dt} = \frac{3}{2nea\sqrt{1-e^2}} \Big[a_x \cos i \sin\Omega \sin\omega - a_z \Big(\sin i \sin\omega - e^2 \frac{\sin\omega}{\sin i}\Big)\Big] \tag{3.23}$$

where $\sin\Omega$ and $\sin\omega$ are either 1 or -1. The only way to nullify the derivative of the eccentricity is to impose $a_y = 0$. This can be done by choosing $\delta = 0$ in the fixed-orientation control. Finally, in order to force the derivatives of Ω and ω to vanish, they can be expressed as a function i and e:

$$\mathcal{G}_1(e,i) = \frac{d\Omega}{dt} = -\frac{3ea_{srp}\cos^2\alpha}{2na\sqrt{1-e^2}} \sin\omega^* \big(\cos\alpha \sin\Omega^* + \sin\alpha \cot i\big) - N \tag{3.24}$$

$$\mathcal{G}_2(e,i) = \frac{d\omega}{dt} = \frac{3a_{srp}\cos^2\alpha}{2nea\sqrt{1-e^2}} \sin\omega^* \Big[\cos\alpha \cos i \sin\Omega^* - \sin\alpha \Big(\sin i - \frac{e^2}{\sin i}\Big)\Big] \tag{3.25}$$

where the superscripts $(\cdot)^*$ signify that the value for Ω and ω are fixed, and in this case is either $\pi/2$ or $-\pi/2$. Frozen orbits are obtained by solving $\mathcal{G}_1(e,i) = \mathcal{G}_2(e,i) = 0$. The only remaining condition is to decide the semi-major axis in order to avoid escape. A good boundary condition can be adapted from Scheeres [11]:

$$a_{max} = \frac{1}{4}\sqrt{\frac{\mu_a m}{P_\Phi S \cos^2\alpha \cos^2\delta}} R \tag{3.26}$$

where m and S are the mass and area of the sail, $P_\Phi \approx 1 \times 10^8$ kg $\cdot$ km^3/(m^{2}s^2) is the Sun's radiation flux and R the mean distance of the asteroid from the Sun. In this case α and δ can be adjusted to increase the maximum possible semi-major axis. Here is an example at Eros where Equations 3.24 were solved graphically with contour plots, while the initial conditions are transformed in cartesian coordinates, adimensionalized and then propagated with the ANH3BP dynamics:

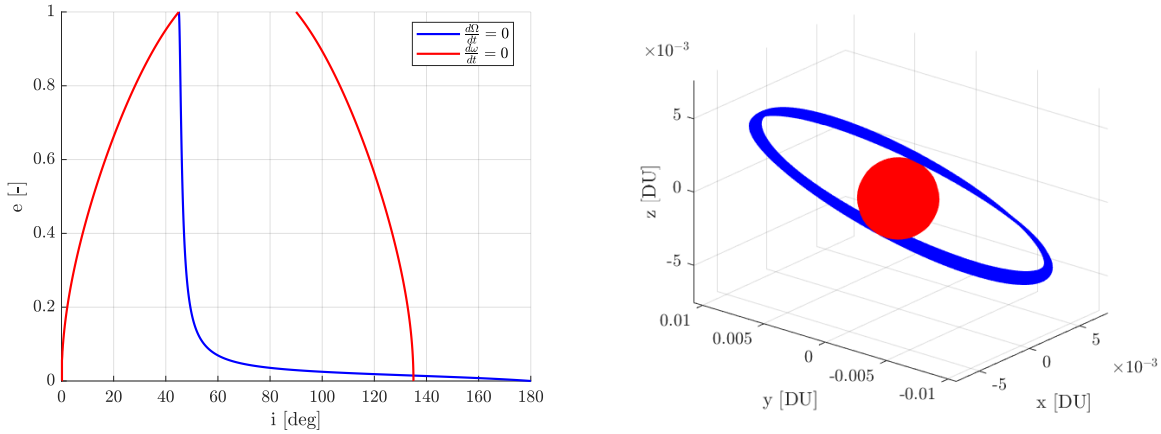

Figure 3.1: Frozen orbit at Eros with $a = 4r_a$, $e = 0.013$, $i = 135°$, $\Omega = -90°$, $\omega = 90°$, $\alpha = 45°$ and $\delta = 0°$.

3.1.2. Frozen keplerian orbits with $\alpha = 0$

A similar method can be achieved by imposing instead:

$$\cos i = 0 \wedge \cos \omega = 0 \tag{3.27}$$

which leads to:

$$\frac{de}{dt} = -\frac{3\sqrt{1-e^2}}{2na}\left(a_x \cos\Omega \sin\omega + a_y \sin\Omega \sin\omega\right) \tag{3.28}$$

$$\frac{di}{dt} = 0 \tag{3.29}$$

$$\frac{d\Omega}{dt} = -\frac{3e}{2na\sqrt{1-e^2}}\left(a_x \sin\Omega \sin\omega - a_y \cos\Omega \sin\omega\right) - N \tag{3.30}$$

$$\frac{d\omega}{dt} = -\frac{3}{2nea\sqrt{1-e^2}} a_z \left(\sin i \sin\omega - e^2 \frac{\sin\omega}{\sin i}\right) \tag{3.31}$$

where $\sin i$ and $\sin\omega$ are either 1 or -1. The only way to nullify the derivative of the argument of pericenter is to impose $a_z = 0$. This can be done by choosing $\alpha = 0$ in the fixed-orientation control. Similarly to the previous method, in order to force the derivatives of e and Ω to vanish, they can be expressed as a function e and Ω:

$$\mathcal{G}_3(e,\Omega) = \frac{de}{dt} = -\frac{3\sqrt{1-e^2}a_{srp}\cos^2\delta}{2na} \sin\omega^* \left(\cos\delta\cos\Omega + \sin\delta\sin\Omega\right) \tag{3.32}$$

$$\mathcal{G}_4(e,\Omega) = \frac{d\Omega}{dt} = -\frac{3ea_{srp}\cos^2\delta}{2na\sqrt{1-e^2}} \sin\omega^* \left(\cos\delta\sin\Omega - \sin\delta\cos\Omega\right) - N \tag{3.33}$$

The same procedure is then applied to obtain frozen orbits, with the exception that δ is the control parameter for the maximum semi-major axis. Here is an example at Eros:

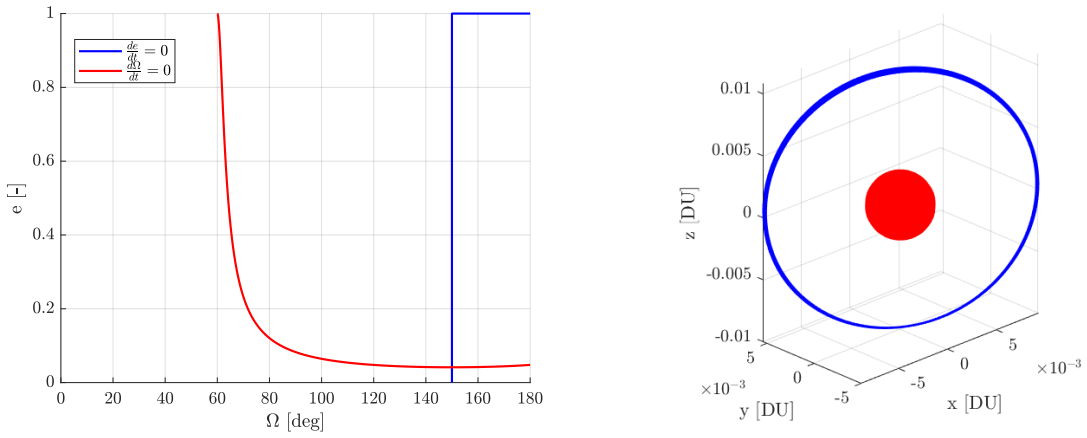

Figure 3.2: Frozen orbit at Eros with $a = 4r_a$, $e = 0.048$, $i = 90°$, $\Omega = 150°$, $\omega = -90°$, $\alpha = 0°$ and $\delta = 60°$.

3.1.3. Keplerian orbits with $\frac{d\Omega}{dt} = -N$

A more general solution for frozen orbits can be found by relaxing the condition of Equation 3.18 as follows:

$$\frac{da}{dt} = \frac{de}{dt} = \frac{di}{dt} = \frac{d\omega}{dt} = 0 \quad \wedge \quad \frac{d\Omega}{dt} = -N \tag{3.34}$$

This means that the rate of change of the argument of the ascending node will be related to the asteroid angular velocity about the Sun. To simplify the system now, the only condition needed is $\sin\omega = 0$ (meaning that either $\omega = 0$ or $\omega = \pi$), which brings:

$$\frac{de}{dt} = -\frac{3\sqrt{1-e^2}}{2na}\cos\omega^*\left[a_x\cos i\sin\Omega - a_y\cos i\cos\Omega - a_z\sin i\right] \tag{3.35}$$

$$\frac{di}{dt} = -\frac{3e}{2na\sqrt{1-e^2}}\cos\omega^*\left[a_x\sin\Omega\sin i - a_y\cos\Omega\sin i + a_z\cos i\right] \tag{3.36}$$

$$\frac{d\omega}{dt} = -\frac{3(1-e^2)}{2nea\sqrt{1-e^2}}\cos\omega^*\left[a_x\cos\Omega + a_y\sin\Omega\right] \tag{3.37}$$

$$\frac{d\Omega}{dt} = -N \tag{3.38}$$

By expanding the terms for the acceleration components, three equations can be obtained, but first, the one concerning the argument of periapsis will be analyzed (only the terms in parentheses since these are the ones which can be put to zero):

$$\cos\alpha\cos\delta\cos\Omega + \cos\alpha\sin\delta\sin\Omega = 0 \tag{3.39}$$
$$\cos\alpha\cos\delta\cos\Omega = -\cos\alpha\sin\delta\sin\Omega \tag{3.40}$$
$$\cot\Omega = -\tan\delta \tag{3.41}$$
$$\Omega = \delta - \frac{\pi}{2} \tag{3.42}$$

By substituting this expression for Ω in the equations for the rate of change of e and i, these equations are obtained:

$$\cos\alpha\cos\delta\cos i\sin\Omega - \cos\alpha\sin\delta\cos i\cos\Omega - \sin i\sin\alpha = 0 \tag{3.43a}$$
$$\cos\alpha\cos\delta\sin\Omega\sin i - \cos\alpha\sin\delta\cos\Omega\sin i + \sin\alpha\sin i = 0 \tag{3.43b}$$

$$-\cos\alpha\cos^2\delta\cos i - \cos\alpha\sin^2\delta\cos i - \sin i\sin\alpha = 0 \tag{3.44a}$$
$$-\cos\alpha\cos^2\delta\sin i - \cos\alpha\sin^2\delta\sin i + \sin\alpha\cos i = 0 \tag{3.44b}$$

$$\tan i = -\cot\alpha \tag{3.45a}$$
$$\tan i = \tan\alpha \tag{3.45b}$$

Equations 3.45 cannot be respected at the same time. However, by imposing $e = 0$, the rate of change of the inclination can be nullified from the start, so that the only remaining condition would be $\tan i = -\cot\alpha$, which brings:

$$i = \alpha - \frac{\pi}{2} \tag{3.46}$$

With Equations 3.42 and 3.46, all orbital elements are imposed by the control angles of the sail, which still influence the maximum semi-major axis. Here is an example at Eros with the sail normal vector visualized:

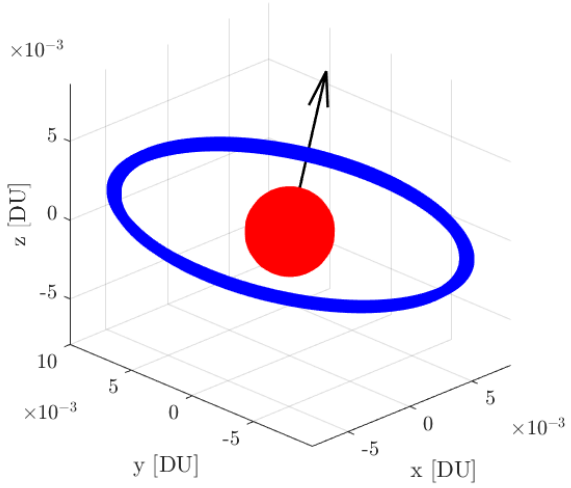

Figure 3.3: Frozen orbit at Eros with $a = 4r_a$, $e = 0$, $i = -50°$, $\Omega = -60°$, $\omega = 0°$, $\alpha = 40°$ and $\delta = 30°$.

3.1.4. Results

These orbits will be called Artificial Terminator Orbits (ATOs) as they do not lie on the terminator plane, but share similar properties to STOs, which can be visualized by numerically continuation. Only for these orbits, a pseudo-arclength continuation algorithm was used to obtain both stable and unstable orbits, which will be represented respectively as blue and red. The algorithm used is presented in Appendix B. In Figures 3.4 and 3.5 some examples with different orientation are reported:

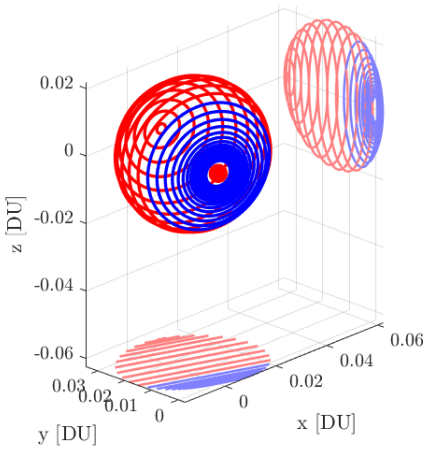

Figure 3.4: ATOs family at Apollo with $\alpha = 0°$ and $\delta = 70°$.

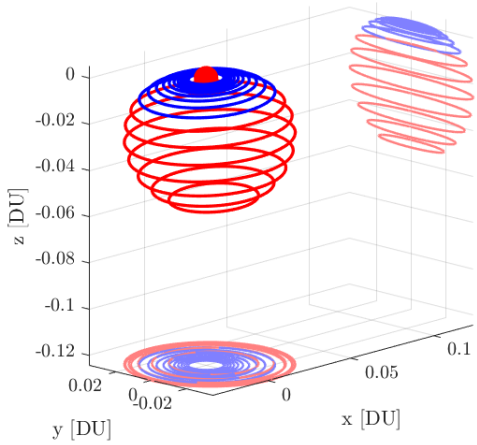

Figure 3.5: ATOs family at Apophis with $\alpha = -85°$ and $\delta = 0°$.

In this case only orbits with a certain symmetry about one plane were plotted, since the differential correction scheme and the continuation process are more straightforward. However, it is reasonable to think that these families also exist when $\alpha \neq 0 \ \wedge \ \delta \neq 0$ and there are no plane symmetries. A linear stability analysis was also conducted and compared with a normal family of STOs at Eros:

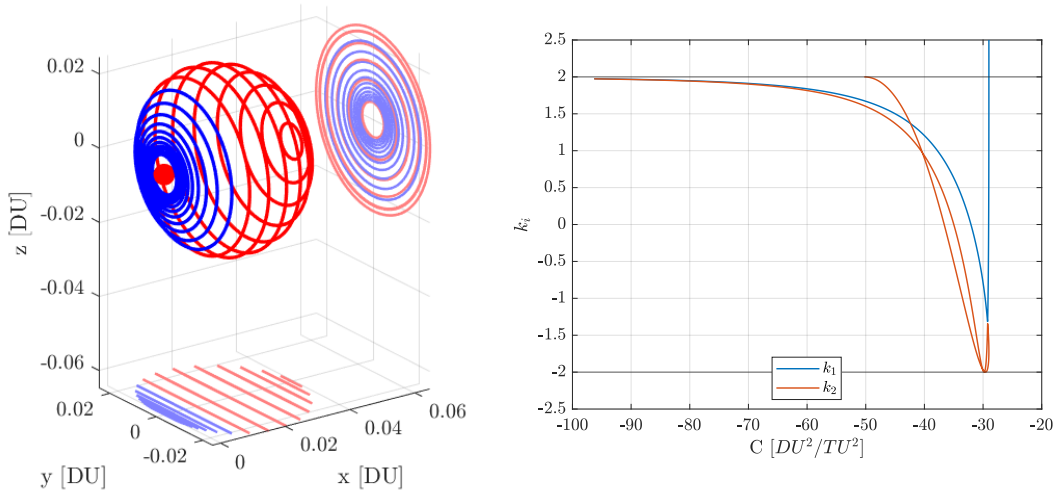

Figure 3.6: STOs family at Eros with respective stability indices.

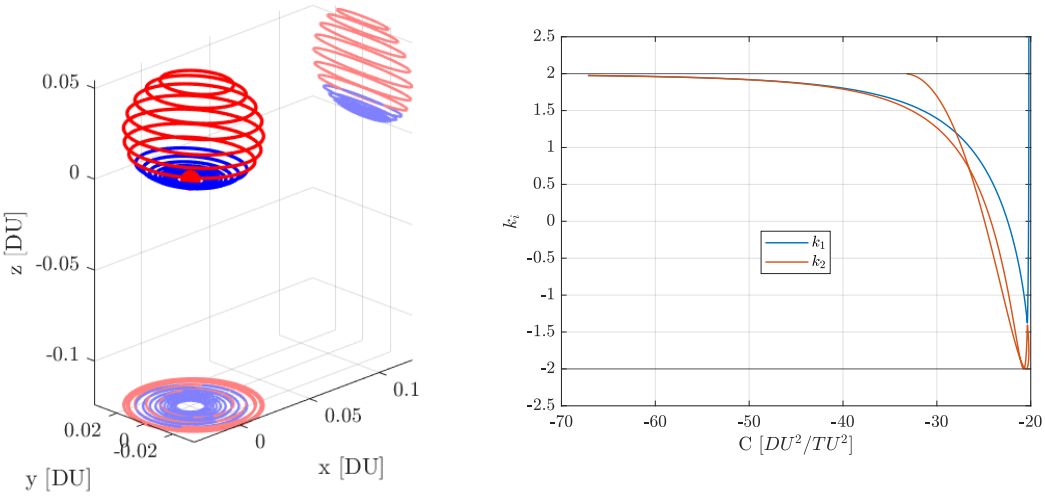

Figure 3.7: ATOs family at Apophis with $\alpha = 85°$ and $\delta = 0°$ and respective stability indices.

As shown, the stability indices are very similar between the two families, meaning that possibly also artificial RTOs might be possible.

3.2. Fixed-orientation RTOs

The process of identifying RTOs is relatively straightforward. Starting from a family of STOs near the asteroid, the continuation method is applied while monitoring the eigenvalues of the monodromy matrix. In this context, a stable complex eigenvalue can be written as $e^{i\theta_p}$, where θ_p is the phase angle, i.e., the angle formed with the positive real axis in the complex plane. The monodromy matrix of a periodic orbit evaluated over $m_r T$ is denoted by $\mathbf{M}^{m_r}$. RTOs originate from $m_r : n_r$ period-multiplying bifurcations. The corresponding stable eigenvalues take the form $e^{im_r\theta_p}$, with θ_p the phase angle accumulated over one orbital period. When the resonance condition $\theta_p = \frac{2n_r\pi}{m_r}$, for integers m_r and n_r, is satisfied, the system admits two real eigenvectors with unit eigenvalues. A perturbation along one of these eigenvectors then reproduces itself after m_r revolutions, leading-to a periodic orbit [23]. In this work, attention is restricted to RTOs of the type $m_r : 1$.

To develop an algorithm for identifying artificial RTOs in the most general form, without relying on symmetries, a simplification of the dynamics is introduced as a first step. Rather than considering all three components of the acceleration, only the x-component is retained, while preserving the full magnitude of the acceleration. The dynamics then becomes:

$$\begin{aligned} \ddot{x} &= -\frac{x}{r^3} + 2\dot{y} + 3x + \tilde{k} \\ \ddot{y} &= -\frac{y}{r^3} - 2\dot{x} \\ \ddot{z} &= -\frac{z}{r^3} - z \end{aligned} \tag{3.47}$$

where $\tilde{k} = k\cos^2\alpha\cos^2\delta$. This formulation essentially corresponds to the dynamics of a conventional spacecraft near an asteroid under the effect of SRP, with the acceleration modified to reproduce the component that a solar sail would experience along its normal direction. The initial conditions for the first STO are:

$$\mathbf{r}_0 = \begin{bmatrix} 0 \\ \gamma \cdot r_a \\ 0 \end{bmatrix}, \qquad \mathbf{v}_0 = \begin{bmatrix} 0 \\ 0 \\ \frac{1}{\sqrt{\gamma \cdot r_a}} \end{bmatrix} \tag{3.48}$$

where r_a is the asteroid radius and γ is an arbitrary real value between 1.5 and 5, which is adjusted depending on the magnitude of the SRP acceleration. The integration time

is set to $t_f = 2\pi\sqrt{(\gamma \cdot r_a)^3}$. These initial conditions serve as a very good initial guess for the differential correction scheme since these are the ones for circular orbits, which are very similar to STOs. After finding the first orbit, it is numerically continued until the phase angle $\theta_p = \frac{2\pi}{m_r}$ is reached. Here is an example for Apophis with $\alpha = 81°$, $\delta = 45°$ and $\tilde{k} = 485$:

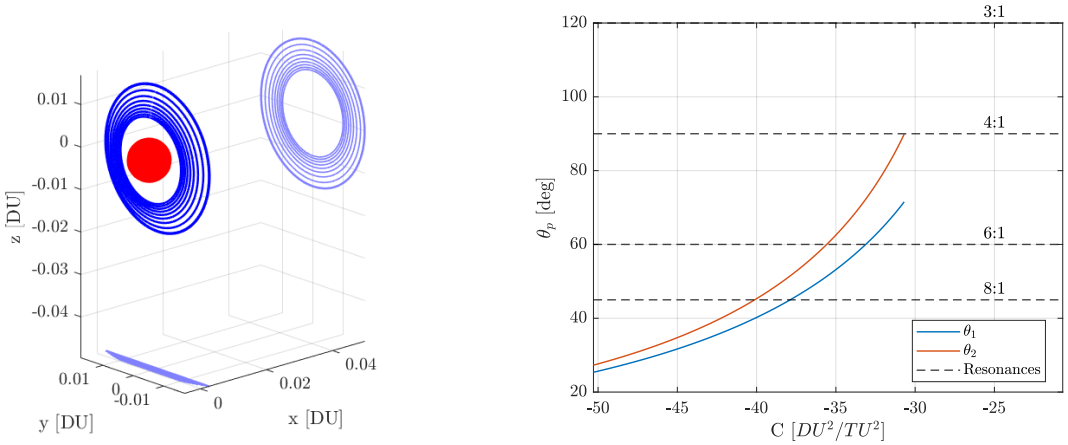

Figure 3.8: Family of STOs continued until 4:1 resonance is reached.

After reaching the desired $m_r : 1$ resonance, the final orbit obtained is then propagated for $t_f = m_r T$, in order to extract the eigenvector to perturb the initial condition. In this case, all rows and columns of the monodromy matrix are extracted except for the second one, corresponding to the variable y, which is the one always put to 0 in the simple shooting process. From this submatrix, the 5 by 1 eigenvector is extracted and it is added as a perturbation to the initial state of the last orbit:

$$\mathbf{x}_{0,RTO} = \mathbf{x}_0 + \gamma \cdot \begin{bmatrix} V_1 \\ 0 \\ V_{2:5} \end{bmatrix} \tag{3.49}$$

where V_i are the components of the eigenvector related to the unit eigenvalue of the $\mathbf{M}^{m_r}$ matrix, while γ is an arbitrary real value between 0.05 and 0.5 typically, and it has to be adjusted in a trial and error process. This initial condition is the one used in the single shooting method presented in Section 2.3.3, along with $t_f = m_r T$ and a Jacobi constant which is increased of the same value c from the last computed orbit. After the simple shooting, a numerical continuation takes place with the differential correction scheme and can be stopped until a certain value of the Jacobi constant is reached.

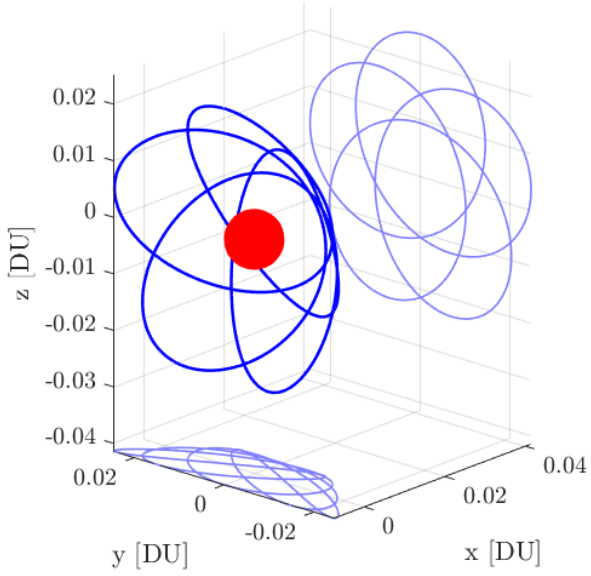

Figure 3.9: 4:1 RTO with $\tilde{k} = 485$.

However, this orbit must be rotated back in the LVLH frame with all components of the acceleration. This is done by rotating the initial condition with the following rotation matrices:

$$\mathbf{R}_\alpha = \begin{bmatrix} \cos\alpha & 0 & \sin\alpha \\ 0 & 1 & 0 \\ -\sin\alpha & 0 & \cos\alpha \end{bmatrix}, \quad \mathbf{R}_\delta = \begin{bmatrix} \cos\delta & \sin\delta & 0 \\ -\sin\delta & \cos\delta & 0 \\ 0 & 0 & 1 \end{bmatrix}, \quad \mathbf{r}_{0,rot} = \mathbf{R}_\delta^T \cdot \mathbf{R}_\alpha^T \cdot \mathbf{r}_0 \tag{3.50}$$

where the superscript $(\cdot)^T$ denotes the transpose of a matrix. The same can be done for the velocity $\mathbf{v}_0$. Since in the dynamics there are components indicating the perturbation of the Sun in the system and these are dependent on the reference frame, just rotating the initial condition is not enough for the orbit to close, so another differential correction must be applied. This can be done either by finding a state in the propagated orbit which has $y = 0$ and then applying the same correction scheme as before, or with a more general correction scheme. In Figure 3.10 the previous example at Apophis is shown before and after applying the correction scheme to the rotated initial conditions:

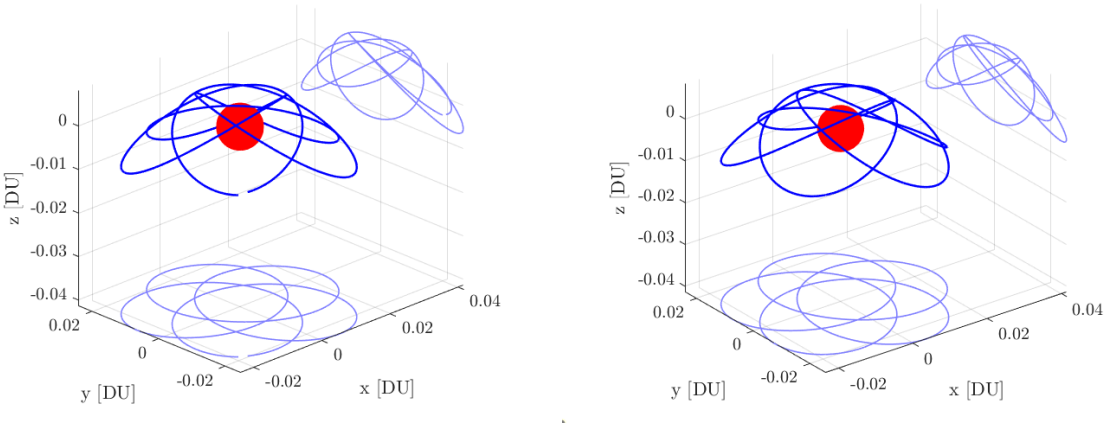

Figure 3.10: 4:1 RTO at Apophis with $\alpha = 81°$, $\delta = 45°$.

It is important to specify that if there is a plane symmetry such as with $\alpha = 0°$ or $\delta = 0°$, most of this process can be avoided and RTOs can be obtained directly from families such as the one represented in Figures 3.4 and 3.5 with the appropriate differential correction scheme. Here are more examples:

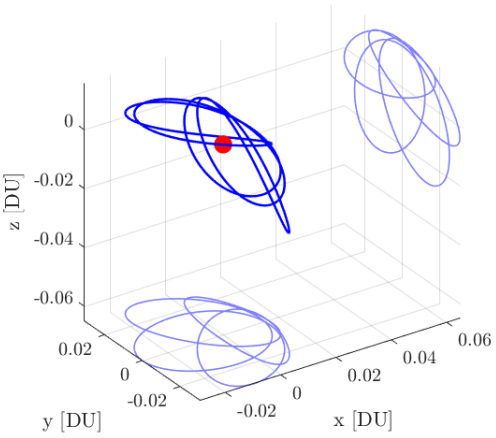

Figure 3.11: 4:1 artificial RTO at Eros with $\alpha = 45°$, $\delta = 0°$.

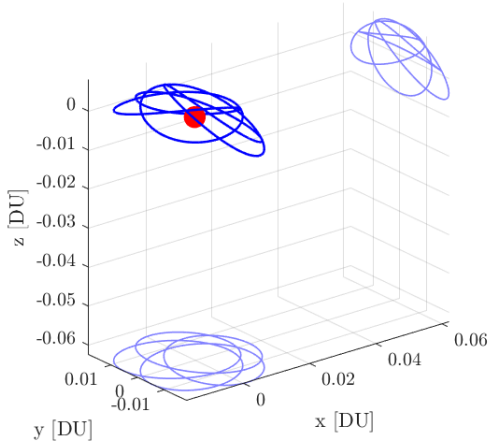

Figure 3.12: 4:1 artificial RTO at Apollo with $\alpha = 70°$, $\delta = 0°$.

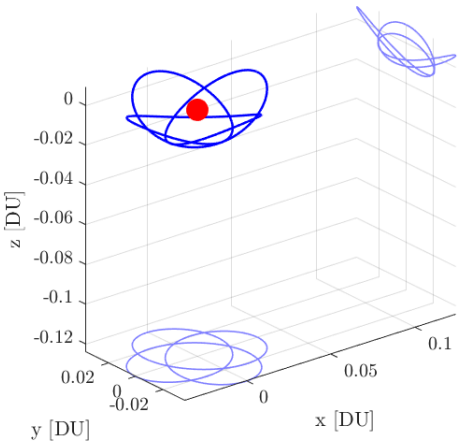

Figure 3.13: 3:1 artificial RTO at Apophis with $\alpha = -85°$, $\delta = 0°$.

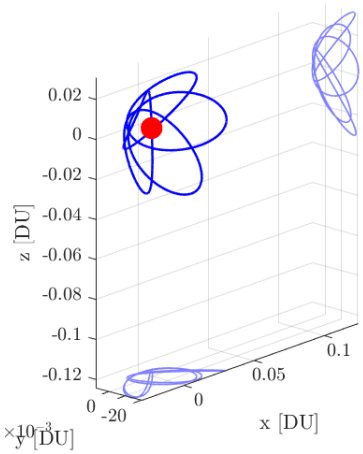

Figure 3.14: 5:1 artificial RTO at Apophis with $\alpha = 0°$, $\delta = 85°$.

It is important to notice that by adjusting the values for α and δ these orbits can have very similar shapes and size, with respect to the asteroid, despite there being difference of orders of magnitude between the various normalized SRP acceleration. Acceleration at Apophis, which starts with $k = 39642$, is reduced to $k\cos^2\alpha = 301$, with $\alpha = 85°$, a value similar to that of Eros. The same happens for Apollo, which needs smaller values for the angles, since it starts at $k = 6907$. Eros technically does not need to greatly reduce the SRP effect.

3.3. Variable-orientation RTOs

RTOs have been shown to exist in a highly perturbed environment with very strong SRP with the sail inclined relative to the terminator plane; however, it would still be useful to identify RTOs lying within the terminator plane. The variable orientation control presented in Section 2.2.3 greatly reduces the effect of SRP while still maintaining the orbits in the terminator plane. With the same initial conditions as Equation 3.48 and the correct differential correction scheme, a family of STOs can be generated. Figures 3.16 and 3.15 show two examples. Unlike the family of orbits presented in Section 3.1.4, these families seem to stop abruptly in the unstable regime. However, the stability indices seem to follow a behavior similar to that in Figure 3.6 before stopping. Another observable trend is that, as the angle α_v increases, the orbits remain closer to the asteroid.

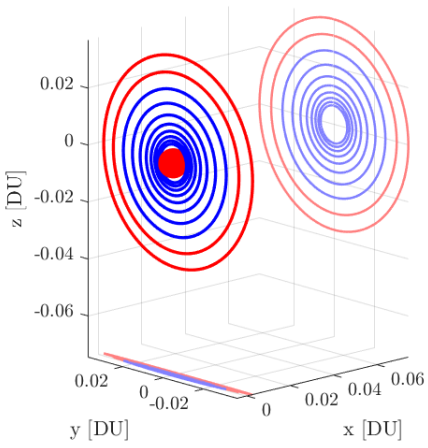

Figure 3.15: STOs family at Apophis with $\alpha_v = 84°$.

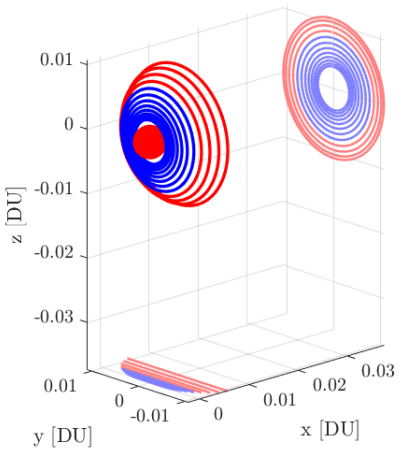

Figure 3.16: STOs family at Apollo with $\alpha_v = 40°$.

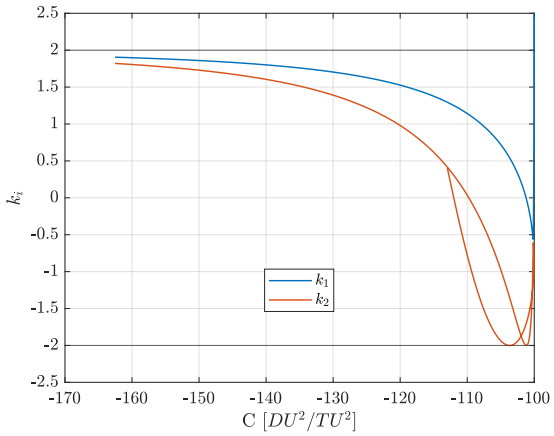

Figure 3.17: Stability indices for STOs at Apollo with $\alpha_v = 40°$.

From this point onward, the procedure follows the same steps as for fixed-orientation orbits, although significantly more trial and error was required when using the simple shooting method. Furthermore, due to the formulation of the correction scheme in Equation 2.43, the search can be terminated after half an orbit, since there is no constraint that forces the trajectory to end where it started. The orbit can still be closed by doubling the period; however, this implies that the resulting bifurcation is different from the intended one. For instance, a 3:1 bifurcation would instead appear as a 6:1, which can be identified by its period. In addition, as α_v increases, the resulting orbits tend to become broader compared to traditional RTOs.

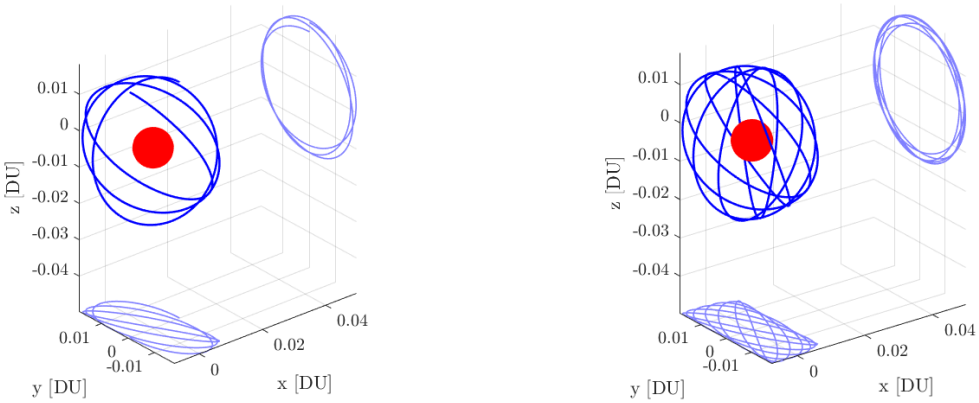

Figure 3.18: Half and full 6:1 RTO at Apophis with $\alpha_v = 82°$, found searching for a 3:1.

This behavior was observed for higher α_v, however the reasons why it occurs requires more investigation on the dynamics of the variable-orientation control. Here are more examples:

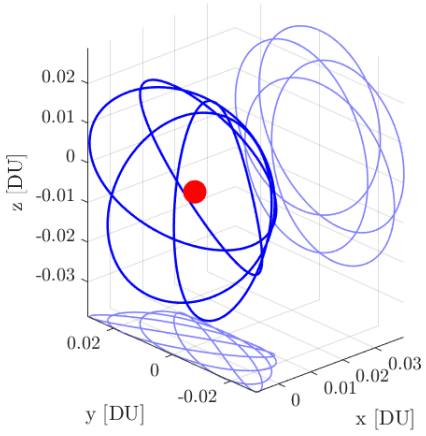

Figure 3.19: 4:1 RTO at Eros with $\alpha_v = 40°$.

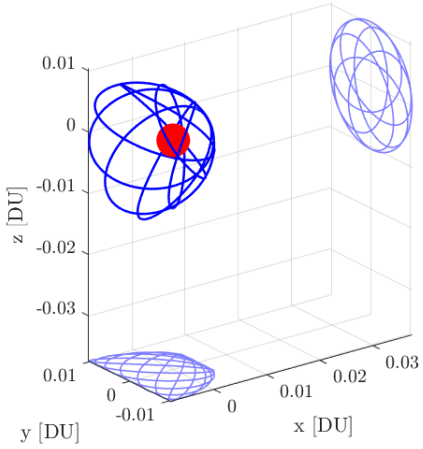

Figure 3.20: 6:1 RTO at Apollo with $\alpha_v = 60°$, found searching for a 3:1.

In this case, the correct resonance was found for Eros with $\alpha_v = 40°$, but not for Apollo. Eros orbit seems to have broader petals with respect to typical RTOs and this might be the effect of the variable-orientation control. In Figures 3.21 and 3.22, this behavior can be better visualized for very high α_v at Apophis.

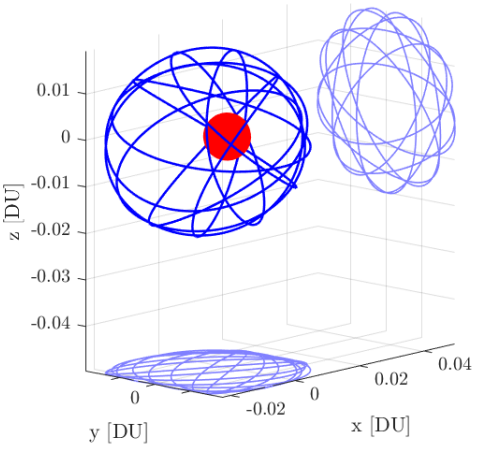

Figure 3.21: 8:1 RTO at Apophis with $\alpha_v = 84°$, found searching for a 4:1.

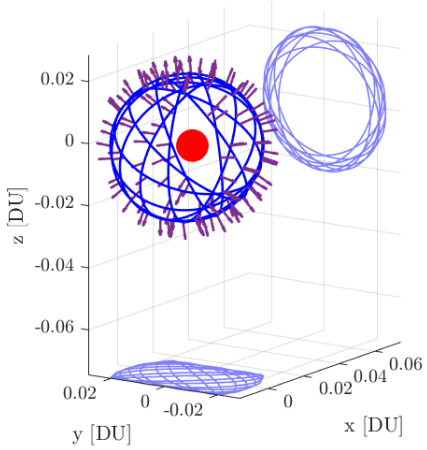

Figure 3.22: 8:1 RTO at Apophis with $\alpha_v = 84°$, found searching for a 4:1, with solar sail normal plotted over time.

3.4. Linear stability analysis

A brief linear stability analysis is conducted on the family of orbits and compared with typical RTOs behavior. Artificial RTOs share the same trend, with one of the indices always being equal to 2 and the other slowly increasing, as can be seen from Figures 3.23 and 3.24, while the family of orbits obtained with the variable-orientation control show a slightly different trend. They seem to go up and down much more quickly than the other families and the continuation stops abruptly. In fact, for these orbits convergence issues arise after a certain value of C, while the numerical continuation of the other two families did not provide any problem.

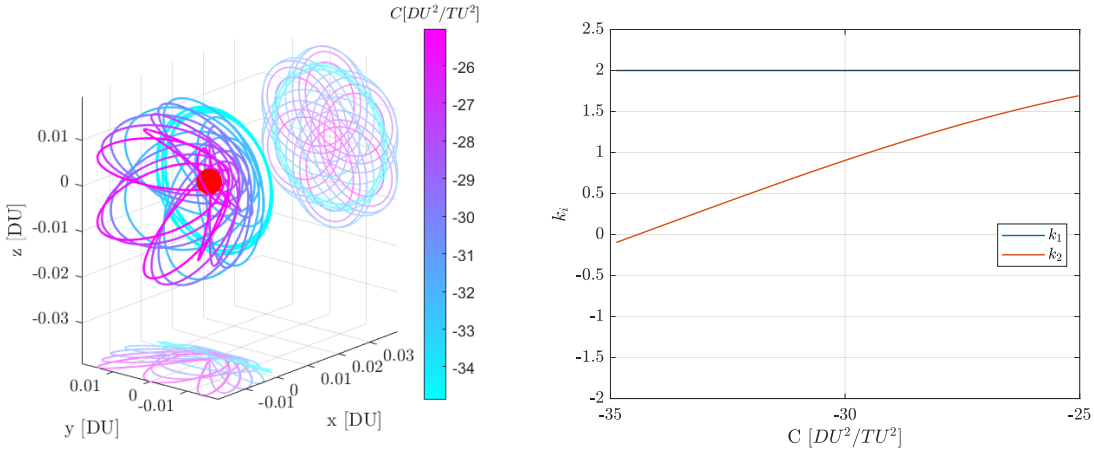

Figure 3.23: Family of 5:1 RTOs at Eros with and stability indices.

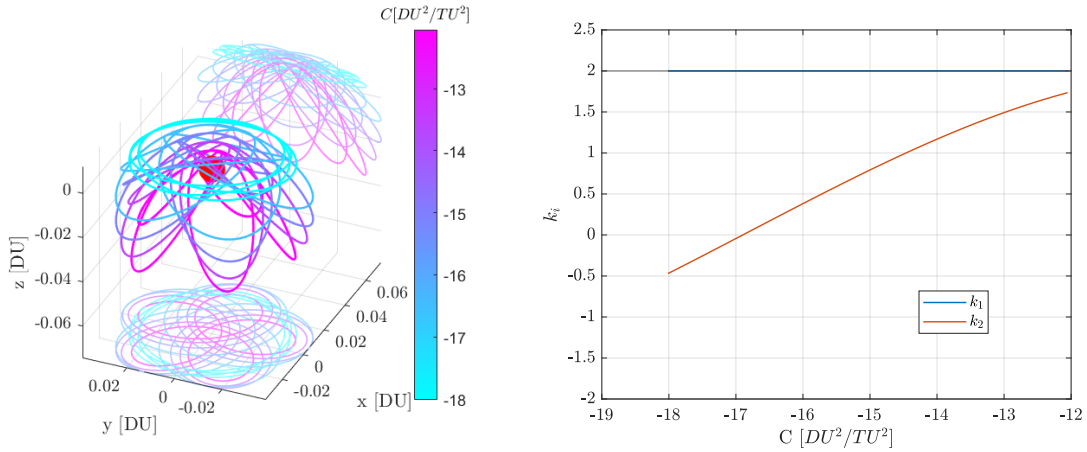

Figure 3.24: Family of 4:1 artificial RTOs at Apophis with $\alpha = 86°$, $\delta = 0°$ and stability indices.

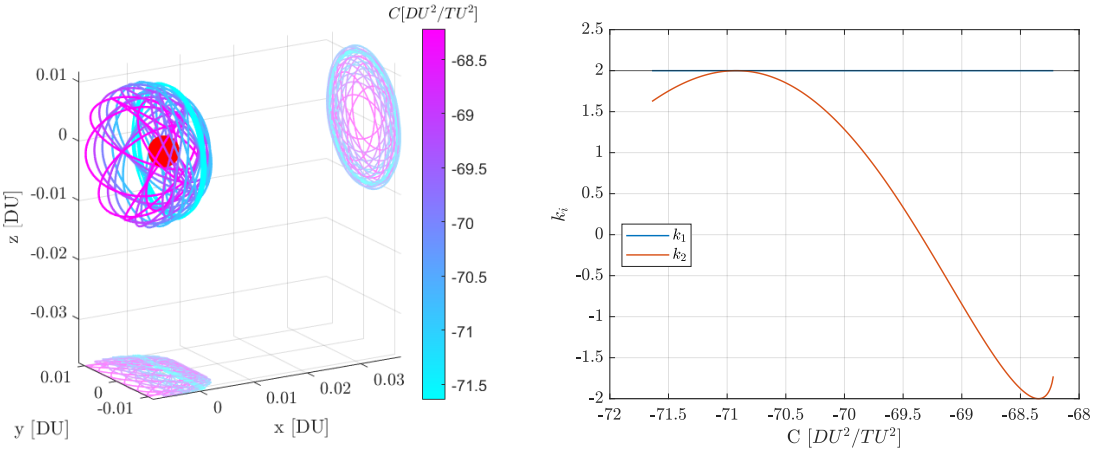

Figure 3.25: Family of 6:1 RTOs at Apollo with $\alpha_v = 60°$ and stability indices.

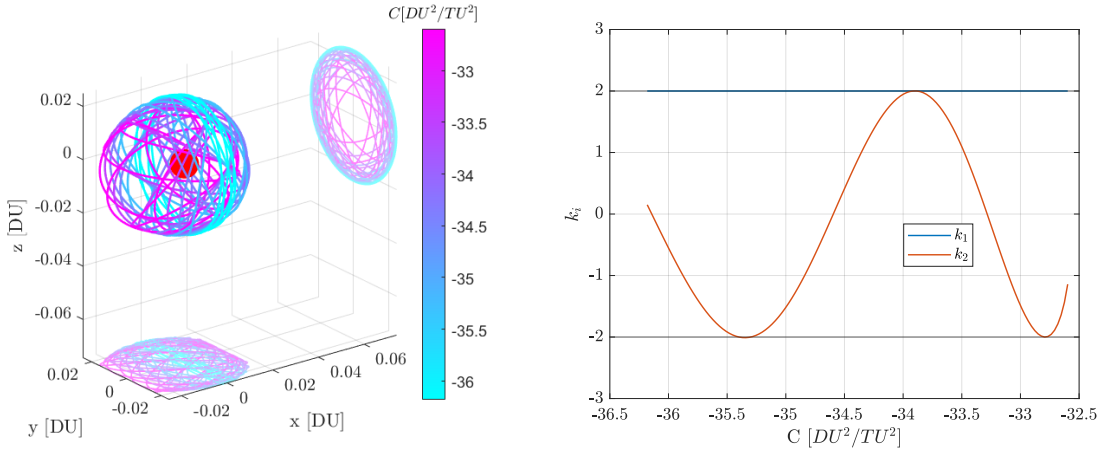

Figure 3.26: Family of 6:1 RTOs at Apophis with $\alpha_v = 84°$ and stability indices.

4 | Quasi Terminator Orbits

4.1. Parabolic coordinates and closed-form solution

This section will present a method for computing QTOs in a closed-form solution, starting from the static perturbed 2-Body problem presented in Section 2.1.2, by following the works of McInnes [29] and Damme and Oberst [26]. A set of parabolic coordinates (ξ, η, θ) is introduced as:

$$\rho = \xi\eta, \quad x = \frac{1}{2}(\xi^2 - \eta^2), \quad \dot{\rho} = \dot{\xi}\eta + \dot{\eta}\xi, \quad \dot{x} = \dot{\xi}\xi - \dot{\eta}\eta \tag{4.1}$$

which makes the radius $r = \frac{1}{2}(\xi^2 + \eta^2)$. With this formulation, the Hamiltonian becomes:

$$H(\xi, \eta) = \frac{1}{2(\xi^2 + \eta^2)} \left(P_\xi^2 + P_\eta^2 + h_x^2 \left(\frac{1}{\xi^2} + \frac{1}{\eta^2} \right) \right) - \frac{2\mu_a}{\xi^2 + \eta^2} - \frac{a_{srp}}{2} \frac{\xi^4 - \eta^4}{\xi^2 + \eta^2} \tag{4.2}$$

where $P_\xi = \dot{\xi}(\xi^2 + \eta^2)$, $P_\eta = \dot{\eta}(\xi^2 + \eta^2)$ and $P_\theta = (\xi\eta)^2\dot{\theta} = \rho^2\dot{\theta}$. In particular, the potential expressed in parabolic coordinates is:

$$U(\xi, \eta) = -\frac{2\mu_a}{\xi^2 + \eta^2} - \frac{a_{srp}}{2} \frac{\xi^4 - \eta^4}{\xi^2 + \eta^2} \tag{4.3}$$

This point is important, as the condition for the separation of variables in these coordinates corresponds to a potential energy of the form [37]:

$$U = \frac{a(\xi) + b(\eta)}{\xi^2 + \eta^2} \tag{4.4}$$

Since the separation of variables is possible, the Hamilton-Jacobi method can be used by introducing a transforming function $S(t, \xi, \eta)$ of the form:

$$S(t, \xi, \eta) = -Et + P_\theta\theta + S(\xi) + S(\eta) \tag{4.5}$$

where E is the total energy. Because the Hamiltonian does not directly depend on time ($dH/dt = \partial H/\partial t = 0$), the total energy is conserved and can be obtained from the initial conditions:

$$E_0 = \frac{1}{2}\left(\dot{\rho}_0 + \dot{x}_0 + \frac{h_x^2}{\rho_0^2}\right) - \frac{\mu_a}{r_0} - a_{srp}x_0 \tag{4.6}$$

The transforming function is chosen such that $\partial S(t,\xi,\eta)/\partial t + H(\xi,\eta) = 0$, so that the resulting expression is:

$$-2E\xi^2 - 2E\eta^2 + P_\xi^2 + P_\eta^2 + P_\theta^2/\xi^2 + P_\theta^2/\eta^2 - 4\mu_a - a_{srp}(\xi^4 - \eta^4) = 0 \tag{4.7}$$

By introducing a separation constant Ψ, two equations are obtained:

$$P_\xi^2 - 2\xi^2 E - a_{srp}\xi^4 + P_\theta^2/\xi^2 - 4\mu_a = -\Psi \tag{4.8}$$

$$P_\eta^2 - 2\eta^2 E + a_{srp}\eta^4 + P_\theta^2/\eta^2 = \Psi \tag{4.9}$$

Setting the momenta P_ξ and P_η to zero, it is possible to find the values ξ and η of the parabola where the momenta vanish, trapping trajectories inside the parabolas. Two equations are obtained:

$$w_1(A) = A^3 + \frac{2}{a_{srp}}EA^2 + \frac{4\mu_a - \Psi}{a_{srp}}A - \frac{h_x^2}{a_{srp}} = 0 \tag{4.10}$$

$$w_2(B) = B^3 - \frac{2}{a_{srp}}EB^2 - \frac{\Psi}{a_{srp}}B + \frac{h_x^2}{a_{srp}} = 0 \tag{4.11}$$

where $A = \xi^2$ and $B = \eta^2$. Two of the three roots of $w_1(A)$ and $w_2(B)$ are the squared coordinates of the constraining parabolas ξ_1, ξ_2, η_1 and η_2, while the third solutions $\tilde{c}_1$ and $\tilde{c}_2$ are parasitic solutions and do not constrain the orbit. In order to design QTOs, some parameters must be decided first. In this case a_{srp} is fixed from the sailcraft geometry, while ρ_0 and x_0 can be imposed at the start to decide the maximum distance from the asteroid and even the minimum SBS angle, useful for observation purposes. Once x_0 and ρ_0 are fixed, ξ_1 and η_1 are also decided, however, it is possible to further restrict the choice of parameters by imposing either $\xi_1 = \xi_2$ or $\eta_1 = \eta_2$. This means that the orbit will be totally constrained on one parabola inside the Zero Velocity Line (ZVL). The orbits constrained on ξ are sun-side QTOs, while the orbits constrained on η are dark-side QTOs. Typically, sun-side QTOs are more useful for observation purposes, so

this work will focus on the case $\xi_1 = \xi_2$.

In order to obtain the remaining parameters h_x and η_2, the parasitic solutions $\tilde{c}_1$ and $\tilde{c}_2$ can be treated as free parameters. The coefficients of the cubic functions in Equations 4.10 and 4.11 are then equated to the following polynomials:

$$w_1(A) = (A - A_1)(A - A_2)(A - \tilde{c}_1) \tag{4.12}$$
$$w_2(B) = (B - B_1)(B - B_2)(B - \tilde{c}_2) \tag{4.13}$$

Then, equating coefficients of order 0 and 2 yields the linear system:

$$\begin{bmatrix} 1 & 0 & -A_1A_2 & 0 \\ 1 & 0 & 0 & B_1B_2 \\ 0 & 2 & 1 & 0 \\ 0 & -2 & 0 & 1 \end{bmatrix} \begin{pmatrix} h_x^2/a_{srp} \\ E/a_{srp} \\ \tilde{c}_1 \\ \tilde{c}_2 \end{pmatrix} = \begin{pmatrix} 0 \\ 0 \\ -A_1 - A_2 \\ -B_1 - B_2 \end{pmatrix} \tag{4.14}$$

where $A_1 = A_2$, B_1 and a_{srp} are already set. The first and third equations of this system yield:

$$h_x^2 = a_{srp}A_1A_2\tilde{c}_1 \tag{4.15}$$
$$E = -\frac{a_{srp}}{2}(A_1 + A_2 + \tilde{c}_1) \tag{4.16}$$

but the expression for the energy can be substituted with the one from Equation 4.6, with $\dot{\rho_0} = \dot{x}_0 = 0$:

$$E = \frac{h_x^2}{2\rho_0} - \frac{\mu_a}{r_0} - a_{srp}x_0 = -\frac{a_{srp}}{2}(A_1 + A_2 + \tilde{c}_1) \tag{4.17}$$

By substituting the expression for h_x from Equation 4.15 and rearranging the expression, $\tilde{c}_1$ is retrieved:

$$\tilde{c}_1 = -\frac{\frac{2\mu_a}{r_0 a_{srp}} + 2x_0 - A_1 - A_2}{1 + \frac{A_1A_2}{\rho_0^2}} \tag{4.18}$$

and can be substituted in Equation 4.15 to obtain the angular momentum and then the initial energy E and $\dot{\theta}_0 = h_x/\rho_0^2$. Then, to get the last parameter B_2, the second and fourth equations of the linear system yield:

$$h_x^2 = -a_{srp} B_1 B_2 \tilde{c}_2 \tag{4.19}$$

$$E = \frac{a_{srp}}{2}(B_1 + B_2 + \tilde{c}_2) \tag{4.20}$$

By equating h_x and E from Equations 4.15 and 4.16:

$$A_1 A_2 \tilde{c}_1 = -B_1 B_2 \tilde{c}_2 \tag{4.21}$$

$$A_1 + A_2 + \tilde{c}_1 = -B_1 - B_2 - \tilde{c}_2 \tag{4.22}$$

then, by expressing $\tilde{c}_2$ from Equation 4.22 and substituting it into Equation 4.21, the final expression to solve for B_2 is:

$$B_2^2 B_1 + B_2(A_1 B_1 + B_1 A_2 + B_1^2 + B_1 \tilde{c}_1) - A_1 A_2 \tilde{c}_1 = 0 \tag{4.23}$$

A similar method can be used when $\eta_1 = \eta_2$ for dark-side QTOs. The initial conditions can either be propagated with the static perturbed 2-Body problem dynamic, or transformed into cartesian coordinates, adimensionalized, and then propagated with the ANH3BP dynamic:

$$\mathbf{r}_0 = \begin{bmatrix} x_0/DU \\ \rho_0/DU \\ 0 \end{bmatrix}, \qquad \mathbf{v}_0 = \begin{bmatrix} 0 \\ 0 \\ \rho_0 \dot{\theta}_0 \cdot TU/DU \end{bmatrix} \tag{4.24}$$

By plotting the projection of the orbit in the ρ-x plane it is possible to visualize how the two parabolas constrain the orbit inside a ZVL, where the energy is the same as the initial one and along the line $\dot{\rho}_0 = \dot{x}_0 = 0$ to prevent escape. However, even if the ZVL is open, escape would be prevented by the two parabolas. Designing orbits in such a way, with the SRP acceleration already fixed, means that only ρ_0 and x_0 must be decided. For sun-side QTOs this means that the maximum distance from the asteroid and the minimum SBS angle ϕ can be decided beforehand with the initial conditions. Here are two examples at Eros with no solar sail control, the orbit is slightly off from the parabolas because the propagation is made with the ANH3BP dynamics, while the whole formulation was with another dynamics, however these effects are minimal.

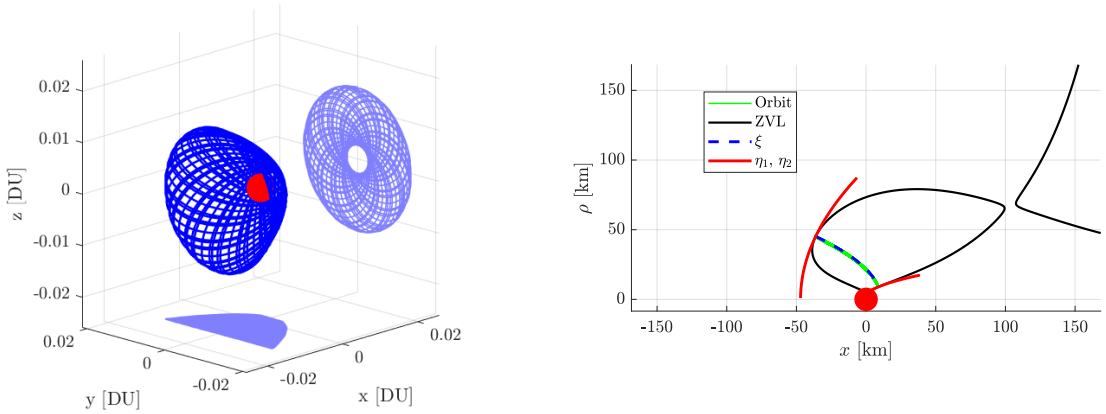

Figure 4.1: Sun-side QTO at Eros with $\rho_0 = 5.37 \cdot r_a$ and $x_0 = -4.3 \cdot r_a$.

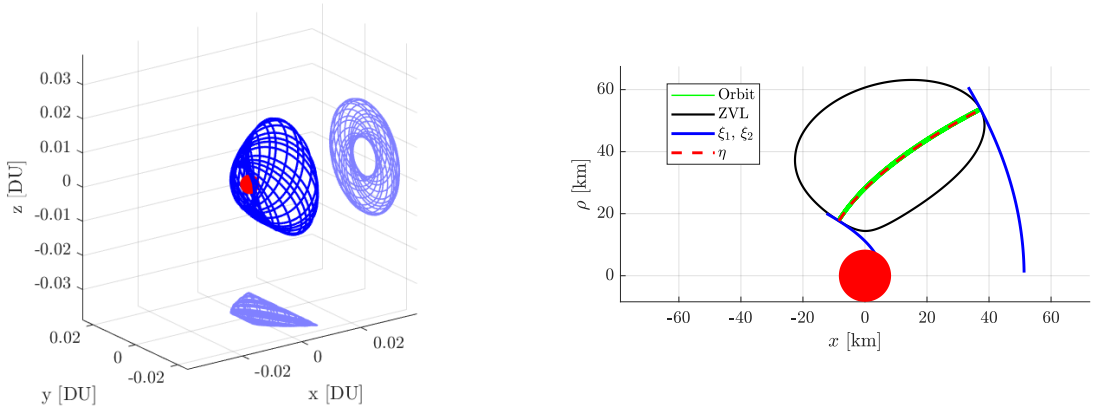

Figure 4.2: Dark-side QTO at Eros with $\rho_0 = 2.1 \cdot r_a$ and $x_0 = -1.1 \cdot r_a$.

4.2. Fixed-orientation QTOs

In the dynamics of the static perturbed 2-Body problem described by Equation 2.6, the sail acceleration is the only term that depends on the definition of the $\hat{x}$-axis. By defining the $\hat{x}$-axis as the normal to the sail, according to Equation 2.11, the same algorithm presented in the previous section can be applied to compute rotated QTOs under fixed-orientation control. Suitable values of α and δ can be selected to reduce the effects of SRP and to facilitate observation requirements. Once the initial conditions are non-dimensionalized, they are rotated using the matrices defined in Equation 3.50 and subsequently propagated. Here are some examples for Apophis and Apollo, showing the sail normal and the projection of the orbit into the ρ–$\hat{\mathbf{n}}$ plane, along with the corresponding parabolas and the ZVL:

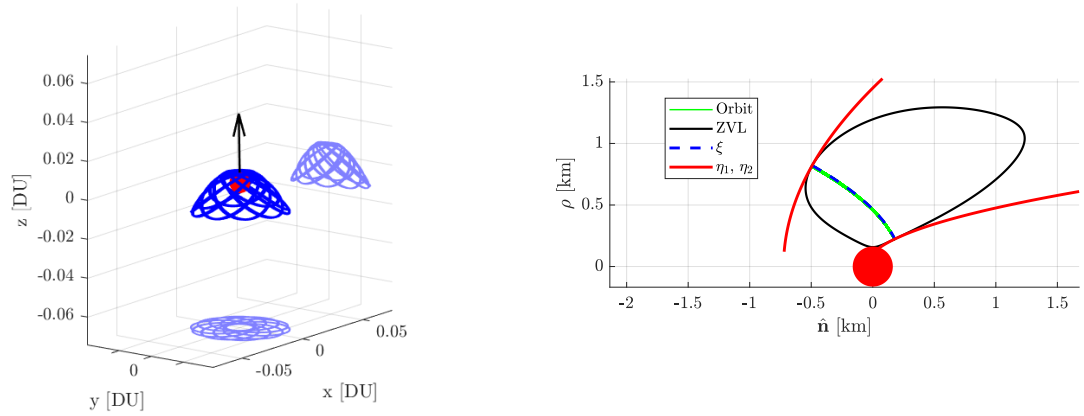

Figure 4.3: QTO at Apophis with $\alpha = 84°$ and $\delta = 45°$.

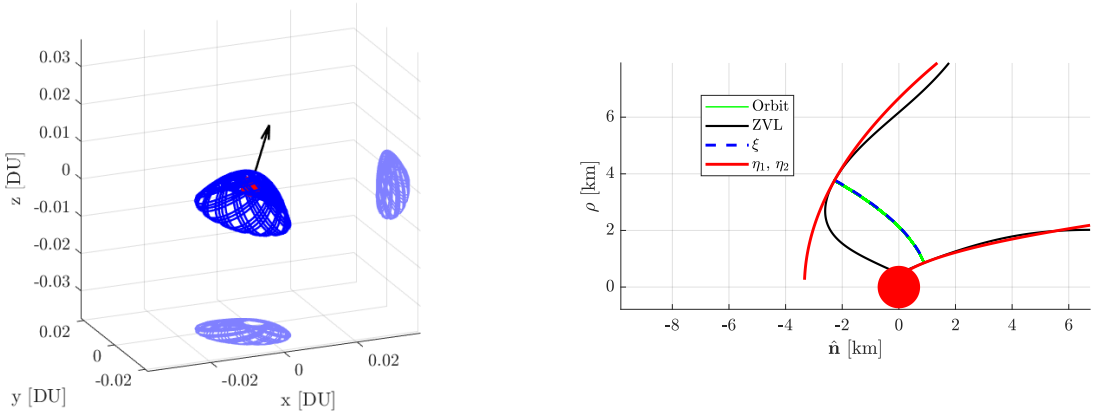

Figure 4.4: QTO at Apollo with $\alpha = 45°$ and $\delta = 45°$.

The additional terms present in the ANH3BP dynamic have a minimal impact on the final orbits; however, the initial choices for ρ_0 and x_0 do not represent anymore mapping parameters such as the SBS angle, so another method to choose them, along with α and δ must be defined. This will be done in Section 5.2.

4.3. Variable-orientation QTOs

When introducing the variable-orientation control, the Hamiltonian is changed to the one of Equation 2.19, with an added term. By expressing it in parabolic coordinates, the expression becomes:

$$\begin{aligned} H =& \frac{1}{2(\xi^2+\eta^2)}\left(P_\xi^2 + P_\eta^2 + h_x^2\left(\frac{1}{\xi^2}+\frac{1}{\eta^2}\right)\right) - \frac{2\mu_a}{\xi^2+\eta^2} \\ & - \frac{a_{srp}\cos^3\alpha_v}{2}\frac{\xi^4-\eta^4}{\xi^2+\eta^2} - \frac{a_{srp}\cos^2\alpha_v\sin\alpha_v}{\xi^2+\eta^2}(\xi^2+\eta^2)\xi\eta \end{aligned} \tag{4.25}$$

with the potential being:

$$U(\xi,\eta) = -\frac{2\mu_a}{\xi^2+\eta^2} - \frac{a_{srp}\cos^3\alpha_v}{2}\frac{\xi^4-\eta^4}{\xi^2+\eta^2} - \frac{a_{srp}\cos^2\alpha_v\sin\alpha_v}{\xi^2+\eta^2}(\xi^2+\eta^2)\xi\eta \tag{4.26}$$

In this case, the form of Equation 4.4 cannot be obtained, since the last term is multiplied by $\xi\eta$, which prevents variable separation in this dynamics. To establish a reliable approach for QTOs with variable-orientation control, a method based on the equilibrium energy will be formulated. First, equilibrium is imposed in Equation 2.20:

$$0 = -\frac{x_{eq}}{r_{eq}^3}\mu_a + a_{srp}\cos^3\alpha_v \tag{4.27}$$

$$0 = -\frac{\rho_{eq}}{r_{eq}^3}\mu_a + a_{srp}\cos^2\alpha_v\sin\alpha_v \tag{4.28}$$

Rearranging some terms to the opposite side and then performing a substitution yields:

$$r_{eq}^3 = \frac{x_{eq}\mu_a}{a_{srp}\cos^3\alpha_v} \tag{4.29}$$

$$\frac{\mu_a\rho_{eq}}{\mu_a x_{eq}}a_{srp}\cos^3\alpha_v = a_{srp}\cos^2\alpha_v\sin\alpha_v \tag{4.30}$$

which simplifies to:

$$\rho_{eq} = x_{eq}\tan\alpha_v \tag{4.31}$$

while the radius can be expressed as:

$$r_{eq} = \frac{x_{eq}}{\cos\alpha_v} \tag{4.32}$$

At this point, it is possible to obtain the coordinate x at equilibrium by substituting the radius expression in Equation 4.29 and the following equilibrium point is obtained:

$$x_{eq} = \sqrt{\frac{\mu_a}{a_{srp}}}, \quad \rho_{eq} = \sqrt{\frac{\mu_a}{a_{srp}}} \tan \alpha_v, \quad r_{eq} = \sqrt{\frac{\mu_a}{a_{srp}}} \frac{1}{\cos \alpha_v} \tag{4.33}$$

By substituting this coordinate into the energy equation while $\dot{\rho} = \dot{x} = \dot{\theta} = 0$, yields:

$$\begin{aligned} E_{eq} &= -\frac{\mu_a}{r_{eq}} - x_{eq} a_{srp} \cos^3 \alpha_v - \rho_{eq} a_{srp} \cos^2 \alpha_v \sin \alpha_v \\ E_{eq} &= -2\sqrt{\mu_a a_{srp}} \cos \alpha_v \end{aligned} \tag{4.34}$$

Now, after choosing some initial coordinates ρ_0 and x_0, with the same methodology shown in Section 4.1 as the shape and orientation are similar to traditional QTOs, an initial guess of the angular momentum h_x, and subsequently for $\dot{\theta}_0$, can be made by keeping the total energy the same as the equilibrium one:

$$h_{x,0} = \sqrt{2\rho_0^2 \left(E_{eq} + \frac{\mu_a}{r_0} + a_{srp} \cos^2 \alpha_v (x_0 \cos \alpha_v + \rho_0 \sin \alpha_v) \right)} \tag{4.35}$$

However, for the orbit to be feasible, ρ_0 and x_0 must lie within the ZVL corresponding to the equilibrium energy level with h_x set to zero. Two examples are shown for Eros and Apophis: the red cross marks the initial position, the black line represents the ZVL at the equilibrium energy for $h_x = 0$, while the remaining contours illustrate how the ZVL associated with the selected initial point evolves as h_x increases.

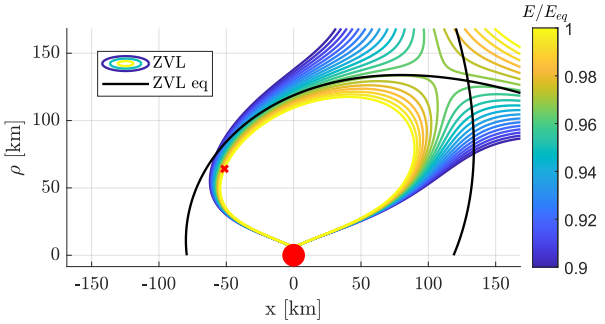

Figure 4.5: ZVL at Eros with $\alpha_v = 45°$.

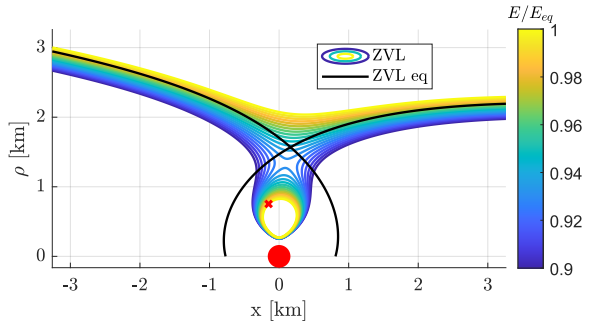

Figure 4.6: ZVL at Apophis with $\alpha_v = 84°$.

As h_x increases, the ZVL may open, allowing potential escape trajectories for the spacecraft. This is an important consideration, since an initial guess that guarantees orbital boundedness does not necessarily ensure suitability for observation purposes. For instance, in Figure 4.7, the initial orbit intersects Apophis, making it unfeasible for practical applications; therefore, adjustments to the initial angular momentum are required.

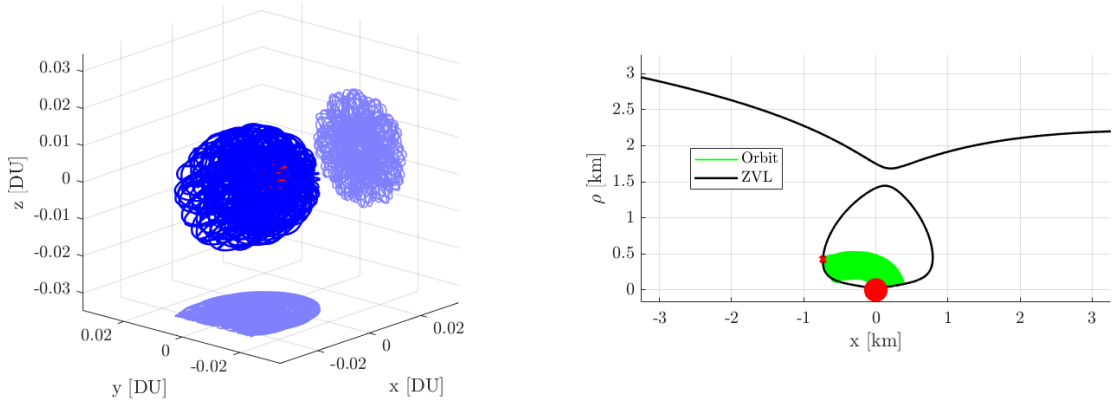

Figure 4.7: QTO at Apophis with $\alpha_v = 84°$ and $h_x = h_{x,0}$.

By increasing h_x, even though the ZVL opens, the orbit remains bounded, showing no escape even after several hundred days of propagation. Another noticeable effect is that the orbit expands upward from the initial point while becoming tighter, similarly to RTOs discussed in Section 3.3. However, some degree of trial and error is required to determine an appropriate increase in h_x, since an excessive value may lead to orbital escape.

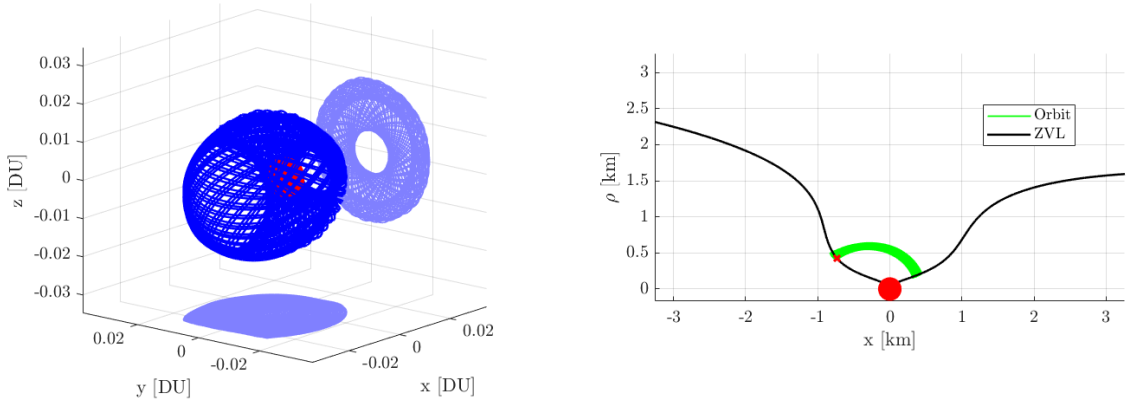

Figure 4.8: QTO at Apophis with $\alpha_v = 84°$ and $h_x = 2.4 \cdot h_{x,0}$.

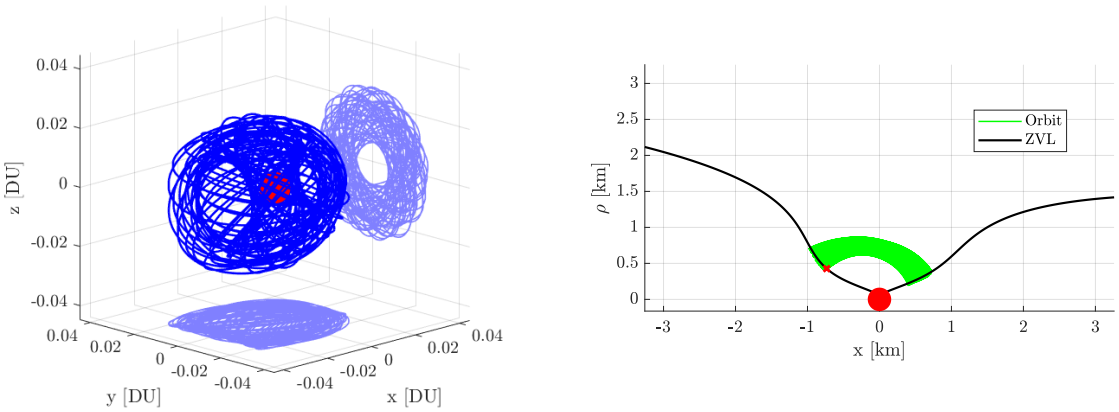

Figure 4.9: QTO at Apophis with $\alpha_v = 84°$ and $h_x = 2.7 \cdot h_{x,0}$.

It is also possible to adjust the value of h_x to obtain a tighter orbit, even when the trajectory does not initially intersect the asteroid. This is particularly useful for QTOs very similar to STOs, where maintaining a nearly constant distance from the small body is desirable. It is worth noting that, in this case, the optimal increase in h_x was achieved much earlier than in the previous example, despite identical control angles and asteroid parameters. This difference arises from the significantly different initial conditions for ρ_0 and x_0.

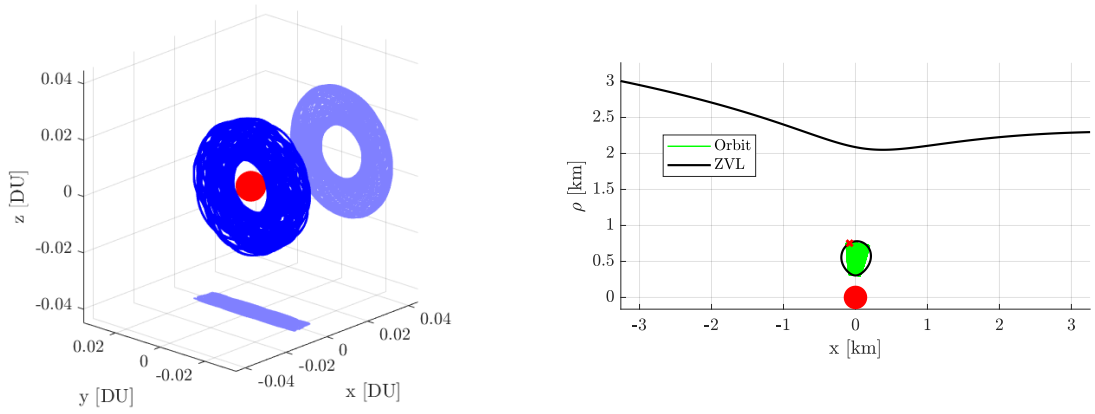

Figure 4.10: QTO at Apophis with $\alpha_v = 84°$ and $h_x = h_{x,0}$.

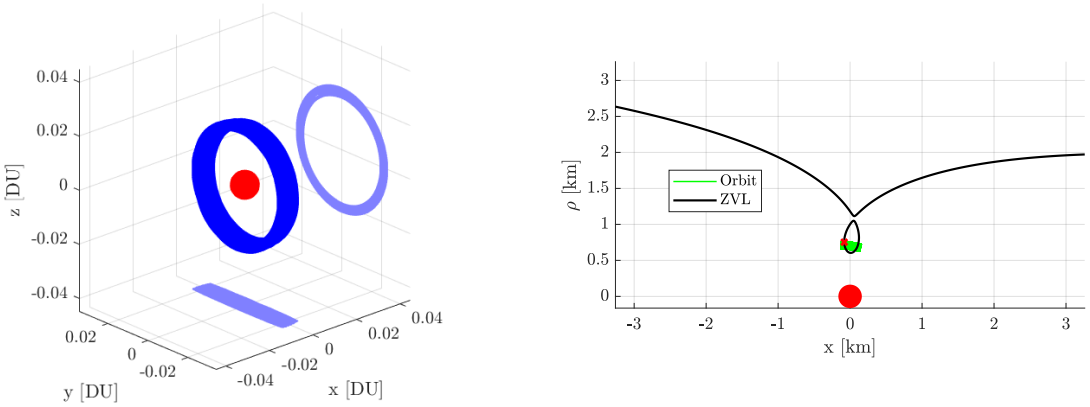

Figure 4.11: QTO at Apophis with $\alpha_v = 84°$ and $h_x = 1.2 \cdot h_{x,0}$.

In some cases, it is necessary to decrease the value of h_x to maintain approximately the same distance from the asteroid throughout the orbit, again through a process of trial and error. The reasons behind these different behaviors, depending on the initial conditions, control angle, and asteroid, are not yet fully understood and would require further investigation.

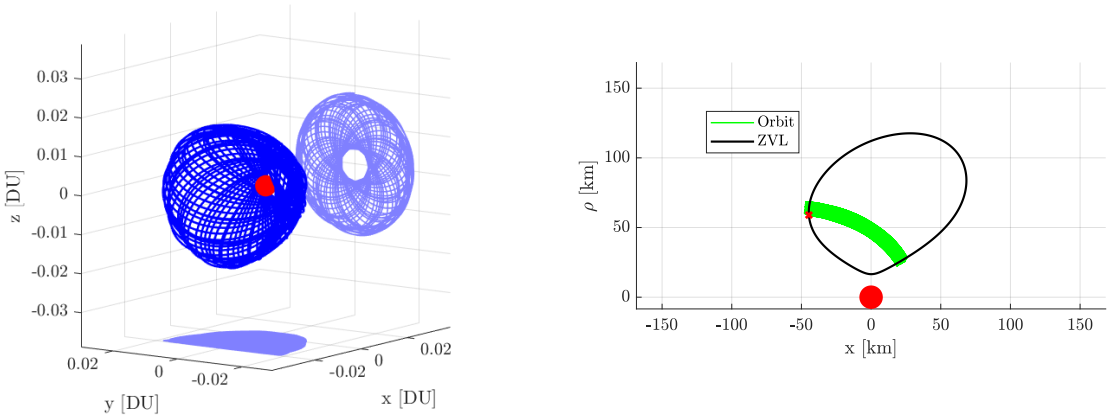

Figure 4.12: QTO at Eros with $\alpha_v = 50°$ and $h_x = h_{x,0}$.

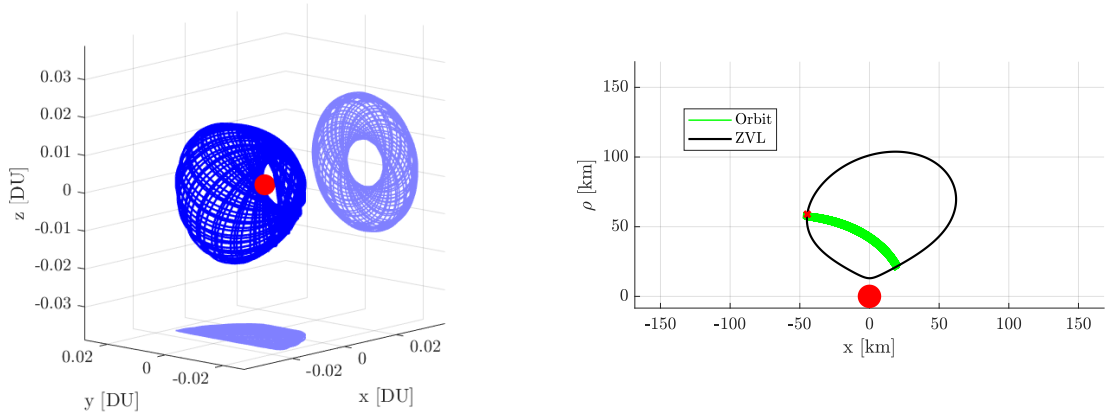

Figure 4.13: QTO at Eros with $\alpha_v = 50°$ and $h_x = 0.9 \cdot h_{x,0}$.

An interesting type of orbit was identified for α_v values in the range of 40°–60°. Due to the position of the equilibrium point and the resulting shape of the ZVL, the trajectory appears to bounce back and forth within the ZVL without escaping, resembling two distinct QTOs intersecting each other. However, the stability of this orbit is very low, as even small perturbations can lead to escape; in fact, minimal variations in h_x were sufficient to cause the orbit to become unbounded.

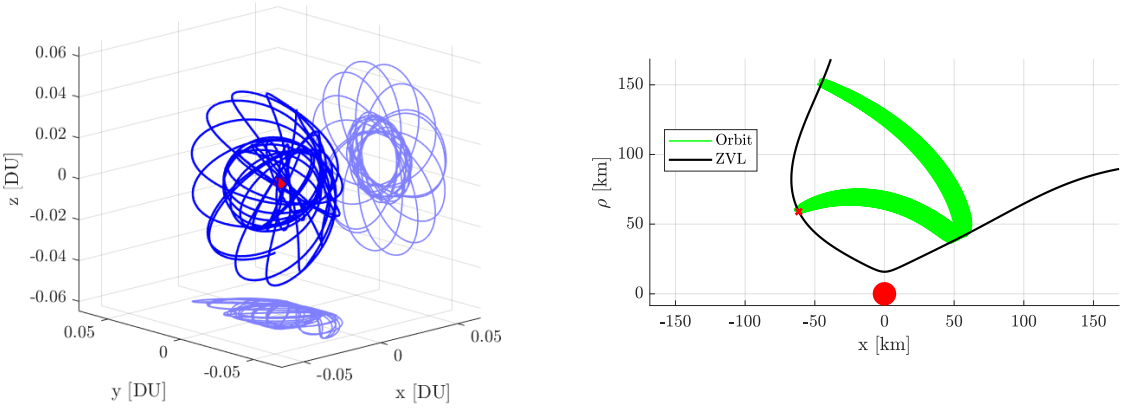

Figure 4.14: QTO at Eros with $\alpha_v = 50°$ and $h_x = 1.435 \cdot h_{x,0}$.

5 | Critical discussion

5.1. Non-ideal sail effects

In this section, the effects of a non-ideal sail where there is absorption will be studied for both types of sail control.

5.1.1. Effects on fixed-orientation control

The main effect of the more general sail model described in Section 2.2.4 is the introduction of an absorption term along the $\hat{x}$-axis, which causes the sail's normal vector to deviate from the acceleration vector. This represents a significant change, since all the orbits obtained under the fixed-orientation control are strictly dependent on the direction of $\hat{\mathbf{n}}$. The expression of the acceleration vector from Equation 2.21 can be rewritten as:

$$\mathbf{a}_{\text{srp}} = \bar{k} \cos^2 \bar{\alpha} \cos^2 \bar{\delta} \begin{bmatrix} \cos \bar{\alpha} \cos \bar{\delta} \\ \cos \bar{\alpha} \sin \bar{\delta} \\ \sin \bar{\delta} \end{bmatrix} \tag{5.1}$$

where the overbars denote the corresponding quantities in the ideal sail case. The additional force term affects not only the direction of the acceleration but also, to a lesser extent, its magnitude, which assumes a slightly different value. By employing the previously obtained RTOs solutions and simply modifying the dynamics to incorporate the new sail model, the correction scheme failed to converge to new periodic orbits. This is due to the large discrepancy between the sail's normal vector and the actual acceleration direction, which exceeds the method's convergence capability. Consequently, the search algorithm must be reformulated to include, from the outset, the additional variables associated with the non-ideal sail in order to successfully compute periodic orbits. These effects are even more evident in the case of QTOs, where the same issue arises if the initial conditions derived for an ideal sail are used for a non-ideal one with identical control angles but different ξ_r. Two examples are shown for different value of the SRP acceleration and the control angles:

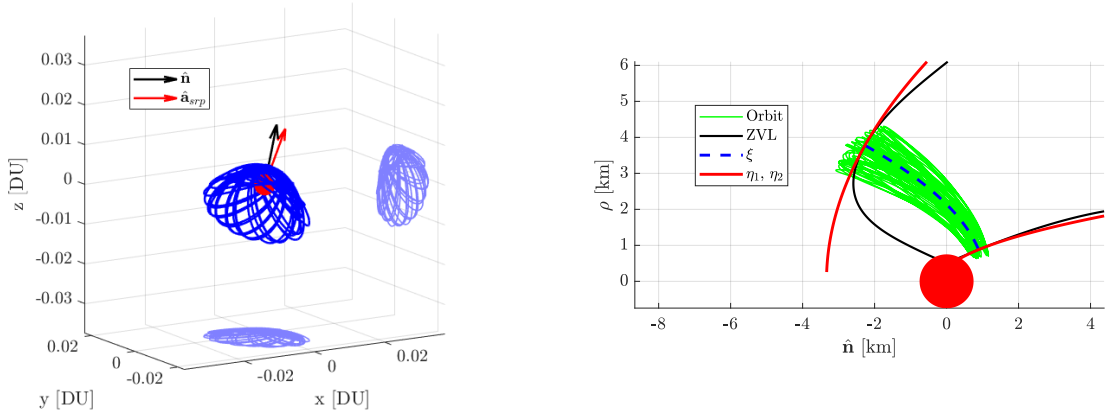

Figure 5.1: Apollo QTO with $\alpha = 45°$, $\delta = 45°$, $\bar{\alpha} = 40°$, $\bar{\delta} = 36.5°$ and $\xi_r = 0.85$.

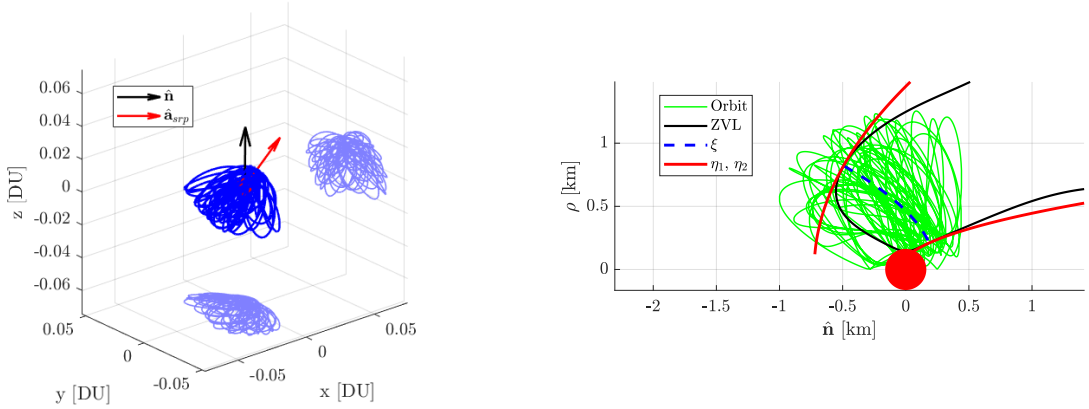

Figure 5.2: Apophis QTO with $\alpha = 84°$, $\delta = 45°$, $\bar{\alpha} = 38°$, $\bar{\delta} = 3.3°$ and $\xi_r = 0.85$.

As can be observed, the orbit obtained for Apollo deviates slightly from the ideal case but remains usable, with the new orientation angles differing only marginally from the ideal ones. In contrast, the orbit at Apophis is totally unfeasible—impacting the asteroid—and the corresponding angles differ significantly from the ideal configuration. This indicates that the effects of the non-ideal sail become more pronounced at higher angles. Nevertheless, by adjusting the initial conditions to be oriented for the new resultant acceleration in the rotation matrices, it is still possible to obtain orbits aligned with this vector, although their orientation will differ from the desired one of the control angles.

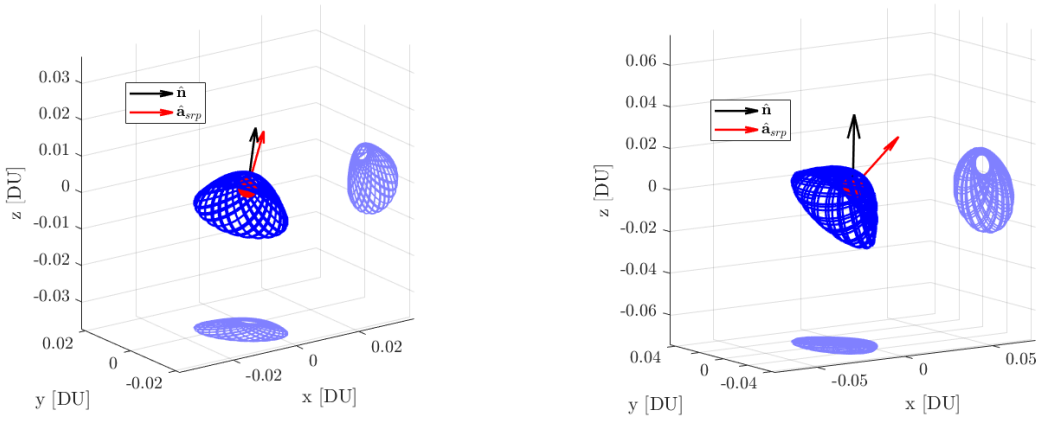

Figure 5.3: Adjusted QTOs at Apollo and Apophis.

To better analyze these effects and quantify the angle variations, the definition of the sail normal from Equation 2.14 is used. In this form, the absorption term affects only the pitch angle, leaving the clock angle unchanged. Even if another definition of the normal is employed, the angles remain fixed and can be easily converted from one definition to the other as:

$$\alpha_2 = \arcsin(\sin\alpha_1 \cos\delta_1), \quad \delta_2 = \arctan(\tan\alpha_1 \sin\delta_1) \tag{5.2}$$

where the subscript $(\cdot)_1$ refers to the angles defined for the normal according to Equation 2.14, and the subscript $(\cdot)_2$ corresponds to those in Equation 2.11. In the following figures, the change of the acceleration angle $\bar{\alpha}$ with respect to the sail pitch angle is presented for different value of ξ_r:

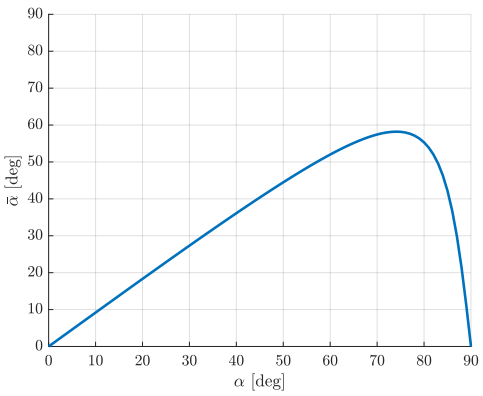

Figure 5.4: $\xi_r = 0.85$.

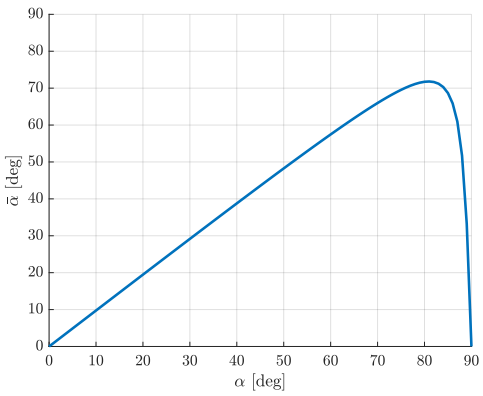

Figure 5.5: $\xi_r = 0.95$.

As shown, the trend follows an approximately linear behavior up to a maximum attainable angle for the acceleration vector, after which it decreases to zero. This implies that some of the orbits obtained in Sections 3.2 and 4.2 are not feasible. For instance, with a reflectivity coefficient of 0.85, the maximum achievable angle is slightly below 60° and occurs only when the control angle is around 75°. However, when selecting the control angles, the reduction of SRP effects must be considered first: for Apophis, only control angles above 82° yielded feasible orbits, meaning that the actual angles of the acceleration vector will always remain below 50°. These effects are mitigated for higher reflectivity coefficients. The following figures better visualize the possible obtainable orbits orientation for non-ideal sails and their difference with respect to ideal ones:

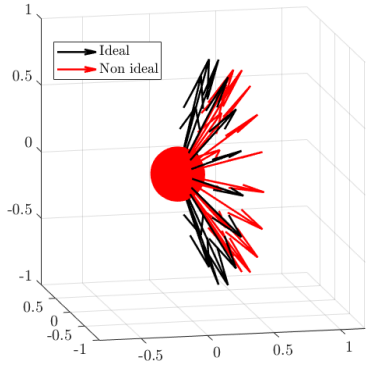

Figure 5.6: Ideal and real orbit orientations $\alpha = 70°$, $\bar{\alpha} = 57.44°$, $\xi_r = 0.85$.

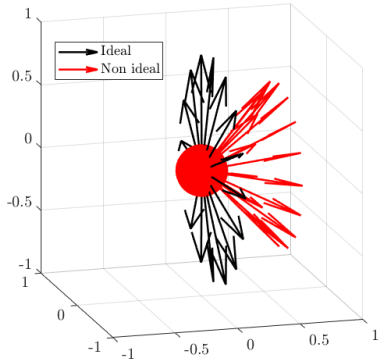

Figure 5.7: Ideal and real orbit orientations $\alpha = 84°$, $\bar{\alpha} = 46.35°$, $\xi_r = 0.85$.

The difference between the ideal magnitude and the real one is also shown in the following figure:

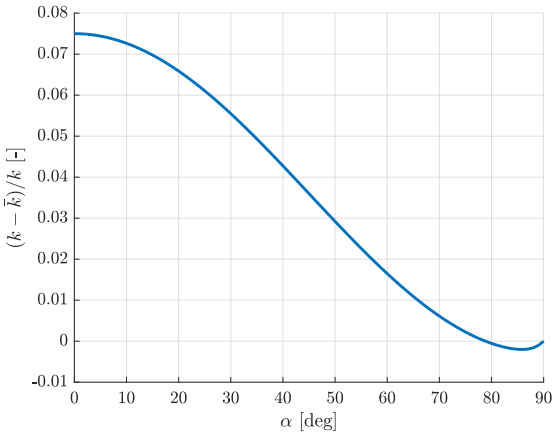

Figure 5.8: Difference between ideal and non-ideal ($\xi_r = 0.85$) magnitude acceleration.

The difference between the two is approximately 7 % at the beginning, mainly due to the reduced pressure resulting from the lower reflectivity coefficient. However, as the angle increases, the additional component along the $\hat{x}$-axis becomes more significant, reducing the difference in magnitude toward the highest values of α. The following figure illustrates how the ratio of the acceleration components remains constant along the $\hat{y}$ and $\hat{z}$ axes, while it varies continuously along the $\hat{x}$ direction.

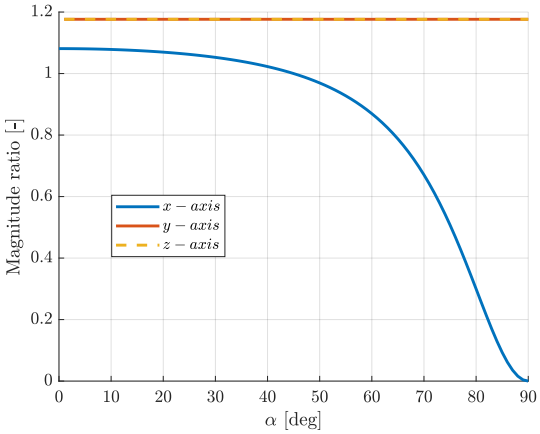

Figure 5.9: Ratio between ideal and non-ideal components of acceleration.

In general, all the work carried out on fixed-orientation orbits can be extended to any type of sail model, provided that the acceleration vector and its corresponding orientation angles are considered instead of the sail normal.

5.1.2. Effects on variable-orientation control

Regarding the variable-orientation control, since the resulting orbits do not directly depend on the sail normal, introducing a non-ideal sail does not cause as many issues as in the fixed-orientation case. The initial conditions of RTOs obtained with the ideal model do not converge or yield periodic orbits when the non-ideal model is applied. In order to fix this issue the non-ideal sail model must be taken into account directly in the dynamics so that the simple shooting process and the correction scheme algorithm can adjust to its effects.

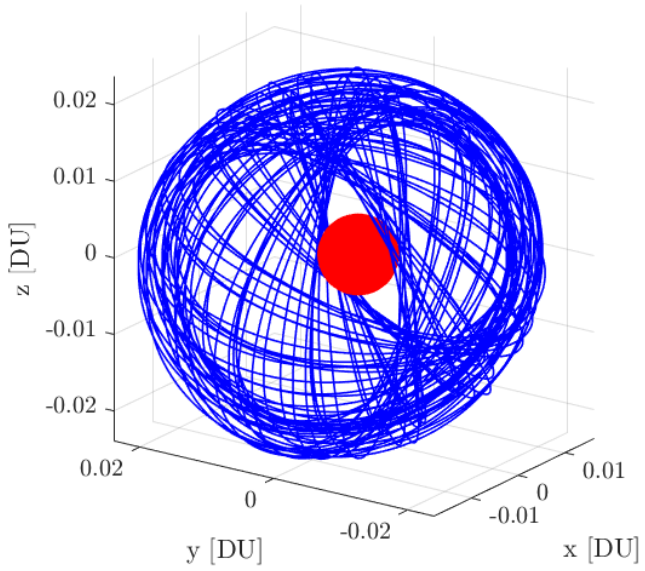

Figure 5.10: Initial conditions for a RTO with an ideal sail propagated at Apophis with $\alpha_v = 84°$ and $\xi_r = 0.85$.

The linear stability indices do not differ significantly from those obtained for this type of RTOs in Section 3.4, with one index remaining equal to 2 and the other oscillating near the stability boundaries. As for the other families of variable-orientation orbits, the continuation process was eventually stopped due to a lack of convergence beyond a certain point.

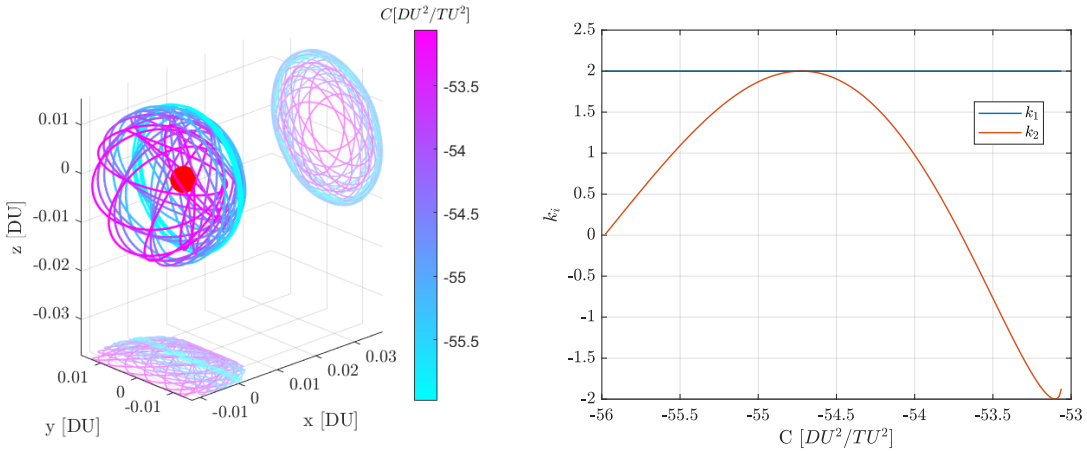

Figure 5.11: Family of 6:1 RTOs at Apollo with $\alpha_v = 65°$, $\xi_r = 0.85$ and stability indices.

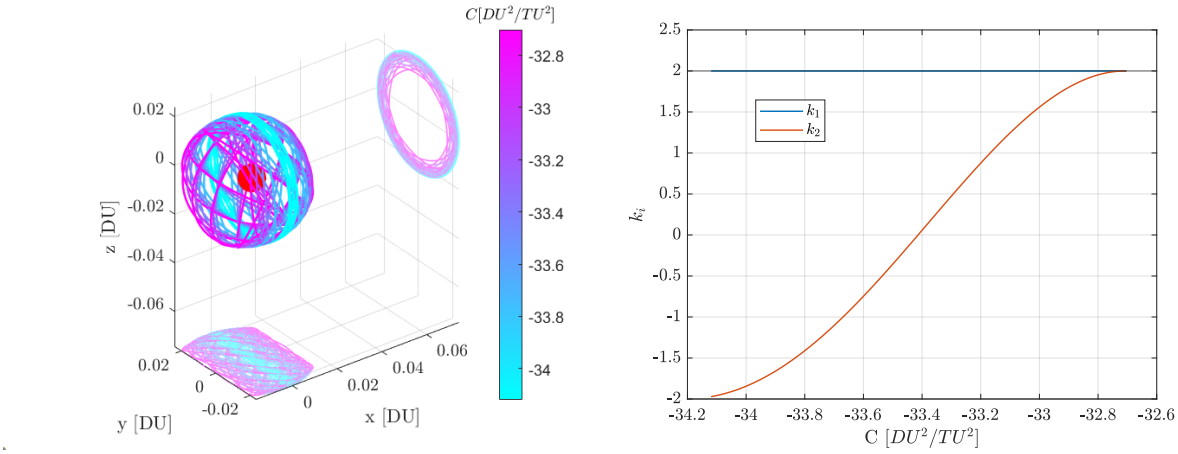

Figure 5.12: Family of 8:1 RTOs at Apophis with $\alpha_v = 84°$, $\xi_r = 0.85$ and stability indices.

Regarding the method to find QTOs discussed in Section 4.3, it needs to account for the non-ideal sail, which changes the dynamics and the energy to:

$$\begin{aligned}
\ddot{x} &= -\frac{\mu_a}{r^3}x + a_{srp}(\xi_r \cos^3\alpha_v + \frac{1}{2}(1-\xi_r)\cos\alpha_v) \\
\ddot{\rho} &= -\frac{\mu_a}{r^3}\rho + \frac{h_x^2}{\rho^3} + a_{srp}\xi_r \cos^2\alpha_v \sin\alpha_v \\
\ddot{\theta} &= -2\frac{\dot{\rho}}{\rho}\dot{\theta}
\end{aligned} \tag{5.3}$$

$$E = \frac{1}{2}\left(\dot{\rho} + \dot{x} + \frac{h_x^2}{\rho^2}\right) - \frac{\mu_a}{r} - x a_{srp}(\xi_r \cos^3\alpha_v + \frac{1}{2}(1-\xi_r)\cos\alpha_v) - \rho a_{srp}\xi_r \cos^2\alpha_v \sin\alpha_v \tag{5.4}$$

By following the same passages as for the ideal case, it is possible to retrieve the new coordinates at equilibrium, even though in this case the solution is not as compact as before:

$$x_{eq} = \sqrt{\frac{\mu_a}{a_{srp}(\xi_r \cos^3\alpha_v + \frac{1}{2}(1-\xi_r)\cos\alpha_v)(1+\epsilon^2)^{3/2}}}, \quad \rho_{eq} = x_{eq}\epsilon, \quad r_{eq} = x_{eq}(1+\epsilon^2) \tag{5.5}$$

where ϵ is a correction factor introduced to simplify the expressions:

$$\epsilon = \frac{\xi_r \cos\alpha_v \sin\alpha_v}{\xi_r \cos^2\alpha_v + \frac{1}{2}(1-\xi_r)} \tag{5.6}$$

Now, the equilibrium energy can be obtained by substituting the equilibrium point in Equation 5.4, after which the same procedure as in the ideal case can be followed. In the following figures, the ratio between non-ideal and ideal equilibrium coordinates and energy can be observed:

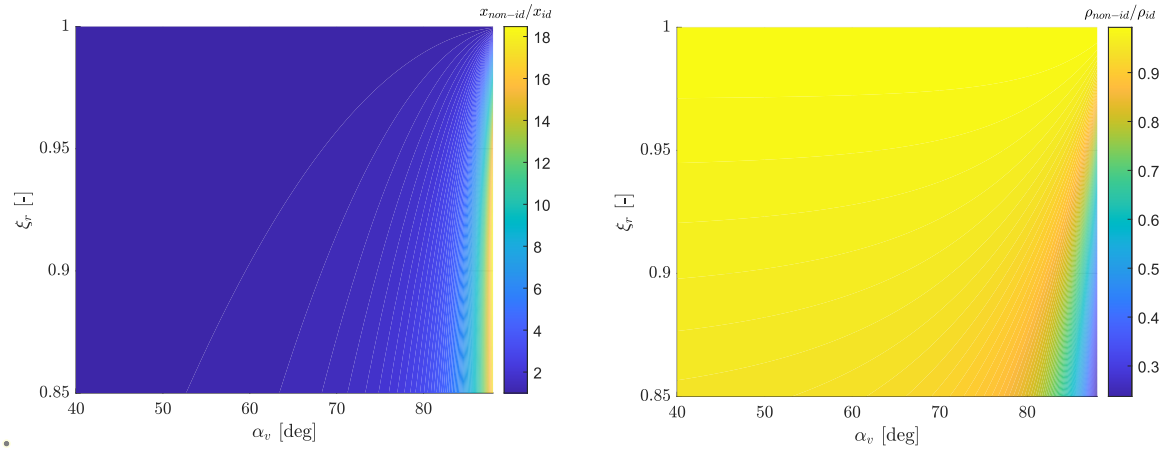

Figure 5.13: Ratio between non-ideal and ideal equilibrium point, x and ρ respectively.

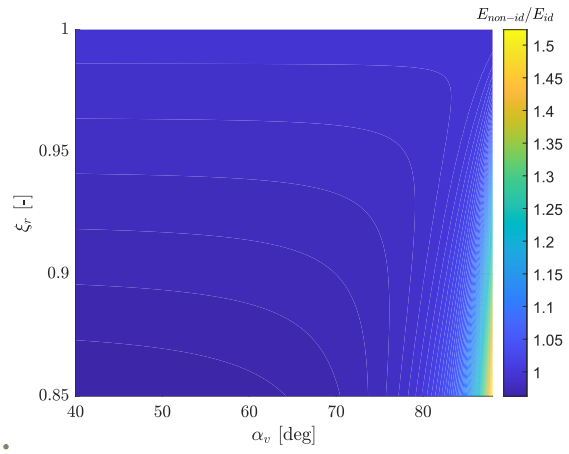

Figure 5.14: Ratio between non-ideal and ideal equilibrium energy.

The x coordinate of the equilibrium point increases significantly as the angle approaches $\alpha_v = 89°$, while ρ decreases, indicating that the ZVL of the equilibrium energy becomes thinner and more elongated along the $\hat{x}$-axis as shown in the following figures. The equilibrium energy slightly decreases for $\alpha_v < 80°$, but rises sharply for larger values. Nevertheless, all of these effects remain negligible until large values of α_v are reached.

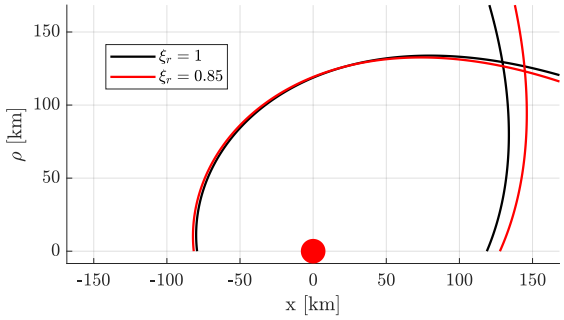

Figure 5.15: Ideal and non-ideal ZVL at Eros with $\alpha_v = 45°$.

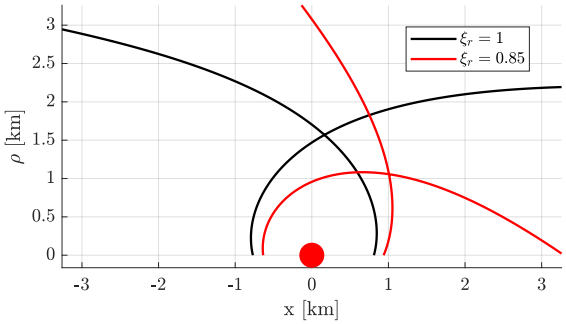

Figure 5.16: Ideal and non-ideal ZVL at Apophis with $\alpha_v = 84°$.

5.2. Mission applications and design

One of the most practical applications of these orbits is asteroid mapping, as their shape allows coverage of a large portion of the small body. For orbits using variable-orientation control, their geometry closely resembles that of traditional terminator orbits, so the same parameters—such as the SBS angle ϕ, period, and minimum and maximum distance from the asteroid—can be used as initial design references [27, 34, 38]. The only additional parameter to consider is the sail pitch angle, which must be tuned to mitigate SRP effects and thus extend the achievable distance from the small body.

More focus is placed on orbits with fixed-orientation control, as the selection of initial parameters affects the orbit characteristics differently from traditional RTOs and QTOs. For example, as discussed in Chapter 4, the choice of x_0 and ρ_0 determines ϕ_{min} for orbits in the terminator plane, whereas for artificial QTOs this value also depends on the control angles. It is important to note that the parameters x_0 and ρ_0 are not defined in the LVLH reference frame, but rather in the frame where the $\hat{x}$-axis is aligned with the SRP acceleration vector, before any rotation is applied to the initial conditions.

Here are some steps to follow when selecting the initial conditions for artificial QTOs described in Section 4.2:

1. Select α and δ to reduce the SRP and obtain a suitable value of k for a mapping orbit (typically between 20 and 200). For instance, starting from $k = 39642$ at Apophis, this value can be reduced either by setting $\alpha = \delta = 74.54°$ or $\alpha = 85.93°$, $\delta = 0°$.

2. Adjust the control angles according to the desired ϕ, the asteroid's rotation axis, or the target region to be mapped.

3. Choose x_0 to control the orbit amplitude, which also influences the minimum value of ϕ and the closest approach to the asteroid. It is generally recommended to set x_0 as a fraction of ρ_0.

4. Choose ρ_0 to set the desired maximum distance from the asteroid. Note that, with all other parameters fixed, increasing or decreasing ρ_0 allows finding orbits close to RTOs without any differential correction scheme. It is recommended to choose ρ_0 as a fraction of r_a.

All these choices can be refined through trial and error to identify the most suitable orbit for a given application. For instance, increasing ρ_0 decreases the number of petals in RTOs, and vice versa. Another useful parameter is the period between the maximum and minimum distance from the asteroid, which is closely related to the petal period of RTOs. Here is an example at Apophis:

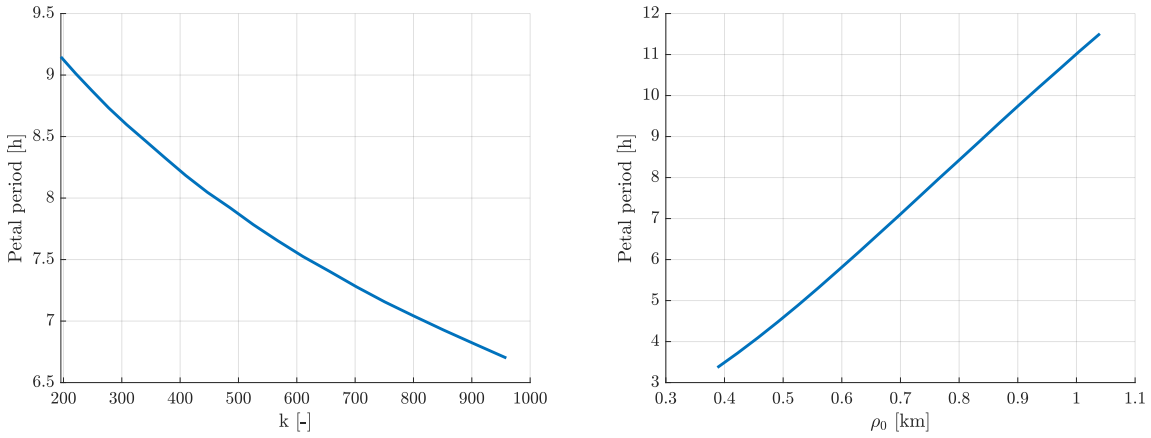

Figure 5.17: Petal period as a function of k and ρ_0.

As can be observed, when all other parameters are fixed, variations in ρ_0 have the strongest influence on this period, whereas changes in α and δ, which modify the magnitude of the SRP, have a slightly smaller effect. In contrast, varying x_0 does not provide any effective control over this period.

5.2.1. Apophis mapping

Now, some examples will be discussed considering Apophis as the target, illustrating the ground tracks with respect to both the Sun and the asteroid. A non-ideal sail with $\xi_r = 0.85$ is considered to obtain results that are more representative of realistic conditions.

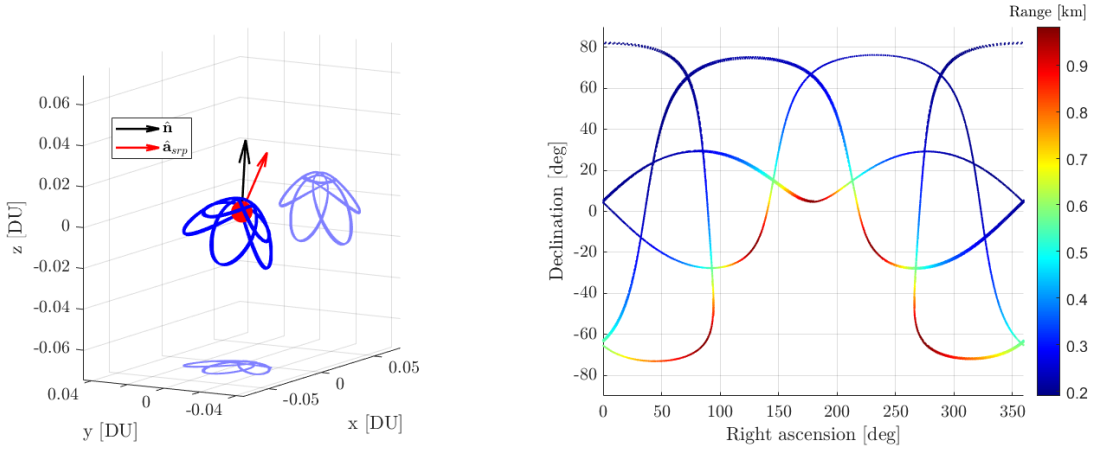

Figure 5.18: Orbit 1 at Apophis with 4:1 resonance with ground track relative to the Sun.

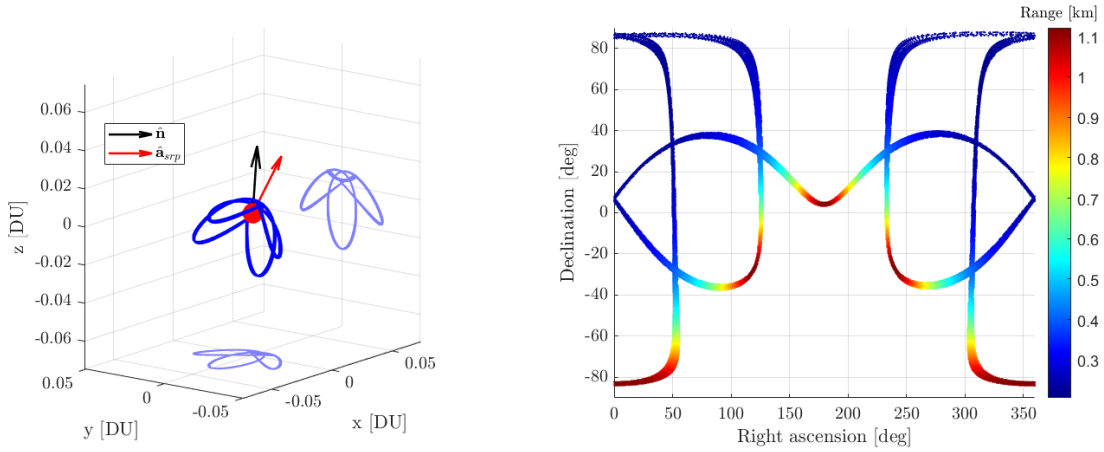

Figure 5.19: Orbit 2 at Apophis with 3:1 resonance with ground track relative to the Sun.

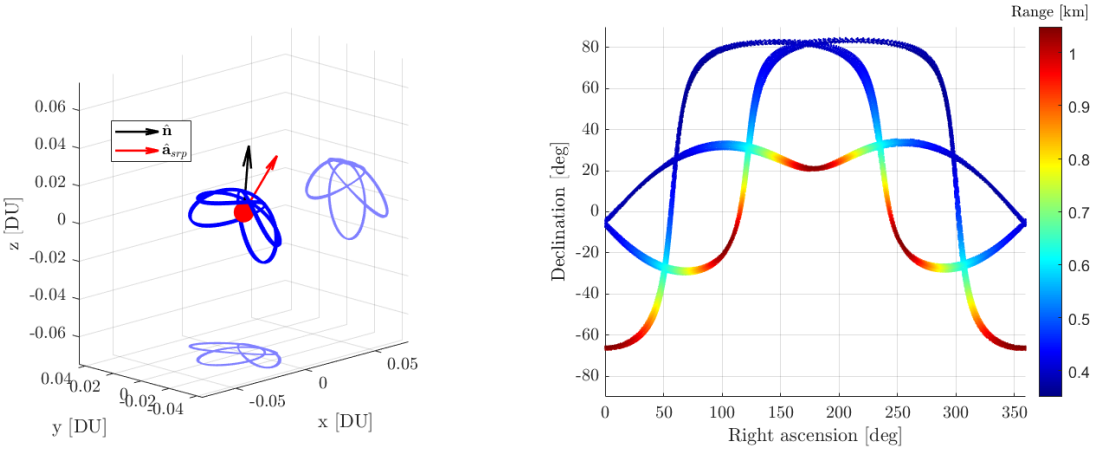

Figure 5.20: Orbit 3 at Apophis with 4:1 resonance with ground track relative to the Sun.

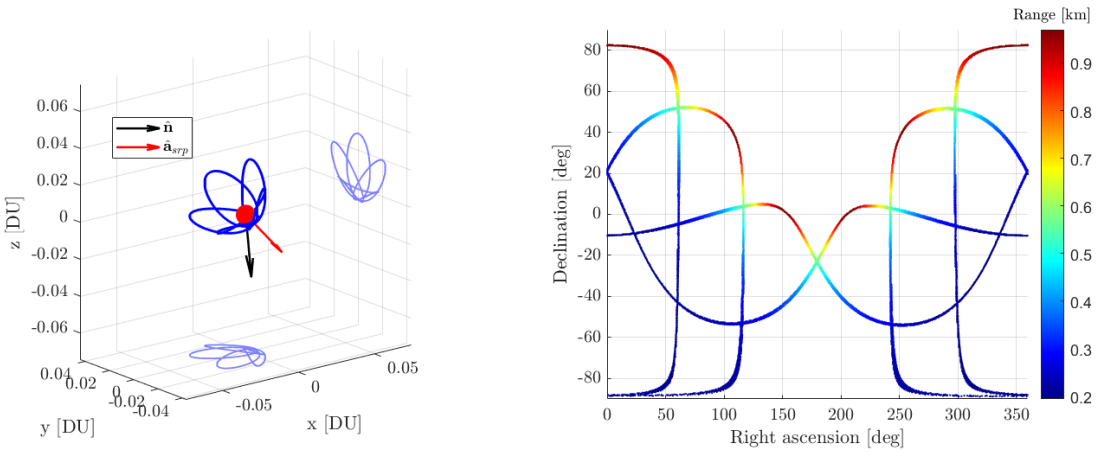

Figure 5.21: Orbit 4 at Apophis with 3:1 resonance with ground track relative to the Sun.

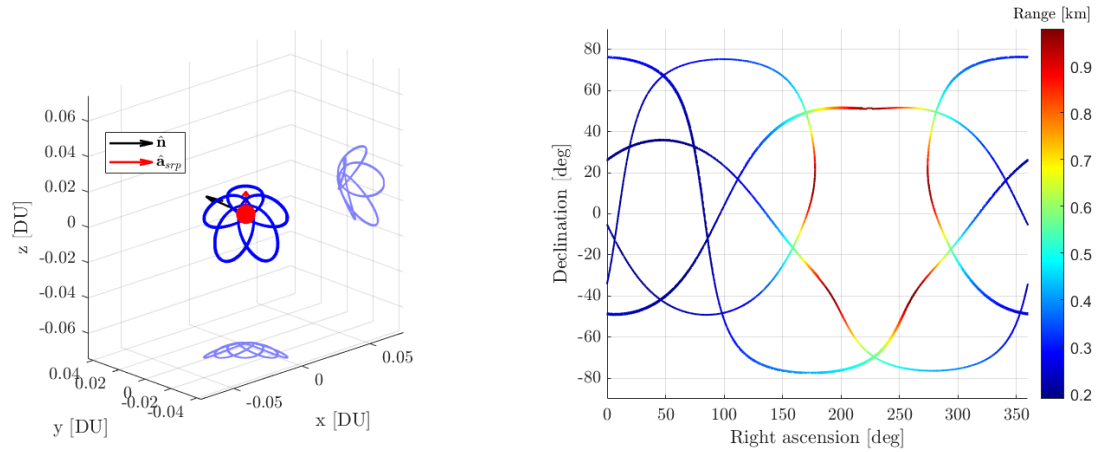

Figure 5.22: Orbit 5 at Apophis with 4:1 resonance with ground track relative to the Sun.

It is worth noting that the resonances were not obtained with any differential correction scheme, but just by changing the initial conditions with some trial and error. In fact, with this method it is possible to retrieve an initial guess to obtain a RTO that can then be corrected with a differential correction scheme, without using the simple shooting. In the following table, the main parameters of the shown orbits are summarized:

Orbit	α [°]	$\bar{\alpha}$ [°]	δ [°]	$\bar{\delta}$ [°]	ρ_0 [km]	x_0/ρ_0 [-]	ϕ_{min} [deg]	r_{max} [km]	r_{min} [km]
1	84	46.4	0	0	0.764	-4/5	3.83	0.983	0.189
2	84	46.4	0	0	0.872	-4/5	3.23	1.121	0.207
3	84	46.4	0	0	0.968	-2/5	20	1.048	0.350
4	-84	-46.4	0	0	0.755	-4/5	15.22	0.970	0.196
5	0	0	84	46.4	0.760	-4/5	6.41	0.978	0.189

Table 5.1: Orbits parameters.

It can be observed how the previously discussed choice of x_0 and ρ_0 significantly affects the resulting orbits. For instance, with all other parameters held constant, going from orbit 1 to orbit 2 required an increase in ρ_0 to obtain a lower resonance number (x_0 was also increased, maintaining the same ratio with ρ_0). In contrast, from orbit 1 to orbit 3, this ratio was reduced, resulting in a smaller ϕ_{min}, a larger r_{min} and a higher ρ_0 to preserve the same resonance. The remaining orbits illustrate how the ground track varies with different angle settings; however, in most practical applications, setting the clock angle to 0° would likely be more advantageous. If no resonance condition is required, the ground track of QTOs can provide insight into how the amplitude of the covered surface varies with changes in the x_0/ρ_0 ratio:

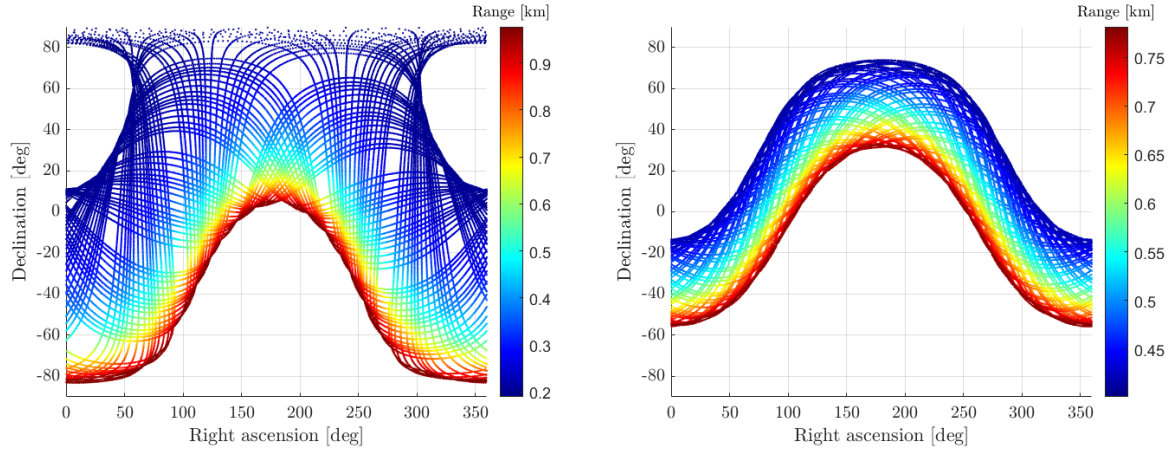

Figure 5.23: First ground track with $x_0/\rho_0 = -4/5$, second one with $x_0/\rho_0 = -1/5$.

As a reference, here is a typical RTO at Eros where no sail control is applied:

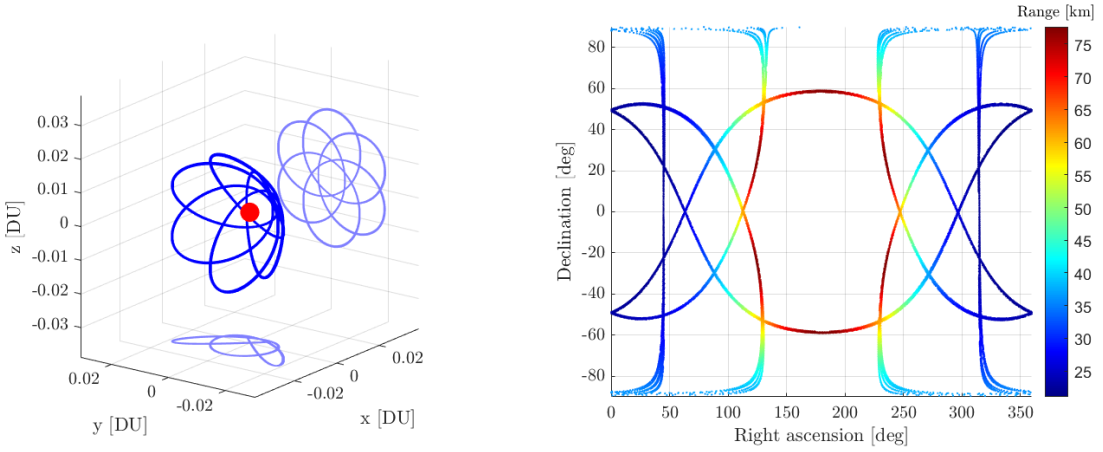

Figure 5.24: 5:1 RTO at Eros with $\phi_{min} = 58.20°$ and ground track relative to the Sun.

Apart from the different ground track, the minimum Sun–body–spacecraft angle is significantly higher than in the previously obtained orbit. Since this parameter is crucial when considering asteroid observation opportunities, it is worth noting that this control strategy has a positive effect on it.

These types of ground tracks, defined relative to the Sun, provide useful insights into the spacecraft's visibility of the asteroid, such as the time spent on the Sun-facing side and the variation of ϕ over the range. However, they do not convey much information about the actual portion of the asteroid's surface that is covered. To transform from the LVLH frame to the body-fixed reference frame of Apophis, SPICE for MATLAB [39] was used to retrieve the coordinates of Apophis at any given time.

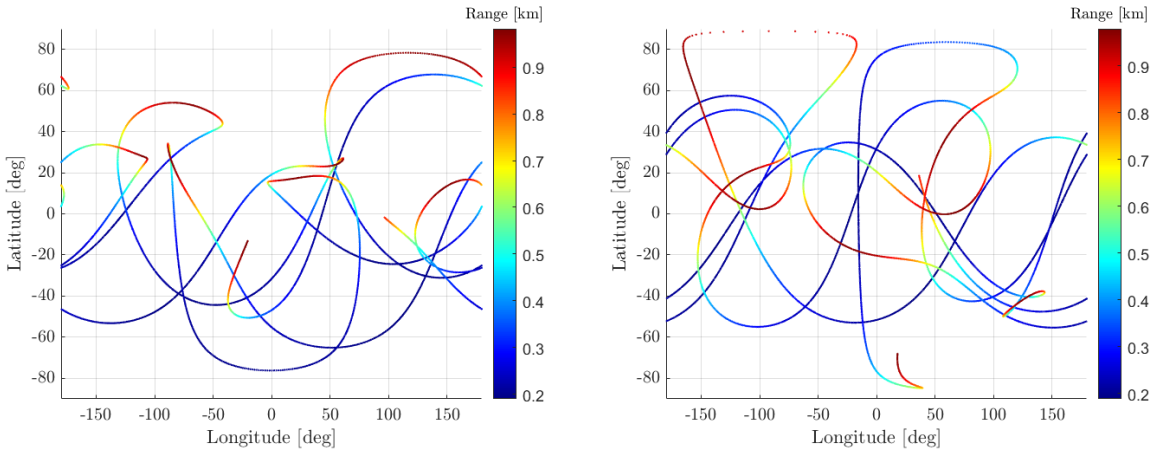

Figure 5.25: Orbit 1 and orbit 5 Apophis ground track over range for 5 days.

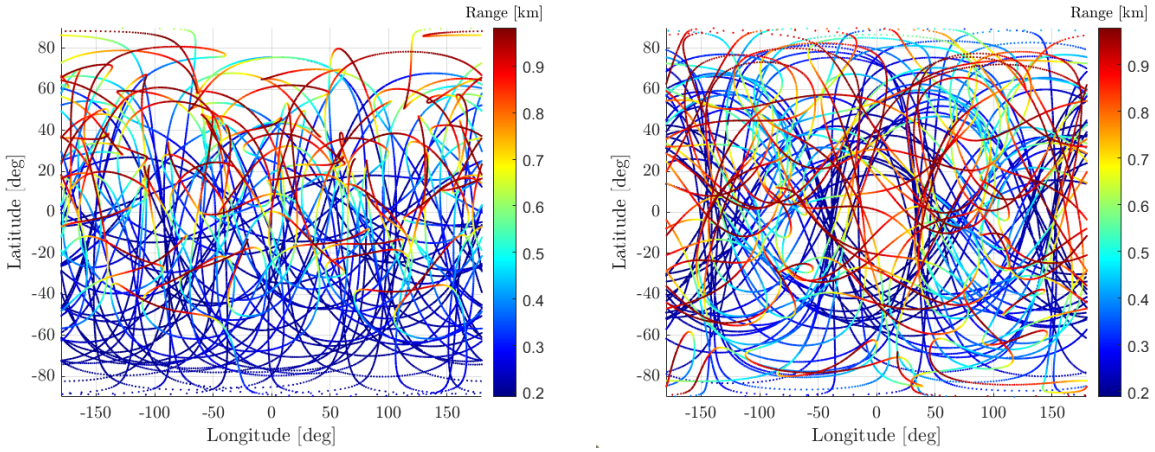

Figure 5.26: Orbit 1 and orbit 5 Apophis ground track over range for 50 days.

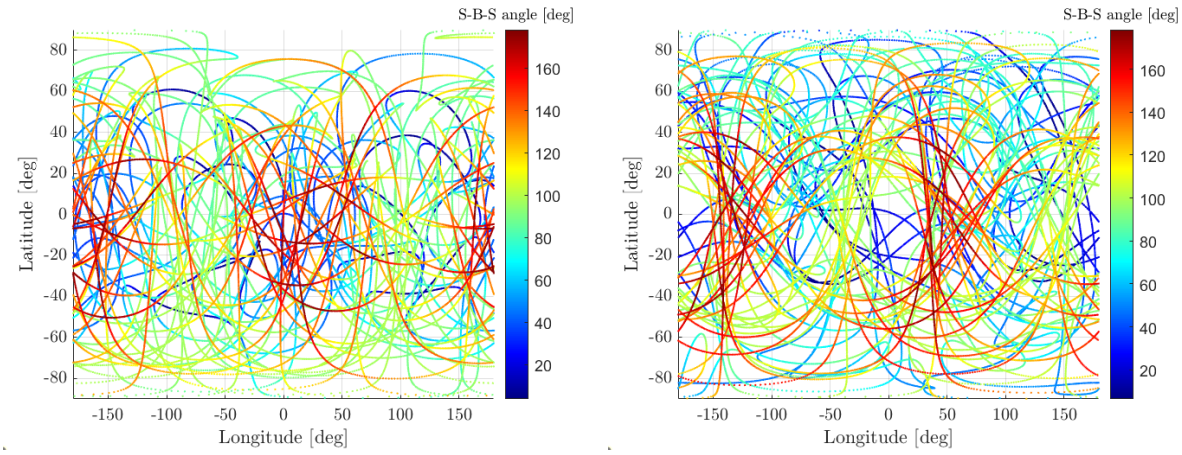

Figure 5.27: Orbit 1 and orbit 5 Apophis ground track over ϕ for 50 days.

As can be observed from the above figures, the periodicity of these orbits cannot be clearly identified in the ground tracks relative to Apophis, since its rotation axis and rotation period were not considered when defining them. It is nevertheless interesting to note that almost the entire surface of Apophis is covered in approximately 50 days, even though the range and the SBS angle do not exhibit clear periodic patterns.

Accounting for Apophis' rotation is particularly challenging, as the asteroid has two distinct periods: a precession period of 27.38 hours and a rotation period of 263 hours. Furthermore, although the angular momentum vector is known—having an ecliptic longitude of 250° and an ecliptic latitude of $-75°$ [40]—it is not constant in the LVLH frame, making it impossible to align with an artificial RTOs. It is still possible to identify orbits where the sail pitch angle matches the ecliptic latitude of the angular momentum vector, which can lead to interesting configurations. This can be achieved by setting $\alpha = \pm 85°$ and $\xi_r = 0.965$ (although this parameter cannot be directly controlled in real mission scenarios), thereby aligning the SRP acceleration vector while reducing its magnitude to obtain a feasible orbit.

Depending on the chosen orientation, it is then possible to map the north pole at the minimum range and the south pole at the maximum range, or vice versa, while keeping this range approximately constant over time. On the other hand, for the SBS angle no reliable method was found in order to control it. Naturally, for this to occur, the orbits must be orientable along the angular momentum direction while maintaining a sufficiently strong SRP acceleration, which may not be feasible for some asteroids due to an excessive area-to-mass ratio or reflective coefficient of the solar sail.

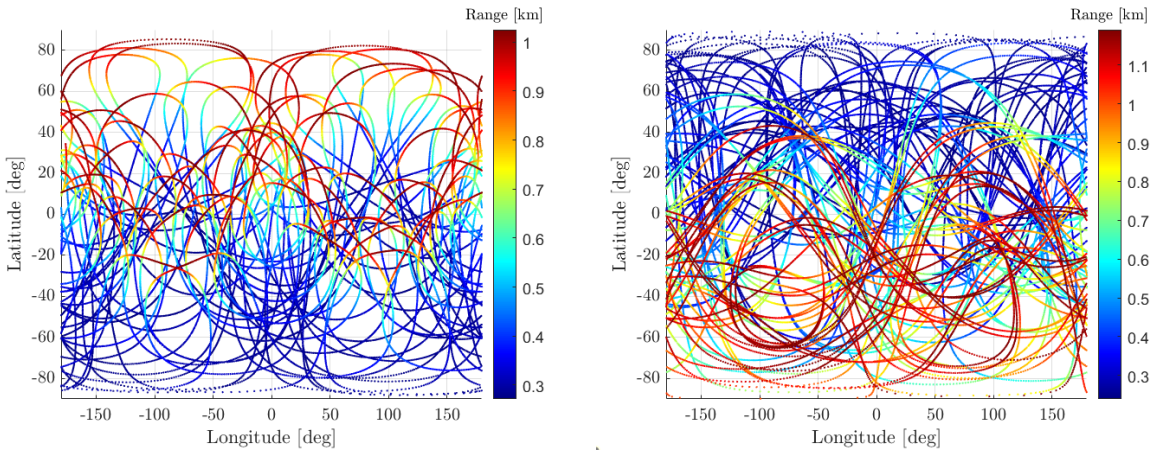

Figure 5.28: Apophis ground track over range for orbits aligned with the angular momentum for 50 days.

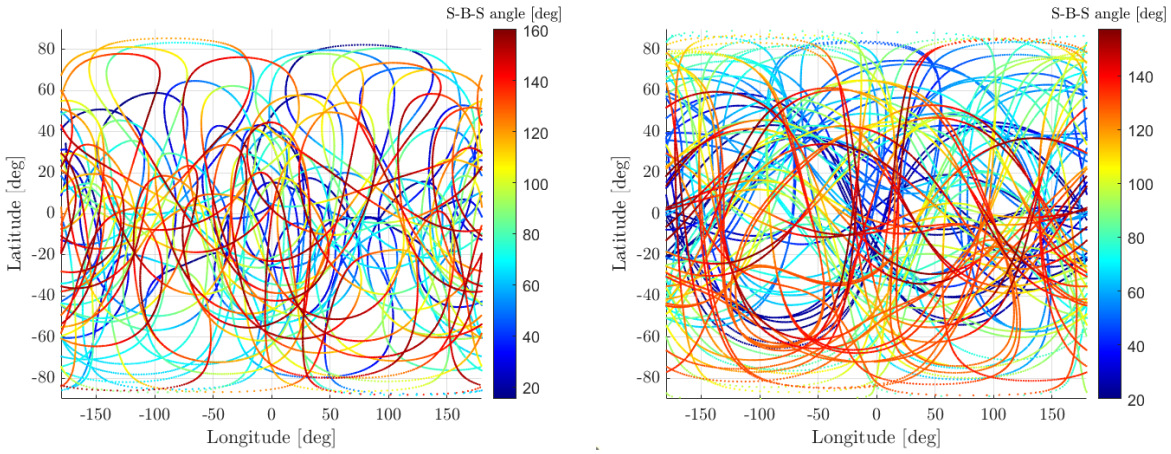

Figure 5.29: Apophis ground track over ϕ for orbits aligned with the angular momentum for 50 days.

6 | Conclusions

This thesis focused on extending the concept of terminator orbits for solar sails operating around small bodies, such as asteroids, where reducing the effects of the SRP is essential to obtain feasible and usable orbits for scientific and observation purposes.

First, two types of control strategies were defined to broaden the available design options: fixed-orientation and variable-orientation control. With the first, it was possible to identify artificial terminator orbits, characterized by a geometry similar to that of classical terminator orbits already discussed in the literature, but not lying on the actual terminator plane—instead being oriented along the SRP acceleration vector. With the second control type, these orbits could be kept within the terminator plane while mitigating the strong effects of the SRP.

An algorithm was then implemented and adapted to accommodate both control strategies, enabling the computation of stable and periodic resonant orbits. A linear stability analysis was performed to compare these solutions with typical RTOs.

To further extend the range of possible configurations, different methods for computing QTOs were investigated. For the fixed-orientation control, modifications were made to the already assessed Hamilton–Jacobi method in parabolic coordinates to obtain closed-form solutions, whereas for the variable-orientation control, a new approach based on the equilibrium energy and ZVL geometry was developed.

Finally, the effects of a non-ideal sail model were analyzed to better assess the feasibility and applicability of these orbits. Possible mission scenarios and design implications were discussed, highlighting how these new orbits could be effectively employed and how they differ from similar existing families.

Overall, these findings provide a new catalog of orbital options for missions employing solar sail technology, opening up novel possibilities for scientific exploration and mission design.

6.1. Future work

Several aspects could be further investigated to enhance the current work and refine these orbits for practical implementation in real missions.

- **Improved dynamical models:** The primary dynamical framework adopted in this study was the ANH3BP, which effectively captures the perturbative effects of the Sun and the influence of SRP. However, it neglects other relevant factors such as eclipses, the detailed gravitational field of the asteroid (here modeled as spherical), and the asteroid's orbital eccentricity, which introduces a time-dependent distance from the Sun. Future work could analyze the impact of these effects on the orbits identified in this thesis and assess their robustness under irregular gravity fields modeled by the SHE or polyhedron approaches.
- **Refined solar sail models:** Although the influence of a non-ideal sail was investigated, further refinements could include additional physical effects such as diffuse reflection or thermal emission from both sides of the sail. Moreover, the feasibility of these orbits could be evaluated from an attitude-control perspective. Another promising direction would be to model furlable sails, where variations in the sail area are exploited as an additional control parameter.
- **Deeper analysis of variable-orientation dynamics:** Several peculiar behaviors were observed in relation to the variable-orientation control strategy — for instance, changes in the resonance ratio when searching for RTOs with large α_v, or the dynamic geometry described in Section 4.3. A more detailed investigation could be carried out by analyzing the Hamiltonian structure of the system with variable control, possibly using Lie-series techniques, as proposed by Farrés et al. [15–17] or Lara et al. [41, 42].
- **Implementation of active control strategies:** When adopting more realistic models and accounting for uncertainties introduced by the actual sail behavior or perturbations from the asteroid's gravity field, it will be necessary to include active control techniques in order to stabilize periodic orbits or prevent escape for QTOs. Possible approaches include LQR controllers or optimization methods such as genetic algorithms, both of which have already been applied to solar sail dynamics [10, 28].

With these enhancements, this class of orbits could become considerably more applicable to real solar sail missions, contributing to future advances in small body exploration.

Bibliography

[1] A. W. Harris and G. D'Abramo, "The population of near-Earth asteroids," *Icarus*, vol. 257, pp. 302–312, 2015.

[2] L. Johnson, R. Young, N. Barnes, L. Friedman, V. Lappas, and C. McInnes, "Solar sails: Technology and demonstration status," *International Journal of Aeronautical Space Sciences*, vol. 13, no. 4, pp. 421–427, 2012.

[3] O. Mori, Y. Shirasawa, Y. Mimasu, Y. Tsuda, H. Sawada, T. Saiki, T. Yamamoto, K. Yonekura, H. Hoshino, J. Kawaguchi, and R. Funase, "Overview of IKAROS Mission," *Advances in Solar Sailing*, pp. 25–43, 2014.

[4] G. Lantoine, A. Cox, T. Sweetser, D. Grebow, G. Whiffen, D. Garza, A. Petropoulos, K. Oguri, J. Kangas, G. Kruizinga, and J. C. Rogez, "Trajectory and maneuver design of the NEA Scout solar sail mission," *Acta Astronautica*, vol. 225, pp. 77–98, 2024.

[5] Accessed: October, 2025. [Online]. Available: https://www.space.com/29374-nasa-cubesat-rocket-launch-system.html

[6] B. Wie, "Solar Sail Attitude Control and Dynamics, Part 1," *Journal of Guidance, Control and Dynamics*, vol. 27, no. 4, pp. 526–535, 2004.

[7] G. Mengali and A. A. Quarta, "Optimal Three-Dimensional Interplanetary Rendezvous Using Nonideal Solar Sail," *Journal of Guidance, Control and Dynamics*, vol. 28, no. 1, pp. 173–177, 2005.

[8] J. Urrios, "Advanced Solar Sailing Trajectory Design and Asteroid Close Proximity Operations," M.S. thesis, Department Aerospace Engineering, Politecnico di Milano, Milan, Italy, 2025.

[9] A. Peloni, M. Ceriotti, and B. Dachwald, "Solar-Sail Trajectory Design for a Multiple Near-Earth-Asteroid Rendezvous Mission," *Journal of Guidance, Control and Dynamics*, vol. 39, no. 12, pp. 2712–2724, 2016.

[10] I. Moore, "Design and Optimisation of Solar Sail Orbits in Proximity of Asteroids,"

Ph.D. thesis, James Watt School of Engineering, University of Glasgow, Glasgow, U.K., 2022.

[11] D. J. Scheeres, "Orbital mechanics about small bodies," *Acta Astronautica*, vol. 72, pp. 1–14, 2012.

[12] D. J. Scheeres, "Orbit mechanics about asteroids and comets," *Journal of Guidance, Control, and Dynamics*, vol. 35, pp. 987–997, 2012.

[13] E. Morrow, D. J. Scheeres, and D. Lubin, "Solar sail orbit operations at asteroids," *J. Spacecr. Rockets*, vol. 38, no. 2, pp. 279–286, 2001.

[14] J. Heiligers and D. J. Scheeres, "Solar-sail orbital motion about asteroids and binary asteroid systems," *Journal of Guidance, Control, and Dynamics*, vol. 41, no. 9, pp. 1947–1962, 2018.

[15] A. Farrés and À. Jorba, "Dynamics, Geometry and Solar Sails," *Indagationes Mathematicae*, vol. 27, no. 5, pp. 1245–1264, 2016.

[16] A. Farrés, À. Jorba, J.-M. Mondelo, and B. Villac, "Periodic motion for an imperfect solar sail near an asteroid," in *Advances in Solar Sailing*. Springer Berlin Heidelberg, 2014, pp. 885–898.

[17] A. Farrés, À. Jorba, and J.-M. Mondelo, "Numerical study of the geometry of the phase space of the Augmented Hill Three-Body problem," *Celestial Mechanics and Dynamical Astronomy*, vol. 129, no. 1-2, pp. 25–55, 2017.

[18] T. Williams and M. Abate, "Capabilities of Furlable Solar Sails for Asteroid Proximity Operations," *Journal of Spacecraft and Rockets*, vol. 46, no. 5, pp. 967– 975, 2009.

[19] J. Heiligers, S. Hiddink, R. Noomen, and C. R. McInnes, "Solar sail Lyapunov and Halo orbits in the Earth–Moon three-body problem," *Acta Astronautica*, vol. 116, pp. 25–35, 2015.

[20] H. Baoyin and C. R. McInnes, "Solar Sail Halo Orbits at the Sun–Earth Artificial L1 Point," *Celestial Mechanics and Dynamical Astronomy*, vol. 94, pp. 155–171, 2006.

[21] M. T. Ozimek, D. J. Grebow, and K. C. Howell, "Design of Solar Sail Trajectories with Applications to Lunar South Pole Coverage," *Journal of Guidance, Control and Dynamics*, vol. 32, no. 6, pp. 1884–1897, 2009.

[22] T. J. Waters and C. R. McInnes, "Periodic Orbits Above the Ecliptic in the Solar-

Sail Restricted Three-Body Problem," *Journal of Guidance, Control and Dynamics*, vol. 30, no. 3, pp. 687–693, 2007.

[23] S. B. Broschart, G. Lantoine, and D. J. Grebow, "Quasi-terminator orbits near primitive bodies," *Celestial Mechanics and Dynamical Astronomy*, vol. 120, no. 2, pp. 195–215, 2014.

[24] S. B. Broschart, D. J. Scheeres, and B. F. Villac, "New families of multi-revolution terminator orbits near small bodies," in *Proceedings of the AAS/AIAA Astrodynamics Specialist Conference*, ser. Advances in the Astronautical Sciences, vol. 135. Pittsburgh, PA, USA: Univelt Inc., 2009, pp. 1685–1702.

[25] Y. Oki, Y. Tsuda, and J. Kawaguchi, "Extension of stable terminator orbits around small bodies," *Acta Astronautica*, vol. 157, pp. 180–188, 2019.

[26] F. Damme and J. Oberst, "Orbital distances and options for small body satellites in Non-Keplerian orbits dominated by solar radiation pressure," *Planetary and Space Science*, vol. 219, 2022.

[27] G. M. Brown, D. R. Wibben, P. G. Antreasian, and K. M. Getzandanner, "Leveraging Resonant Terminator Orbits for the Trajectory Design of OSIRIS-APEX at (99942) Apophis," in *46th Annual AAS Guidance, Navigation and Contro Conference*, ser. Advances in the Astronautical Sciences, Breckenridge, CO, USA, 2024.

[28] M. Giancotti, "Stable Orbits in the Proximity of an Asteroid: Solutions for the Hayabusa 2 Mission," Ph.D. thesis, Sapienza - University of Rome, Rome, Italy, 2014.

[29] J. Bookless and C. McInnes, "Dynamics and Control of Displaced Periodic Orbits Using Solar-Sail Propulsion," *Journal of Guidance, Control and Dynamics*, vol. 29, no. 3, pp. 527– 537, 2006.

[30] B. Dachwald, W. Seboldt, M. Macdonald, G. Mengali, A. A. Quarta, C. R. McInnes, L. R. Reyes, D. J. Scheeres, B. Wie, M. Görlich, F. Lure, B. Diedrich, V. Baturkin, V. L. Coverstone, M. Leipold, and G. P. Garbe, "Potential Solar Sail Degradation Effects on Trajectory and Attitude Control," in *AIAA Guidance, Navigation, and Control Conference and Exhibit*, vol. 6172, San Francisco, California, USA, 2005.

[31] C. R. Koppel, "New tool for finding periodic halo orbits: The solver of a spacecraft simulator (ESPSS-ECOSIMPRO ® European space propulsion system simulation)," 2016. [Online]. Available: https://api.semanticscholar.org/CorpusID:198110187

[32] A. R. Sobey and T. R. Lockett, "Design and Development of NEA Scout Solar Sail

Deployer Mechanism," in *Proceedings of the 43rd Aerospace Mechanisms Symposium*, NASA Ames Research Center, 2016, pp. 315–328.

[33] Nasa Horizon. Small-body database lookup. Accessed: October, 2025. [Online]. Available: https://ssd.jpl.nasa.gov/tools/sbdb_lookup.html#/

[34] G. Lantoine, S. B. Broschart, and D. J. Grebow, "Design of quasi-terminator orbits near primitive bodies," in *AAS/AIAA Astrodynamics Specialist Conference*, ser. Advances in the Astronautical Sciences, Hilton Head, SC, USA, 2013.

[35] S. Kikuchi, Y. Oki, and Y. Tsuda, "Frozen Orbits Under Radiation Pressure and Zonal Gravity Perturbations," *Journal of Guidance, Control and Dynamics*, vol. 44, no. 11, pp. 1924– 1946, 2021.

[36] D. J. Scheers, "Satellite Dynamics about Small Bodies: Averaged Solar Radiation Pressure Effects," *The Journal of the Astronautical Sciences*, vol. 47, no. 1-2, pp. 25–46, 1999.

[37] L. D. Landau and E. M. Lifshitz, *Mechanics*. Pergamon Press, 1976.

[38] S. B. Broschart, G. Lantoine, and D. J. Grebow, "Characteristics of quasi-terminator orbits near primitive bodies," in *AAS/AIAA Spaceflight Mechanics Meeting*, ser. Advances in the Astronautical Sciences, Kauai, Hawaii, USA, 2013.

[39] NASA Navigation and Ancillary Information Facility (NAIF). MICE: SPICE Toolkit for MATLAB, 2025. Accessed: October, 2025. [Online]. Available: https://naif.jpl.nasa.gov/naif/toolkit.html

[40] P. Pravec, P. Scheirich, J. Ďurech, J. Pollock, Kušnirák, P., K. Hornoch, Galád, A., D. Vokrouhlický, D., A. W. Harris, E. Jehin, J. Manfroid, C. Opitom, M. Gillon, F. Colas, J. Oey, Vraštil, J., D. Reichart, K. Ivarsen, J. Haislip, and A. LaCluyze, "The tumbling spin state of (99942) Apophis," *Icarus*, vol. 233, pp. 48–60, 2014.

[41] M. Lara and J. F. Palacián, "Hill Problem Analytical Theory to the Order Four: Application to the Computation of Frozen Orbits around Planetary Satellites," *Mathematical Problems in Engineering*, 2009.

[42] M. Lara, J. F. Palacián, and R. P. Russell, "Mission design through averaging of perturbed Keplerian systems: the paradigm of an Enceladus orbiter," *Celestial Mechanics and Dynamical Astronomy*, vol. 108, no. 1, pp. 1–22, 2010.

A | Appendix A

This Appendix shows the computation for all the partial derivatives needed for the computation of the STM and for the differential correction scheme.

Potential of the ANH3BP for fixed orientation control:

$$U = \frac{1}{r} - \frac{1}{2}(z^2 - 3x^2) + k\cos^2\alpha\cos^2\delta(x\cos\alpha\cos\delta + y\cos\alpha\sin\delta + z\sin\alpha) \tag{A.1}$$

Second partial derivatives of the potential for the variational equations:

$$U_{xx} = \frac{3x^2}{r^5} - \frac{1}{r^3} + 3 \tag{A.2}$$

$$U_{yy} = \frac{3y^2}{r^5} - \frac{1}{r^3} \tag{A.3}$$

$$U_{zz} = \frac{3z^2}{r^5} - \frac{1}{r^3} - 1 \tag{A.4}$$

$$U_{xy} = \frac{3xy}{r^5} \tag{A.5}$$

$$U_{xz} = \frac{3xz}{r^5} \tag{A.6}$$

$$U_{yz} = \frac{3yz}{r^5} \tag{A.7}$$

Potential of the ANH3BP for variable orientation control:

$$U = \frac{1}{r} - \frac{1}{2}(z^2 - 3x^2) + k\cos^2\alpha_v(x\cos\alpha_v + r_{yz}\sin\alpha_v) \tag{A.8}$$

Second partial derivatives of the potential for the variational equations:

$$U_{xx} = \frac{3x^2}{r^5} - \frac{1}{r^3} + 3 \tag{A.9}$$

$$U_{yy} = \frac{3y^2}{r^5} - \frac{1}{r^3} + \frac{k\cos^2\alpha_v \sin\alpha_v}{r_{yz}} - \frac{k\cos^2\alpha_v \sin\alpha_v}{r_{yz}^3} y^2 \tag{A.10}$$

$$U_{zz} = \frac{3z^2}{r^5} - \frac{1}{r^3} - 1 + \frac{k\cos^2\alpha_v \sin\alpha_v}{r_{yz}} - \frac{k\cos^2\alpha_v \sin\alpha_v}{r_{yz}^3} z^2 \tag{A.11}$$

$$U_{xy} = \frac{3xy}{r^5} \tag{A.12}$$

$$U_{xz} = \frac{3xz}{r^5} \tag{A.13}$$

$$U_{yz} = \frac{3yz}{r^5} - \frac{k\cos^2\alpha_v \sin\alpha_v}{r_{yz}^3} yz \tag{A.14}$$

For the differential correction scheme, the derivatives of the Jacobi constant for the fixed-orientation control are given by:

$$\frac{\partial C}{\partial x} = \frac{x}{r^3} - 3x - k\cos^3\alpha\cos^3\delta \tag{A.15}$$

$$\frac{\partial C}{\partial y} = \frac{y}{r^3} - k\cos^3\alpha\cos^2\delta\sin\delta \tag{A.16}$$

$$\frac{\partial C}{\partial z} = \frac{z}{r^3} + z - k\cos^2\alpha\cos^2\delta\sin\alpha \tag{A.17}$$

$$\frac{\partial C}{\partial \dot{x}} = \dot{x} \tag{A.18}$$

$$\frac{\partial C}{\partial \dot{y}} = \dot{y} \tag{A.19}$$

$$\frac{\partial C}{\partial \dot{z}} = \dot{z} \tag{A.20}$$

For the variable-orientation control, the corresponding expressions are:

$$\frac{\partial C}{\partial x} = \frac{x}{r^3} - 3x - k\cos^3\alpha_v \tag{A.21}$$

$$\frac{\partial C}{\partial y} = \frac{y}{r^3} - k\cos^3\alpha_v \sin\alpha_v \frac{y}{r_{yz}} \tag{A.22}$$

$$\frac{\partial C}{\partial z} = \frac{z}{r^3} + z - k\cos^2\alpha_v \sin\alpha_v \frac{z}{r_{yz}} \tag{A.23}$$

The terms corresponding to the velocities derivatives are the same as those for the fixed-control case.

B | Appendix B

This Appendix presents the pseudo-arclenght continuation algorithm used to continue STOs [28]. The EoM for the ANH3BP can be written as:

$$\dot{\mathbf{x}} = \mathbf{f}(\mathbf{x}) \tag{B.1}$$

By making the orbit period T a parameter and introducing a new time variable $\tau = t/T$, the equation becomes:

$$\mathbf{x}' = T\mathbf{f}(\mathbf{x}) \tag{B.2}$$

where the prime $'$ indicated differentiation with respect to τ. Moreover, with this formulation $\mathbf{x}(0) = \mathbf{x}(1)$. The Jacobi constant is an implicit parameter of the system that cannot be varied directly, so an unfolding parameter λ to regulate C is introduced:

$$\mathbf{x}' = \mathbf{g}(\mathbf{x}, T, \lambda) = T\mathbf{f}(\mathbf{x}) + \lambda \nabla C(\mathbf{x}) \tag{B.3}$$

When $\lambda \neq 0$ the problem is dissipative and no periodic solution can be found, so that the algorithm is forced to always respect the condition $\lambda = 0$. The periodicity condition for the orbit is expressed as a function Γ depending on 8 parameters $\mathbf{u} = (\mathbf{x}_0, T, \lambda)$. The condition for periodicity is the following:

$$\Gamma(\mathbf{u}_{i+1}, \mathbf{u}_i) = \begin{bmatrix} \varphi_\tau(\mathbf{x}_{0,i+1}, 1) - \mathbf{x}_{0,i+1} \\ (\mathbf{x}_{0,i+1} - \mathbf{x}_{0,i}) \cdot \mathbf{g}_{0,i} \end{bmatrix} = \mathbf{0} \tag{B.4}$$

where φ_τ is the flow of $\mathbf{g}(\mathbf{u})$, g_0 is the right-hand side of Equation B.3 at $\tau = 0$, and the subscript $(\cdot)_i$ denotes a previous known solution. The first six equations ensure that the starting point is the same as the last. The last element, on the other hand, ensures that the continuation process proceeds in a direction orthogonal to the motion direction $\mathbf{g}_{0,i}$. Since any point along a periodic orbit satisfies $\mathbf{x}(0) = \mathbf{x}(1)$, this additional orthogonality

condition effectively restricts the search to a single direction and prevents undesired phase drift in the solution. In order to compute the predictor step the Jacobian matrix of Γ is needed:

$$\frac{\partial \Gamma}{\partial \mathbf{u}}(\mathbf{u}_{i+1}, \mathbf{u}_i) = \begin{bmatrix} \frac{\partial \varphi_1}{\partial \mathbf{x}_0} - \mathbf{I}_6 & \frac{\partial \varphi_1}{\partial T} & \frac{\partial \varphi_1}{\partial \lambda} \\ \mathbf{g}_{0,i} & 0 & 0 \end{bmatrix} \tag{B.5}$$

where $\mathbf{I}_6$ is the 6×6 identity matrix, and $\partial \varphi_1 / \partial \mathbf{x}_0$ is the monodromy matrix of $\mathbf{g}(\mathbf{u})$, which, along with the other two elements, are obtained with the variational equations:

$$\frac{d}{d\tau}\left(\frac{\partial \varphi_\tau}{\partial \mathbf{x}_0}\right) = TJ(\mathbf{x})\frac{\partial \varphi_\tau}{\partial \mathbf{x}_0} \tag{B.6}$$

$$\frac{d}{d\tau}\left(\frac{\partial \varphi_\tau}{\partial T}\right) = TJ(\mathbf{x})\frac{\partial \varphi_\tau}{\partial T} + \frac{\partial \mathbf{g}}{\partial T} \tag{B.7}$$

$$\frac{d}{d\tau}\left(\frac{\partial \varphi_\tau}{\partial \lambda}\right) = TJ(\mathbf{x})\frac{\partial \varphi_\tau}{\partial \lambda} + \frac{\partial \mathbf{g}}{\partial \lambda} \tag{B.8}$$

where $J(\mathbf{x})$ is the Jacobian of $\mathbf{f}$. The initial conditions are, respectively:

$$\frac{\partial \varphi_0}{\partial \mathbf{x}_0} = \mathbf{I}_6, \quad \frac{\partial \varphi_0}{\partial T} = 0, \quad \frac{\partial \varphi_0}{\partial \lambda} = 0 \tag{B.9}$$

At this point, the correction applied to $\mathbf{u}$ can be computed by solving the following linear system until a certain tolerance is met:

$$\begin{bmatrix} \left(\frac{\partial \Gamma}{\partial \mathbf{u}}\right)^{(n)} \\ \mathbf{u}_i' \end{bmatrix} \Delta \mathbf{u}^{(n)} = - \begin{bmatrix} \Gamma^{(n)} \\ (\mathbf{u}_{i+1} - \mathbf{u}_i) \cdot \mathbf{u}_i' - \Delta\sigma \end{bmatrix} \tag{B.10}$$

where $\Delta\sigma$ is the step length chosen for the continuation, while $\mathbf{u}_i'$ is the unit null vector of the Jacobian $\partial\Gamma/\partial\mathbf{u}$ evaluated at $\mathbf{u}_i$. The last equation in the system ensures that the predictor step moves in the direction tangent to the line of solution to Equation B.4. Only for the first step, the predictor is computed as:

$$\mathbf{u}_{i+1}^{(0)} = \Delta\sigma\, \mathbf{u}_i' \tag{B.11}$$

List of Figures

List of Tables

List of Acronyms

AEPs	Artificial Equilibrium Points
ANH3BP	Augmented Normalized Hill 3-Body problem
ATOs	Artificial Terminator Orbits
AU	astronomical unit
CR3BP	Circular Restricted 3-Body problem
DU	Distance Unit
EoM	Equations of Motion
LPEs	Lagrange Planetary Equations
LQR	Linear Quadratic Regulator
LVLH	Local-Vertical Local-Horizontal
NEOs	near-Earth objects
ODEs	Ordinary Differential Equations
QTOs	Quasi Terminator Orbits
RTOs	Resonant Terminator Orbits
SBS	Sun-body-spacecraft
SHE	Spherical Harmonics Expansion
SRP	Solar Radiation Pressure
STM	State Transition Matrix
STOs	Sun Terminator Orbits
TU	Time Unit
ZVL	Zero Velocity Line

List of Symbols

Variable	Description	SI unit
$\mathbf{r}$	Spacecraft position vector	km (or DU)
$\mathbf{v}$	Spacecraft velocity vector	km/s (or DU/TU)
$\mathbf{a}_{srp}$	SRP acceleration vector	km/s^2 (or DU/TU^2)
(a_x, a_y, a_z)	SRP acceleration components	km/s^2 (or DU/TU^2)
(x, y, z)	Cartesian coordinates	km (or DU)
$\dot{(\cdot)}$	Time derivative	
$\|\| \cdot \|\|$ or unbolded	Norm of a vector	
μ_a	Asteroid gravitational constant	km^3/s^2
μ_{sun}	Sun gravitational constant	km^3/s^2
N	Asteroid orbital angular velocity	1/s
R	Sun-asteroid mean distance	km
C	Jacobi constant	km^2/s^2 (or DU^2/TU^2)
H	Hamiltonian	km^2/s^2
K	Kinetic energy	km^2/s^2
U	Potential energy	km^2/s^2 (or DU^2/TU^2)
(x, ρ, θ)	Cylindrical coordinates	km, km, rad
$P_{(\cdot)}$	Generalized momentum	
h_x	Angular momentum along x-axis	km^2/s
β	Sail lightness number	-
I	Solar irradiance at 1 AU	W/m^2
R_0	Sun-Earth distance	km
c	Speed of light	km/s
S	Spacecraft area	m^2
m	Spacecraft mass	kg

K_1	Sail acceleration constant	kg·km/(m^{2}s$^{(2/3)}$)
$\mathbf{r}_s$	Direction of incident light	-
$\mathbf{n}$	Sail normal versor	-
$\hat{(\cdot)}$	Unit vector	
α	Sail pitch angle	rad (or deg)
δ	Sail clock angle	rad (or deg)
$(\cdot)_v$	Variable-orientation control angles	
r_{yz}	Position projected in the yz-plane	km (or DU)
ξ_r	Reflectivity coefficient	-
$\mathbf{x}$	State (position and velocity)	DU, DU/TU
t	Time variable	TU
$\mathbf{f}$	System dynamics	
φ	Flow of a system	
J	Jacobian	
$U_{(\cdot\ \cdot)}$	Second partial derivative of the potential	1/TU^2
$\mathbf{\Phi}$	State transition matrix	
$\mathbf{I}_n$	$n \times n$ identity matrix	
$\mathbf{M}$	Monodromy matrix	
$(\cdot)_0$	Variable at initial time	
$(\cdot)_f$	Variable at final time	
T	Orbit period	s (or TU)
$\lambda_{1,2}$	Monodromy matrix eigenvalues	
$a_{1,2},\ k_{1,2}$	Stability indices	
$\mathbf{Z}$	Simple shooting state	DU, DU/TU
$\mathbf{G}$	Simple shooting constraints	
F	Simple shooting objective function	
$\mathbf{b}$	Correction scheme constraints	
$\mathbf{y}$	Correction scheme state	DU, DU/TU, TU
r_a	Asteroid radius	km (or DU)
a	Semi-major axis	km (or DU)
e	Eccentricity	-
Ω	Right ascension of the ascending node	rad (or deg)

ω	Argument of periapsis	rad (or deg)
ν	Spacecraft true anomaly	rad (or deg)
U_{SRP}	SRP potential	km^2/s^2
n	Spacecraft mean motion	$1/s$
σ	Mean anomaly	rad (or deg)
$\mathcal{G}_i$	Derivative as a function	
$(\cdot)^*$	Prescribed angle value	
P_Φ	Sun radiation flux	$kg \cdot km^3/(m^2s^2)$
θ_p	Phase angle	rad (or deg)
$m_r,\ n_r$	Resonance bifurcations	-
γ	Arbitrary constant	-
V	Monodromy matrix eigenvector	
$\mathbf{R}_{\alpha,\delta}$	Rotation matrix	-
$(\cdot)^T$	Transpose of a matrix	
(ξ, η, θ)	Parabolic coordinates	$\sqrt{km}$, $\sqrt{km}$, rad
$S(t, \xi, \eta)$	Transforming function	
Ψ	Separation constant	km^3/s^2
$w_{1,2}$	Cubic functions	
$A,\ B$	Cubic functions variables	km
$\tilde{c}_{1,2}$	Parasitic solutions	km
ϕ	Sun-body-spacecraft angle	rad (or deg)
$(\cdot)_{eq}$	Value at equilibrium	
ϵ	Correction factor	-
τ	Scaled time variable	-
$\mathbf{g}$	Pseudo-arclenght dynamics	
$\mathbf{u}$	Pseudo-arclenght state	
λ	Unfolding parameter	
Γ	Periodicity condition	
$\Delta\sigma$	Step length	-
$\mathbf{u}_i'$	Unit null vector	